1982

Molecular beam photoionization studies of molecules and their van der Waals clusters

Yoshi Ono
Iowa State University

Ono, Yoshi

MOLECULAR BEAM PHOTOIONIZATION STUDIES OF MOLECULES AND THEIR VAN DER WAALS CLUSTERS

Iowa State University PH.D. 1982

Molecular beam photoionization studies of molecules and their van der Waals clusters

by

Yoshi Ono

A Dissertation Submitted to the
Graduate Faculty in Partial Fulfillment of the
Requirements for the Degree of
DOCTOR OF PHILOSOPHY

Major: Chemistry

Approved:

Signature was redacted for privacy.

In Charge of Major Work

Signature was redacted for privacy.

For the Major Department

Signature was redacted for privacy.

For the Graduate College

Members of the Committee:

Signature was redacted for privacy.

Iowa State University
Ames, Iowa

1982

TABLE OF CONTENTS

	Page
GENERAL INTRODUCTION	1
EXPLANATION OF THESIS FORMAT	7
EXPERIMENTAL APPARATUS	8
THEORY	19
SECTION I. A HIGH RESOLUTION PHOTOIONIZATION STUDY OF NITRIC OXIDE	28
INTRODUCTION	29
EXPERIMENTAL	31
RESULTS AND DISCUSSION	32
REFERENCES	52
SECTION II. A PHOTOIONIZATION STUDY OF CARBON DISULFIDE AND ITS CLUSTERS	54
INTRODUCTION	55
EXPERIMENTAL	58
RESULTS AND DISCUSSION	59
REFERENCES	85
SECTION III. A STUDY OF THE HIGH RYDBERG STATE AND ION-MOLECULE REACTIONS OF CARBON DISULFIDE USING THE MOLECULAR BEAM PHOTOIONIZATION METHOD	88
INTRODUCTION	89
EXPERIMENTAL	92
RESULTS AND DISCUSSION	93
REFERENCES	114

Page

SECTION IV. A MOLECULAR BEAM PHOTOIONIZATION STUDY OF OCS, $(OCS)_2$, $(OCS)_3$, AND $OCS \cdot CS_2$ 116

INTRODUCTION 117

EXPERIMENTAL 119

RESULTS AND DISCUSSION 120

REFERENCES 139

SECTION V. A HIGH RESOLUTION PHOTOIONIZATION STUDY OF ACETYLENE 141

INTRODUCTION 142

EXPERIMENTAL 144

RESULTS AND DISCUSSION 145

REFERENCES 150

SECTION VI. A STUDY OF THE UNIMOLECULAR DECOMPOSITION OF THE $(C_2H_2)_2^+$ COMPLEX 151

INTRODUCTION 152

EXPERIMENTAL 155

RESULTS AND DISCUSSION 156

REFERENCES 179

SECTION VII. A STUDY OF THE UNIMOLECULAR DECOMPOSITION OF THE $(C_2H_2)_3^+$ COMPLEX 183

INTRODUCTION 184

EXPERIMENTAL 186

RESULTS AND DISCUSSION 187

REFERENCES 209

CONCLUSION 212

REFERENCES 217

ACKNOWLEDGEMENTS 221

GENERAL INTRODUCTION

The techniques and apparatus used in photoionization studies have changed drastically over the past fifty-five years since Mohler first made "critical potential" measurements (1,2) on atomic gases using an arc discharge of the same gas in one part of a double electrode thermionic tube to induce a photoion current in another part. These studies provided inner shell ionization energy measurements of the vapors of alkali metals and rare gases. Uncertainties in these measurements were on the order of 1 eV. Since then, the technological improvements made in vacuum techniques, mass spectrometry, vacuum ultraviolet (VUV) light sources, etc. have provided methods of obtaining new types of fundamental information from a greater variety of atoms and molecules with increased accuracy.

When VUV light sources, monochromators and photon detectors were first utilized (3-6), the ion current in a gas cell was measured as a function of the photon energy to determine the ionization energies (IE) and to obtain ionization yield curves. Mass spectrometers were later incorporated into the ion detection system to be able to determine and discriminate the processes of ionization and fragmentation (7,8). Thus, the photoionization efficiency (PIE) curve, which is a measure of the photoion intensity divided by the photon intensity as a function of the photon energy, was able to provide accurate ionization energy and fragment appearance energy (AE) determinations and relative partial photoionization cross sections of gaseous molecules. This experimental

configuration was soon adopted by other researchers (9-12) and was the conventional method of obtaining photoionization data for many years.

The accuracy of the data reported in the earliest studies was restricted mainly by the photon resolutions achieved. Wainfan et al. (6,7) initially used a 10 Å photon bandwidth over the region 473-1100 Å and Watanabe (3-5) reported a 1 Å resolution at wavelengths greater than 1100 Å. Hurzeler et al. (8,9) employed a 6 Å resolution. With sufficiently high photon resolution, various types of features were able to be distinguished on the PIE curves, particularly step function type behavior near the ionization thresholds due to direct ionization to successive vibrational states of the ion, and autoionization structure superimposed on these steps. More recently, the conventional method has been used with resolutions as high as 0.016 Å (13).

With improvements in photon resolution, the main factor limiting the ultimate resolution became the rotational and vibrational energy distributions at typical gas cell temperatures. For diatoms at room temperature, the rotational envelope is approximately 26 meV and for polyatomics, 39 meV. This distribution introduces smoothly rising ionization onsets which lower the IE and AE determinations and prevents examination of the true autoionization line shapes. The effects of the hot bands can be reduced by cooling the gas to temperatures near the condensation point of the particular gas but this only aids in the study of such gases as H_2, N_2, O_2, etc. which have very low condensation temperatures.

In 1973, Parr and Taylor (14,15) demonstrated the use of a supersonic molecular beam in a photoionization study in order to take advantage of the extensive cooling of the translational, rotational, and vibrational degrees of freedom. Temperatures as low as 0.17K for rotation and 20-50K for vibration have been reported (16). Though the cooling characteristics of supersonic beams had been known for some time (17), the differentially pumped beam source used to satisfy the necessity for a very low background pressure in the ionization region resulted in an insufficient density of reactant molecules in the collision region (0.1 to 1 mTorr compared to >10 mTorr in gas cell studies) to produce an adequate ion intensity. The development of differentially pumped windowless monochromators, modern gratings and intense light sources, however, increased the intensity of VUV photons which compensated for the loss in number density.

The supersonic molecular beam technique was later adopted by Ng, Trott, Dehmer and their co-workers (18-29). Their results clearly showed finer and sharper structure compared to gas cell studies utilizing the same optical resolution. This was partly due to the nearly collisionless environment in the ionization region of the reaction chamber which essentially eliminated the problem with secondary collision processes that often hindered the gas cell studies. As a result, the interpretation of the data was made easier and less ambiguous.

Another advantageous characteristic of supersonic molecular beams is the ability to produce a relatively high concentration of clusters (30). Photoionization of these clusters produce molecular ions which

cannot be obtained from ordinary stable molecules and permits determination of thermochemical quantities such as the ion-neutral interaction energy which is obtained through the following relationship:

$$D(AB^+ \cdot AB) = IE(AB) + D(AB \cdot AB) - IE((AB)_2)$$

where $D(AB^+ \cdot AB)$ and $D(AB \cdot AB)$ are the dissociation energies of $AB^+ \cdot AB$ and $AB \cdot AB$, respectively. The monomer IE can be accurately determined from the sharp onset observed in the PIE spectra but the dimer IE is often difficult to determine due to the large differences in the equilibrium geometry between the neutral and ion dimers causing a smooth tailing characteristic near threshold and thus, is usually determined to a lesser accuracy. The neutral-neutral dissociation energy $D(AB \cdot AB)$ is generally small (order of magnitude $\sim$0.05 eV) and is obtained from the depth of the estimated Lennard Jones potential which is derived from viscosity measurements or from the second virial coefficients (31). Similarly, binding energies can be obtained for higher clusters as is demonstrated, for example, in the higher cluster studies of acetone in Ref. 24.

Furthermore, photoionization or photoexcitation of clusters can be viewed as a means of preparing collision complexes with a specific range of internal energies. Observation of the decomposition products of these complexes as a function of photon excitation energy can provide insight into the mechanisms of ion-molecule reactions, high Rydberg state chemistry, and unimolecular decomposition.

Formation of dimers in the supersonic molecular beam can be accomplished by either increasing the stagnation pressure or decreasing the nozzle temperature. By optimizing the two conditions, dimers can be formed with little or no contamination from higher clusters and without significantly increasing the load on the vacuum system. The presence of higher clusters can present a problem since an $(AB)^+_{n>2}$ cluster can fragment to $(AB)^+_2$ obscuring the actual dimer PIE curve. Systems of clusters which have been previously studied are H_2 (32), O_2 (32,33), N_2 (34), CO (34), NO (34), CO_2 (35), CS_2 (25), H_2O (23), H_2S (36), C_2H_4 (37), NH_3 (38), acetone (24), HX (X = F, Cl, Br) (39), and Ar (20,26-28), Kr (20), and Ze (19). Heterogeneous dimers XeKr, XeAr, KrAr (22), NeAr. NeKr, NeXe (29) have also been studied.

The study of higher clusters becomes more difficult as n becomes larger due to the lower density of $(AB)_n$ in the beam and contamination from still higher clusters. Slight variations in the nozzle temperature or pressure can change the cluster concentrations drastically and can result in inconsistent PIE curves. A stable beam source is thus an important criterion for studying larger clusters. Studies of higher clusters include $(Ar)_{n=2-6}$ (27), $(O_2)_{n=2-5}$ (32), $(H_2S)_{n=2-7}$ (36), $(NH_3)_{n=2-4}$ (38), and $(acetone)_{n=2-4}$ (24).

The capabilities of the supersonic molecular beam technique have been extended further with the development of a new apparatus utilizing a 3 meter monochromator, a high intensity light source, and a quadrupole mass spectrometer. A description of this apparatus is provided along with a brief review of theoretical considerations in order to provide

some insight into the interpretation of photoionization data. The experimental results on nitric oxide, carbon disulfide, carbonyl sulfide, acetylene, and their clusters are reported as well as the results for the heterogeneous dimers of $Ar \cdot CS_2$ and $CS_2 \cdot OCS$. It will be shown that the sensitivity and capabilities of this apparatus have surpassed the performance of its predecessors and entirely new insights into these molecules and their clusters have been obtained.

EXPLANATION OF THESIS FORMAT

Each section of this thesis represents an independent article in a format ready for submission for publication with minor modifications. Since the experimental apparatus is identical for each section, a description is presented prior to the first section along with a general discussion of theoretical considerations. Specific operating conditions of the apparatus are presented in a brief experimental description in each section. The figures, tables and references cited in each section refer only to those contained in that section. The references cited in the introduction, theory, experimental apparatus, and conclusion are contained in the reference section at the end of the thesis.

EXPERIMENTAL APPARATUS

The essential features of the apparatus used in these studies consist of a discharge light source, a vacuum ultraviolet light detector, a 3-meter near normal incidence VUV monochromator (McPherson 2253M) which disperses and refocuses the selected light onto a molecular beam of the target gas, and a quadrupole mass spectrometer for ion detection.

Figure 1 shows a side view of the apparatus displaying the coupling of the 3-meter monochromator and the scattering chamber. Due to the massive weights of the stainless steel scattering chamber and the monochromator, as well as the length of the monochromator exit arm, the units are coupled together with flexible bellows to prevent accidental distortion of the exit arm. Alignment of the photon beam with the molecular beam is achieved with three X-Y translational benches on which the monochromator is supported. In order to prevent any change in the relative positions of the units during the pumping cycles, the monochromator is rigidly coupled to the monochromator stand, which is in turn attached securely to the stand of the scattering chamber.

The discharge lamp is a quartz capillary tube with a water cooling jacket similar in design to those described in Refs. 18, 40 and 41, except that the length has been increased to 60 cm to provide a higher photon intensity. Since the light accepting angle for a 3-meter monochromator is appreciably smaller than that of the 1-meter units used previously, a higher intensity photon light source was necessary. This was achieved by using a lamp with increased length. Depending on the

Figure 1. Side view of the photoionization apparatus. (1) monochromator, (2) X-Y translational bench, (3) liquid nitrogen trapped 6 in. diffusion pump, (4) monochromator stand, (5) light source, (6) differential pumping arm, (7) entrance slit, (8) to Roots blower pumping system, (9) to ejector pump, (10) Daly type particle detector, (11) scattering chamber, (12) quadrupole mass spectrometer, (13) flexible coupling bellows, (14) photon detector, (15) sodium salicylate coated quartz window, (16) exit slit, (17) photoionization center, (18) 10 in. diffusion pump system, and (19) stand for scattering chamber.

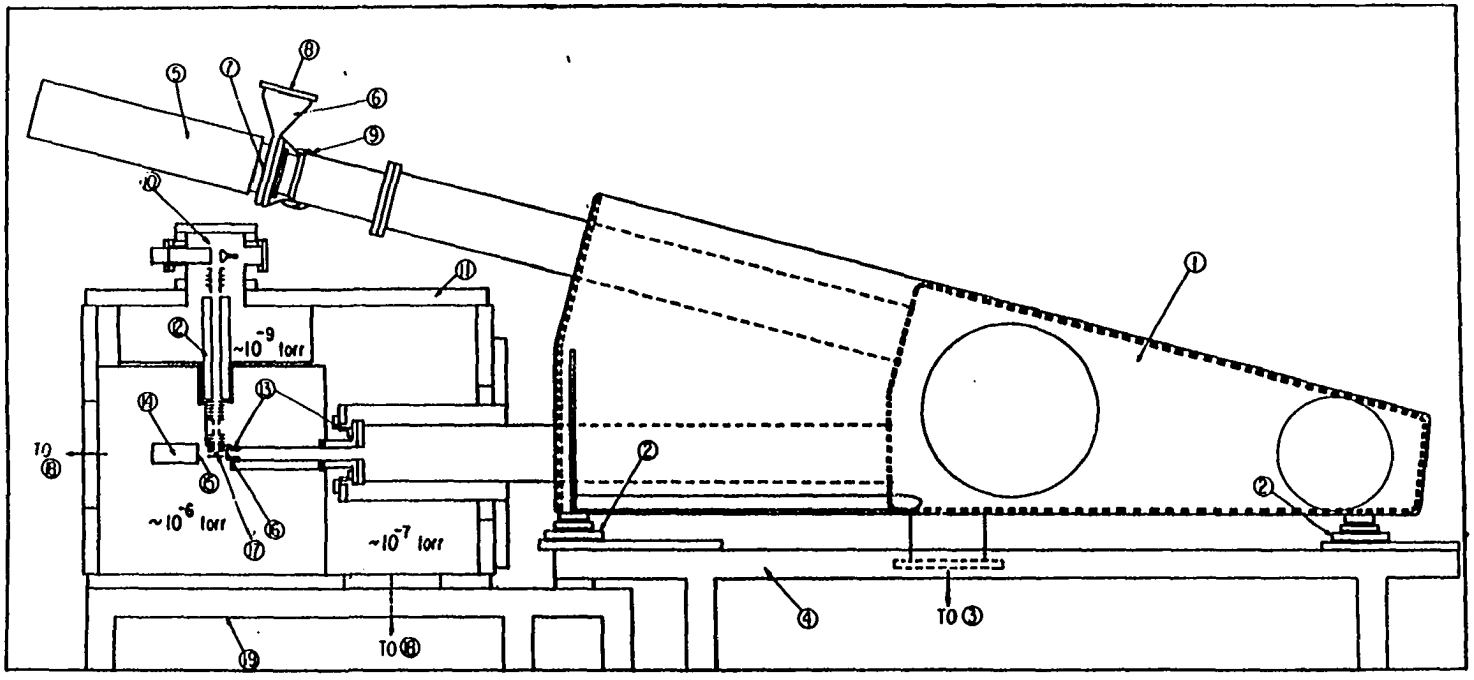
⑤
⑦
⑧
⑥
⑨
⑩
⑪
①
⑫
~10⁻⁹ torr
⑭
⑬
TO ⑧
⑯
~10⁻⁶ torr
⑮
⑰
~10⁻⁷ torr
②
②
④
TO ③
TO ⑱
⑲

spectral region, the light sources used were the helium Hopfield continuum (600-1100 Å), the argon continuum (1050-1550 Å), or the hydrogen many-lined psuedocontinuum (850-1000 Å). The helium and argon continua were generated in approximately 80 Torr of He and 200 Torr of Ar, respectively, in a pulsed discharge mode. The design of the high power pulser is similar to that described in Ref. 18 except that the maximum pulse amplitude has been increased to 20 kV in order to make possible the use of longer lamps in future studies. The hydrogen pseudocontinuum is generated in approximately 10 Torr of H_2 gas in a DC discharge mode by a current limited DC power supply (Universal Voltronix Model BAL-20-500-M) normally operated at 5 kV and 500 mA.

In order to operate the light source and monochromator without windows, the source is differentially pumped by a Roots blower (Leybold Heraeus Model WS-500) and an ejector pump (CVC KS-200). The monochromator is pumped by a liquid nitrogen trapped 6" diffusion pump (Varian model VHS6). With the lamp operated at 80 Torr He, and with a 500 μm entrance slit, a pressure of approximately 10^{-4} Torr is maintained in the monochromator.

The dispersed light emitted from the exit slit of the monochromator intersects at 90° with the molecular beam. The intensity of the photon beam is monitored by a sodium salicylate coated quartz window coupled to a photomultiplier tube in a water cooled housing. The fluorescence of the sodium salicylate has been found to be nearly linear in the region 300-2000 Å (42). The output of the photomultiplier tube is measured with a picoammeter which is subsequently connected to a voltage

to frequency converter. The digital signals are then counted. The distance from the exit slit to the ionization region is approximately 2.5 cm. The grating employed in these studies is either the Bausch and Lomb 1200 1/mm MgF_2 or the Os coated aluminum grating blazed at 1360 Å. Based on the size of the grating, the photon beam width at the ionization region is estimated to be 1.3 mm. For maximum efficiency, the Os coated grating is used in the region 500-1100 Å and the MgF_2 coated grating is used in the range 1100-2000 Å.

Figure 2 shows a detailed cross section of the differential pumping arrangement of the molecular beam production system, ionization region, ion optics and quadrupole mass spectrometer. A schematic diagram of the variable temperature nozzle design is also shown in the figure. By changing the feeding rate of the liquid nitrogen to the cooling jacket or the input power of the heater, the nozzle temperature can be varied from ∿90-600K and fixed to within ±5K of the desired level. The beam expansion chamber is pumped by a 10" diffusion pump which has a pumping speed of ∿4000 l/s and can maintain a pressure of approximately 10^{-4} Torr using a nozzle orifice diameter of 70 μm and a stagnation pressure of 700-1500 Torr. The high intensity central portion of the supersonic jet is collimated into the ionization chamber by a 0.76 mm diameter conical skimmer. The ionization chamber is typically operated at 10^{-5} to 10^{-6} Torr by pumping with a liquid nitrogen trapped 10" diffusion pump with a pumping speed of 4000 l/s. The number density of target gas molecules at the collision center is estimated to be 10^{-3} Torr. The photoions generated at the collision center are deflected into a third

Figure 2. Cross sectional view of the differential pumping arrangement of the molecular beam production system, ionization region, ion optics, and quadrupole mass spectrometer

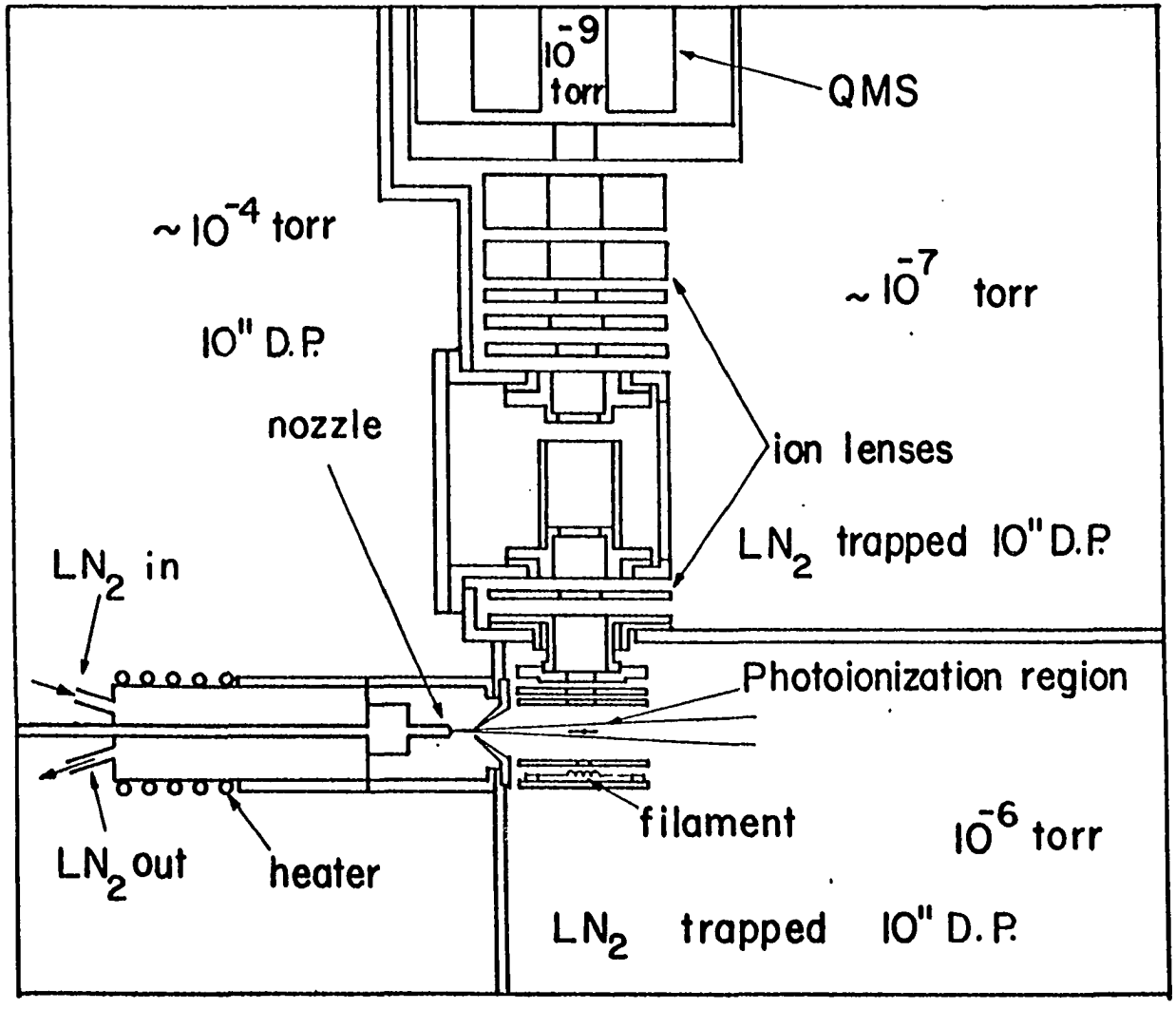
10^{-9} torr
QMS
$\sim 10^{-4}$ torr
10" D.P.
$\sim 10^{-7}$ torr
nozzle
ion lenses
LN_2 trapped 10" D.P.
LN_2 in
Photoionization region
filament
10^{-6} torr
LN_2 out
heater
LN_2 trapped 10" D.P.

chamber which is also pumped by a liquid nitrogen trapped 10" diffusion pump. This chamber is maintained at a pressure of approximately 10^{-7} Torr. The ion lenses focus the photoions onto the entrance aperture of the quadrupole mass spectrometer (Extranuclear Model 4-270-9), and the resulting mass selected ions are detected with a Daly type particle detector (43) using pulse counting techniques. The entire detector chamber is pumped differentially by a 120 l/s ion pump and a liquid nitrogen trap which maintains a pressure of approximately 10^{-9} Torr in the chamber. This arrangement not only provides a higher molecular beam intensity at the ionization center, but it also maintains a sufficiently low background pressure to prevent interference due to secondary scattering processes.

Since this apparatus is designed for high resolution studies, it is necessary to insulate the vibrations from the mechanical pumps. This was accomplished by connecting the mechanical pumps to the diffusion pumps and the scattering chamber with thin wall flexible bellows.

Due to spatial restrictions, the photon beam is modulated by a 150 Hz tuning fork chopper instead of the more common practice of chopping the molecular beam. The chopper generates two gating signals corresponding to the beam on and off. Each gate activates one of the two identical counters monitoring the number of ions detected. The difference in the output of the two counters gives the net signal. Another gate is used to activate a third counter which measures the light intensity by counting the digital output from the voltage to frequency converter. A schematic block diagram for the automatic control

system is shown in Fig. 3. A microprocessor unit (A) based on the M6800 and equipped with scalers (or counters), D/A converters, and interface adapters is employed to transmit and receive data and instructions from the other units; a molecular beam timer and gate (B), a modem for telephone communication to the AS/6 computer at the Iowa State University Computation Center (ISUCC) (D), a model 43 Teletype, a cassette tape deck for data and program storage, a monochromator control and display unit (McPherson Model 785), a voltage to frequency converter, and the ion counting system. The software in ROM enables automatic data acquisition, storage and plotting. After a preset counting time, the Teletype will print the current wavelength, the values of the three counters and the calculated PIE at that particular wavelength. The values of the PIE and light intensity are plotted immediately on a X-Y plotter. At the end of a counting cycle, the monochromator control and display unit is instructed to advance the monochromator stepping motor to the next wavelength setting and a new counting cycle is started. The smallest wavelength increment attainable with the present system is 0.0025 Å. After accumulating a set of data points, the information is recorded onto a cassette tape. At a later time, the stored data can be transferred back to the microprocessor for replotting or can be transferred to the ISUCC for further processing. The plotted light intensity is used to make wavelength calibrations by using the appropriate known atomic resonance lines or the H_2 emission lines when the H_2 pseudocontinuum is used.

Figure 3. Block diagram of the electronic components associated with the data acquisition system. Unit A is a M6800 based microprocessor equipped with three counters (scalers), peripheral interface adapters (PIA), digital-to-analog converters (DAC), and asynchronous control interface adapters (ACIA) for interaction with the monochromator control and display, the X-Y plotter, the cassette tape deck, the Teletype, and the modem for phone line communication with D, the Iowa State University Computation Center (ISUCC). Unit B is a molecular beam timer and gate, Unit C is the detector assembly comprised of a quadrupole mass spectrometer and scintillation detector. PMT and VFC represent photomultiplier tube and voltage-to-frequency converter, respectively

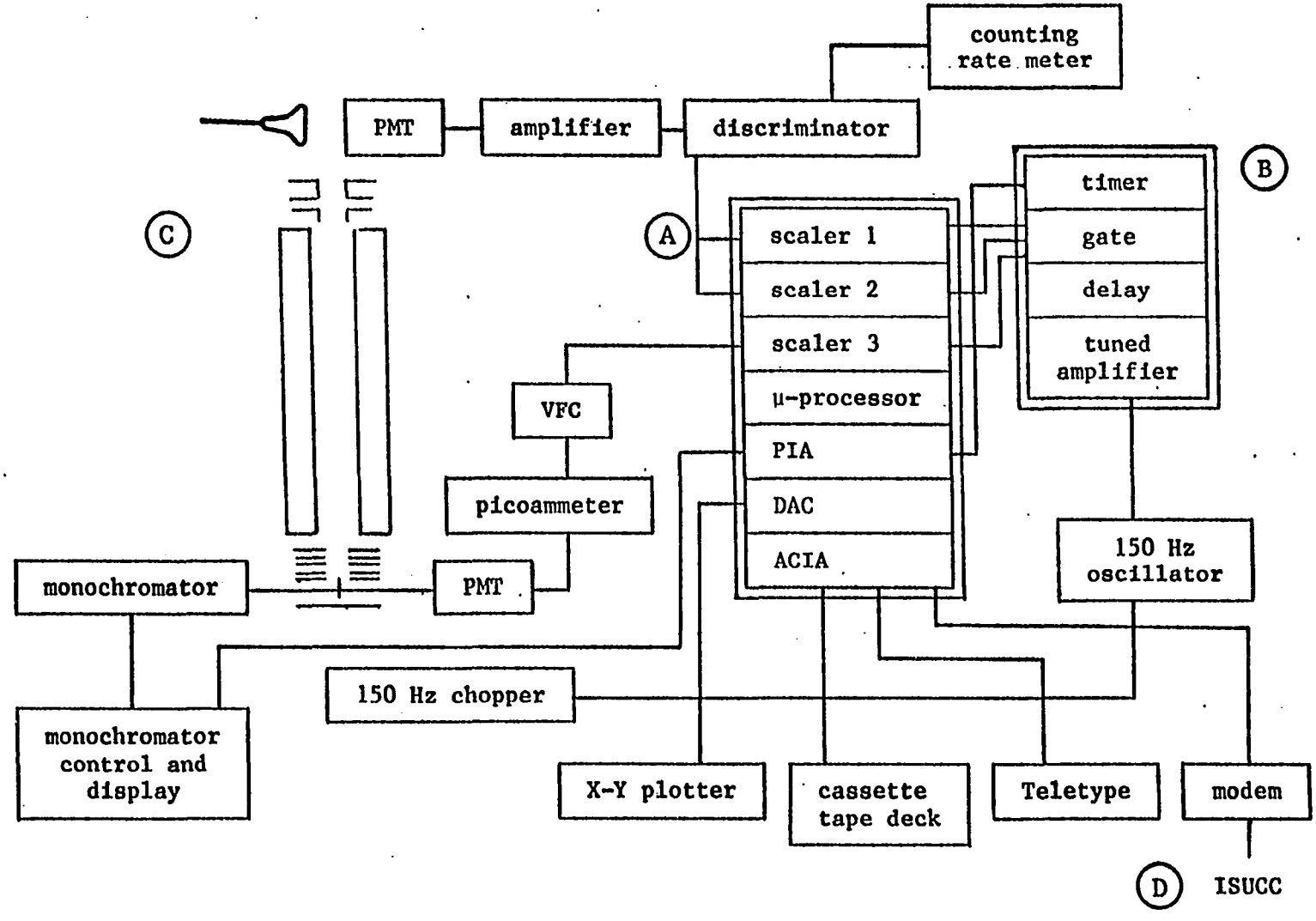
counting rate meter
PMT
amplifier
discriminator
timer
gate
delay
tuned amplifier
B
C
A
scaler 1
scaler 2
scaler 3
μ-processor
PIA
DAC
ACIA
VFC
picoammeter
monochromator
PMT
150 Hz oscillator
150 Hz chopper
monochromator control and display
X-Y plotter
cassette tape deck
Teletype
modem
D
ISUCC

THEORY

The absorption of a photon by a molecule transfers it from an initial state E_i to a final state E_f according to the relation $E_f - E_i = h\nu$, where ν is the frequency of the photon and h is Plancks constant. When E_f corresponds to energies greater than or equal to the ionization energy, among the processes known to occur are direct ionization, autoionization, predissociation, ion pair formation, and fragmentation. Each of these processes is manifested in a characteristic form on the PIE curve and the interpretation of these features allow one to quantitatively deduce various traits of the molecule. The relations between the observed PIE data and the related physical quantities are briefly presented in the following summary of the theoretical aspects of photoionization.

The direct ionization process involves the ejection of an electron from the ground state of the molecule to form an ionic state:

$$AB(X,\ v=0) + h\nu \rightarrow AB^{+}(\tilde{X},\ \tilde{A},\ \tilde{B},\ \ldots,\ v=0,1,2,\ \ldots) + e^{-} \quad .$$

The minimum photon energy for this process is called the adiabatic ionization energy and corresponds to the initial rise of the ion intensity on the PIE curve. Theoretical treatments of this process (44,45) predict step function type behavior in the PIE curve near the threshold with each successive step representing the onset of a vibrationally excited state of the ion. This has been observed experimentally for numerous molecules (46-48).

If the ground state wavefunction is characterized by the wavefunction Ψ_i and the final state molecular ion and electron by Ψ_f, the transition moment integral is expressed as

$$M_{if} = \langle \Psi_i | \Sigma \hat{p} | \Psi_f \rangle$$

where $\Sigma\hat{p}$ is the dipole moment operator extended over all electrons and nuclei. If the wavefunction is separated into the product of the electronic and nuclear wavefunctions using the Born-Oppenheimer approximation, by considering only the vibrational nuclear motions, the wavefunction can be rewritten as

$$\Psi(r,R) = \Psi_e(r,R)\Psi_v(R)$$

where r and R represent the electron coordinates and the nuclear coordinates, respectively. Furthermore, the dipole operator can be separated into electronic and nuclear dependent parts.

$$\Sigma \hat{p} = \Sigma \hat{p}_e + \Sigma \hat{p}_n \quad .$$

The transition moment is thus

$$M_{if} = \int \Psi^*_{v_i}(R)\Psi_{v_f}(R)dR \int \Psi^*_{e_i}(r,R)\ \Sigma \hat{p}_e\ \Psi_{e_f}(r,R)dr$$

$$+ \int \Psi^*_{v_i}(R)\ \Sigma \hat{p}_n\ \Psi_{v_f}(R)dR \int \Psi^*_{e_i}(r,R)\Psi_{e_f}(r,R)dr \quad .$$

Since the electronic eigenfunctions are orthogonal, the second term is zero and the expression for the transition probability P_{if} is

$$P_{if} = \langle \Psi_{v_i} | \Psi_{v_f} \rangle^2 \langle \Psi_{e_i} | \Sigma\ p_e | \Psi_{e_f} \rangle^2 \quad .$$

The vibrational overlap integral is the Franck-Condon factor which is represented by the relative heights of the steps near the threshold. The second term is the electric dipole moment element and is nonzero for all one electron photoionization processes since Ψ_{e_f} possesses finite contributions of all symmetries.

Figure 4 illustrates the direct ionization process and several Franck-Condon overlap conditions. Since the maximum transition probability occurs in the Franck-Condon region where the initial wavefunction is a maximum, the shape of the PIE curve near threshold will reflect the shape and states of the ionic potential curve in the Franck-Condon region. The three cases shown exemplify the ejection of an electron from (a) a nonbonding molecular orbital, (b) a bonding molecular orbital, and (c) an antibonding molecular orbital. The equilibrium internuclear distance of the ion relative to that of the neutral molecule as well as the depth of the ion potential curve is dependent upon the type of orbital from which the ejected electron originated. Thus, for case (a), there is little change in the potential energy curve shape of the ion relative to that of the neutral molecule and the 0-0 transition is expected to be the major feature. For case (b), removing a bonding electron increases the equilibrium R and transitions occur to the steep slope of the repulsive side of the ionic potential curve. The depth of the curve is smaller than in case (a) or (c) and the vibrational intervals v are also smaller. The expected threshold behavior is shown in Fig. 4. In case (c), removal of an antibonding electron strengthens the bonding of the molecular ion and decreases the

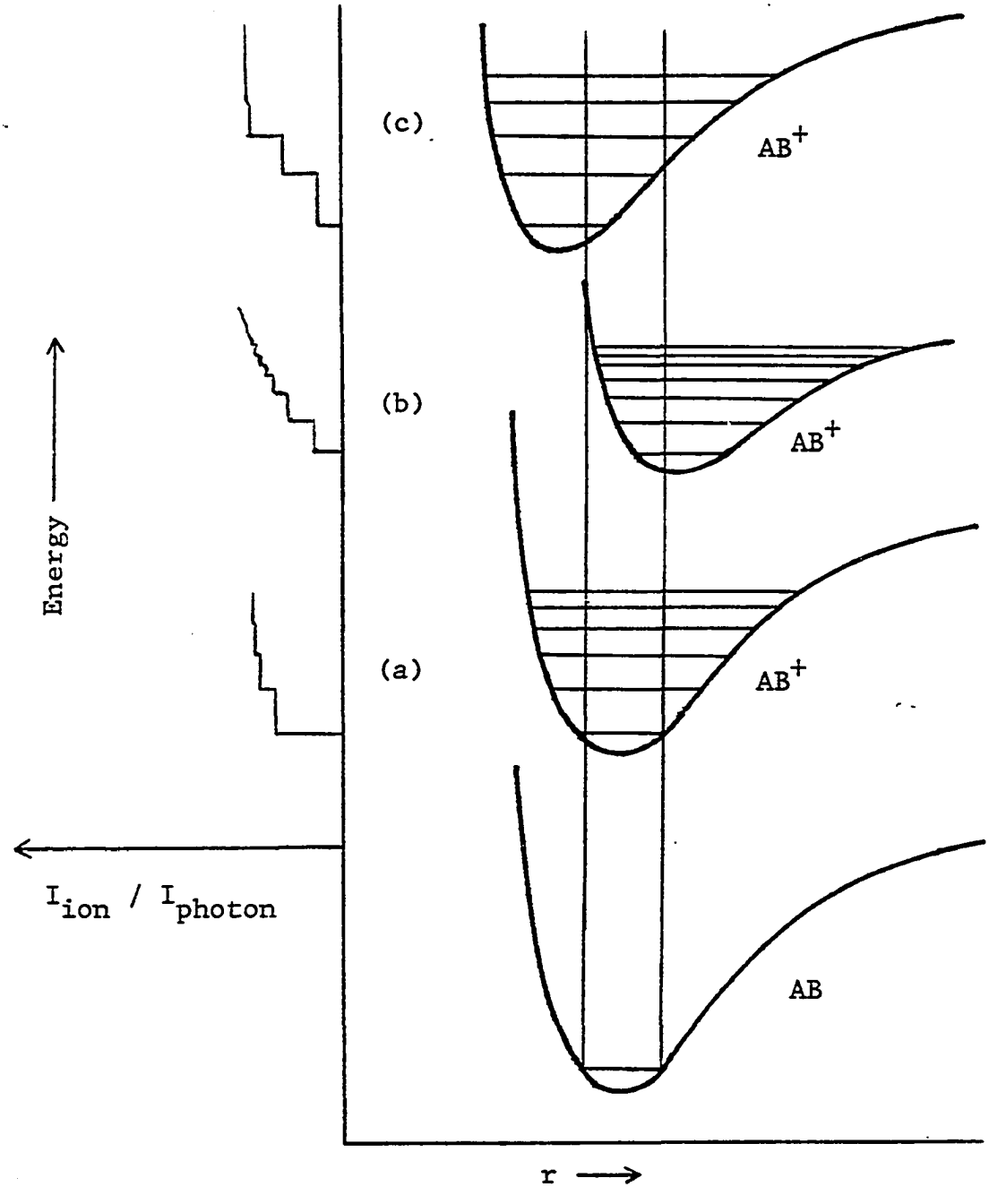

Figure 4. Franck-Condon overlap conditions for direct ionization involving the ejection of (a) a nonbonding electron, (b) a bonding electron, and (c) an antibonding electron

bond length which in turn increases the vibrational spacings in the ionic state, resulting in the behavior shown in Fig. 4. This is the case for nitric oxide which is the subject of Section I.

When discrete states of the neutral molecule lie above the level of the first ionization energy, population of these states can occur through absorption and subsequently cross into the ionization continuum with the loss of an electron.

$$AB + h\nu \rightarrow AB^{*} \rightarrow AB^{+} + e^{-} \quad .$$

Autoionization is a resonant process which appears as a peak and/or dip on the PIE curve wherever E_f corresponds to the energy of a discrete state and interaction occurs between the state and the continuum. The width of the structure is inversely proportional to the lifetime of the autoionizing state. This interaction between a continuum and a discrete state has been treated theoretically by Fano (49), successfully accounting for the experimentally observed asymmetry, broadening, and shifting of the autoionization peak. A more rigorous treatment considering the interaction of many resonances with many continua was presented by Mies (50). Figure 5 illustrates the autoionization process and its interaction with the continua.

Autoionization structures typically appear as a progression of peaks following the Rydberg formula

$$\nu_n = \nu_\infty - R/(n - \delta)^2$$

where ν_∞ is the convergence limit of the series, R is the Rydberg constant, n is the principal quantum number of a Rydberg state and δ is the

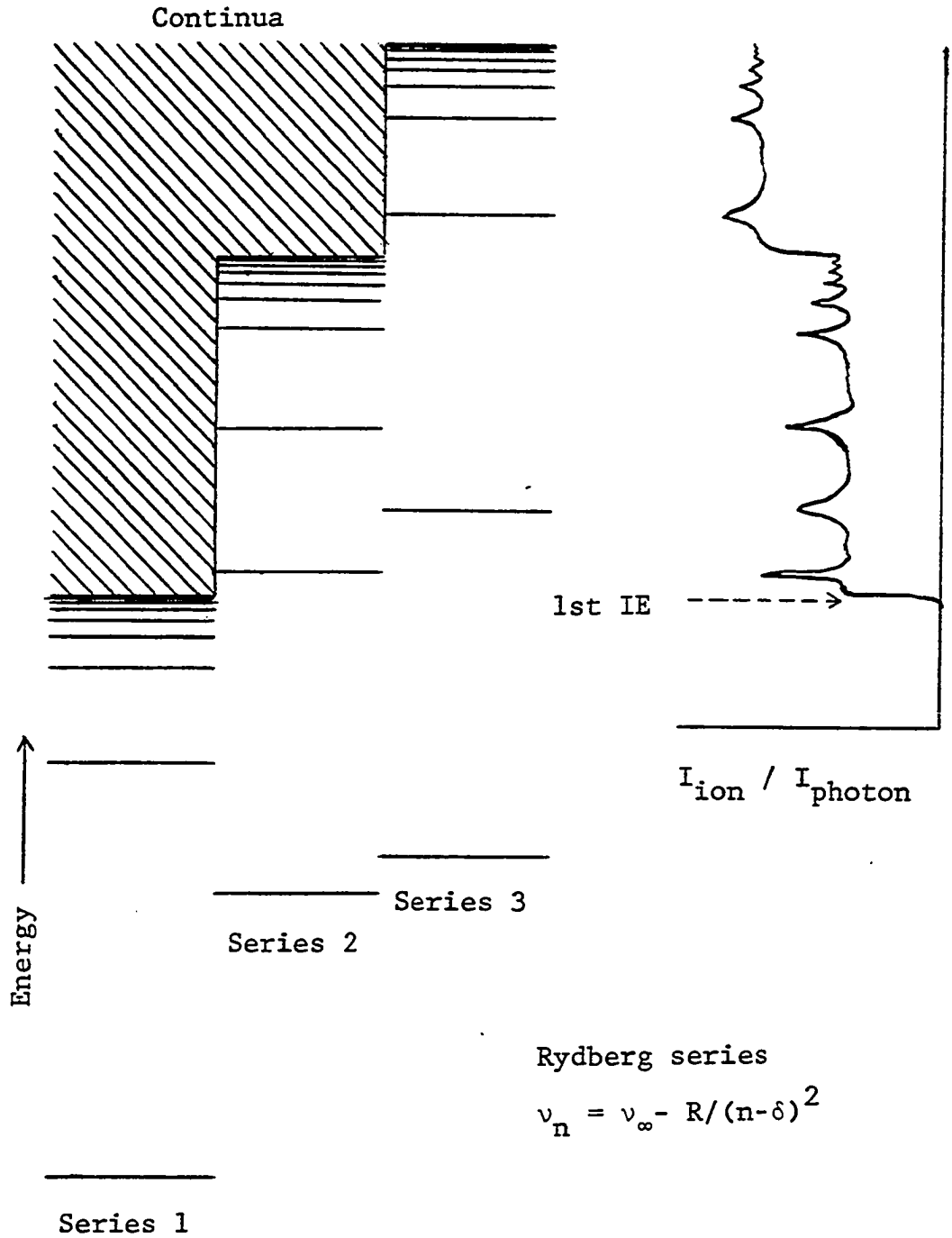

Figure 5. Series of Rydberg levels interacting with the one or more continua demonstrating the autoionization process

"quantum defect". The term $n-\delta$ is often expressed as n^*, the effective principal quantum number. A Rydberg state is simply an ion core in a specified quantum state and a Rydberg electron with quantum numbers n and ℓ. The quantum defect is a parameter introduced to account for the penetration of the ion core by the Rydberg electron and, to a lesser extent, for the polarization of the core charge distribution and the exchange forces between the Rydberg electron and the core. The degree of penetration of the core by the electron is dependent upon ℓ, the orbital angular momentum quantum number for a Rydberg series (i.e., ns, np, nd, etc.), and is a major factor effecting the magnitude of δ. The nature of a Rydberg series is often deduced by the value obtained for δ since $\delta_s > \delta_p > \delta_d$, etc. In a given series, the quantum defect remains nearly constant, especially at high n values thus making it possible to accurately determine higher IEs. Further details of autoionization and Rydberg series are found in Refs. 41, 48, 51-53.

Analysis of the Rydberg series for nitric oxide, carbon disulfide, carbonyl sulfide and acetylene have been performed and are reported in this thesis. The observed structures are often complicated and interactions are extensive. Fits to the Rydberg formula were made when possible with the aid of information reported in previous absorption studies.

Predissociation follows the same mechanism as autoionization with the exception that the continuum involves formation of two neutral fragments.

$$AB + h\nu \rightarrow AB^{*} \rightarrow A + B \quad .$$

Though the results of this process are not observable in photoionization, it competes with autoionization so as to effect the intensity of the autoionization structure. The theory involved in autoionization also applies to predissociation and was demonstrated by the asymmetric line shape obtained for the predissociation of H_2 (54).

Fragmentation of the parent ion occurs when sufficient internal energy is concentrated at a particular bond to dissociate it forming a fragment ion and a neutral species.

$$AB + h\nu \rightarrow AB^{+*} + e^{-} \rightarrow A^{+} + B + e^{-} \quad .$$

The minimum photon energy at which A^{+} ions are formed is the appearance energy and is often used to deduce the heat of formation of fragment ions (55) or the bond dissociation energies of molecular ions. This is possible, however, only when the reverse activation energy is zero, which is generally the case for diatomics and small polyatomic molecules. For larger polyatomic molecules, the rate of fragmentation at the minimum energy can be too small to be identified and the difference between the actual minimum energy and the observed AE is called the kinetic shift. In a statistical approach to the expression for the rate constant, quasi-equilibrium theory assumes that rapid energy randomization occurs throughout the oscillators in the molecule and if sufficient energy becomes concentrated in one particular bond, dissociation will occur. The rate constant has been expressed as

$$k(E) = \frac{\alpha W^{\ddagger}(E - E_o)}{h\rho(E)}$$

where α is the reaction path degeneracy, h is Planck's constant, $W^{\ddagger}(E-E_o)$ is the number of quantum states of the transition complex with energies $\leq E-E_o$, and $\rho(E)$ is the density of states of the parent ion at energy E. When the energy is slightly higher than E_o, the rate constant is small and a sensitive apparatus is required to determine the true AE. Comparisons made between rates derived with this formula and experimental data show that the degree of agreement depends upon the method and accuracy of calculating $W^{\ddagger}(E-E_o)$ and $\rho(E)$ (56). The finer details of the fragmentation process can be found in Refs. 57 and 58.

SECTION I.

A HIGH RESOLUTION PHOTOIONIZATION STUDY OF NITRIC OXIDE

INTRODUCTION

The photoionization efficiency (PIE) curve of nitric oxide displays a classic example of step function type behavior near the threshold. Previous photoionization studies of NO have demonstrated this (1-8) and more recently, fine structure superimposed upon these steps has been observed (7,8). A PIE curve for NO^+ in the region 1190-1340 Å was published by Ng, Mahan, and Lee (8) in 1976 and since the measurements were carried out using the supersonic beam method to reduce the rotational temperature of NO, a more detailed autoionization structure was evident as compared to the gas cell experiment (7) using the same optical resolution. In that same year, Miescher and Alberti (9) published an atlas of the absorption spectrum of NO, and Miescher (10) published a high resolution study of the absorption structure in the region 1420-1250 Å. This led to a reinterpretation of the fine structure in the PIE curve of Ng et al. (8) in a paper by Miescher, Lee and Gürtler (11) based on the Rydberg series observed in absorption. They assumed the $^2\Pi_{3/2}$ state was relaxed and assigned the structure as originating only from the $X^2\Pi_{1/2}$ ground state. The results of their analysis leads to the conclusion that $\Delta v < -1$ transitions of the vibrational autoionization processes are substantial. Due to the relatively low resolution of the PIE curve, Rydberg levels were specified only as np and nd, and peaks with multiple assignments were unavoidable.

According to absorption studies (9-11), four Rydberg series ns, np, nd and nf are observed in this spectral region. In order to achieve a more detailed analysis of the autoionization structure, and thus the

autoionization process in NO, it is necessary to perform photoionization experiments with higher resolution. Autoionization structure resolved beyond 80,000 cm^{-1} (1250 Å) will provide a test for the previous identifications of the Rydberg series observed in absorption (12). It is also possible to assess whether $NO(^2\Pi_{3/2})$ relaxes in a free jet expansion by comparing the relative intensity of the autoionization structure at different nozzle temperatures.

EXPERIMENTAL

The nitric oxide molecular beam was formed by a nozzle with a 50 μm diameter orifice using a stagnation pressure of ∿760 Torr. The NO gas was C.P. grade obtained from Matheson with a quoted purity of ≥99% and used without further purification.

The PIE curve for NO^+ in the wavelength region 1264-1342 Å which comprises the first two vibrational steps, v = 0 and 1, of NO^+ in its ground state was obtained using the hydrogen many-lined pseudocontinuum as the light source. The region 1189-1264 Å which covers the vibrational steps v = 2 and 3 of NO^+ was obtained with the Ar continuum. Each spectra was scanned at least twice. In some portions of the curve, the fine structure reported here is based on the average of more than three runs. Data are plotted at intervals of 0.05 Å. Typical counting times are 10s in the region 1264-1342 Å and 40s in the region 1189-1264 Å. The NO^+ signal observed with this 3-m apparatus is more than two orders of magnitude greater than that obtained with the 1-m apparatus (8) using the same optical resolution due to the improved molecular beam and light intensities.

RESULTS AND DISCUSSION

The PIE curves for NO^+ obtained using the H_2 pseudocontinuum as the light source at a nozzle temperature of 290K (1304-1342 Å) and 150K (1264-1340 Å) are depicted in Figs. 1 and 2, respectively. Figures 3(a) and 3(b) show the PIE curve in the region 1189-1264 Å obtained using the Ar continuum as the light source. As expected, a step function behavior is observed. Since the resolution is a factor of six higher than that previously used to investigate this system (8), the fine structure superimposed on these vibrational steps is much better resolved.

If the onsets at 1339.32 Å (74664.8 cm^{-1}), 1298.68 Å (77001.3 cm^{-1}), 1260.80 Å (79314.7 cm^{-1}), and 1225.62 Å (81591.4 cm^{-1}) are taken to be the ionization potentials of NO to $NO^+(X^1\Sigma^+)$ v = 0, 1, 2, and 3, respectively, we find these values are all lower in energy by $\sim$50 cm^{-1} than the values deduced from absorption (10) and emission (13,14) experiments. The first onset at 1339.32 Å (74664.8 cm^{-1}) is $\sim$56 cm^{-1} lower in energy than the value for the ionization potential of NO obtained from Ref. 10. Since the NO molecular beam was sampled under molecular flow conditions in a high vacuum chamber, contributions from secondary collisional chemiionization processes at the thresholds are expected to be negligible. Furthermore, contributions from clusters formed in the expansion should also be very small because $(NO)_n$, $n \geq 2$ constituted less than one percent of the NO beam for a room temperature nozzle operated under the present nozzle conditions. The rotational temperature is believed to be $\leq$20K ($\sim$16 cm^{-1}) (15). Taking into account the instrumental resolution which is approximately 8 cm^{-1} in this wavelength region, the

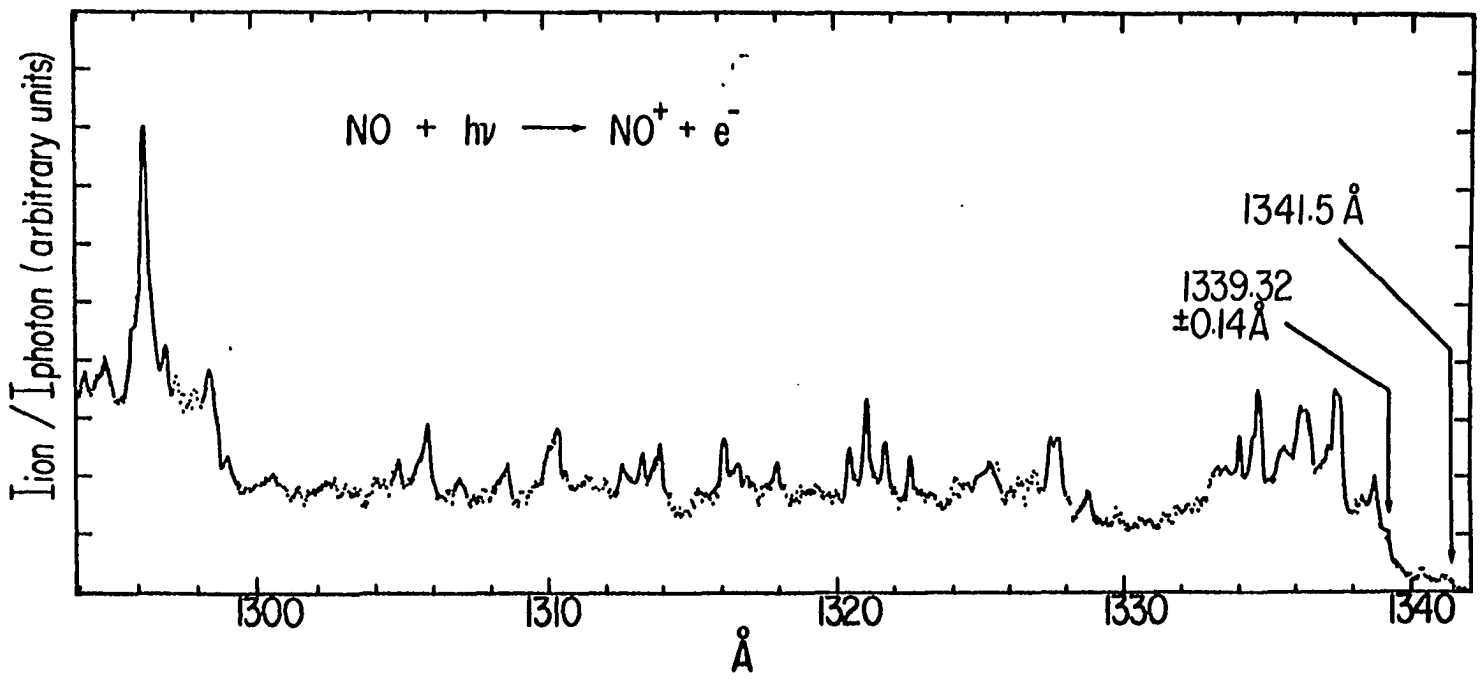

Figure 1. PIE curve for NO^+ in the region 1294-1342 Å obtained using the H_2 many-lined pseudo-continuum as the light source at a nozzle temperature of 290K and a nozzle stagnation pressure of ∿760 Torr

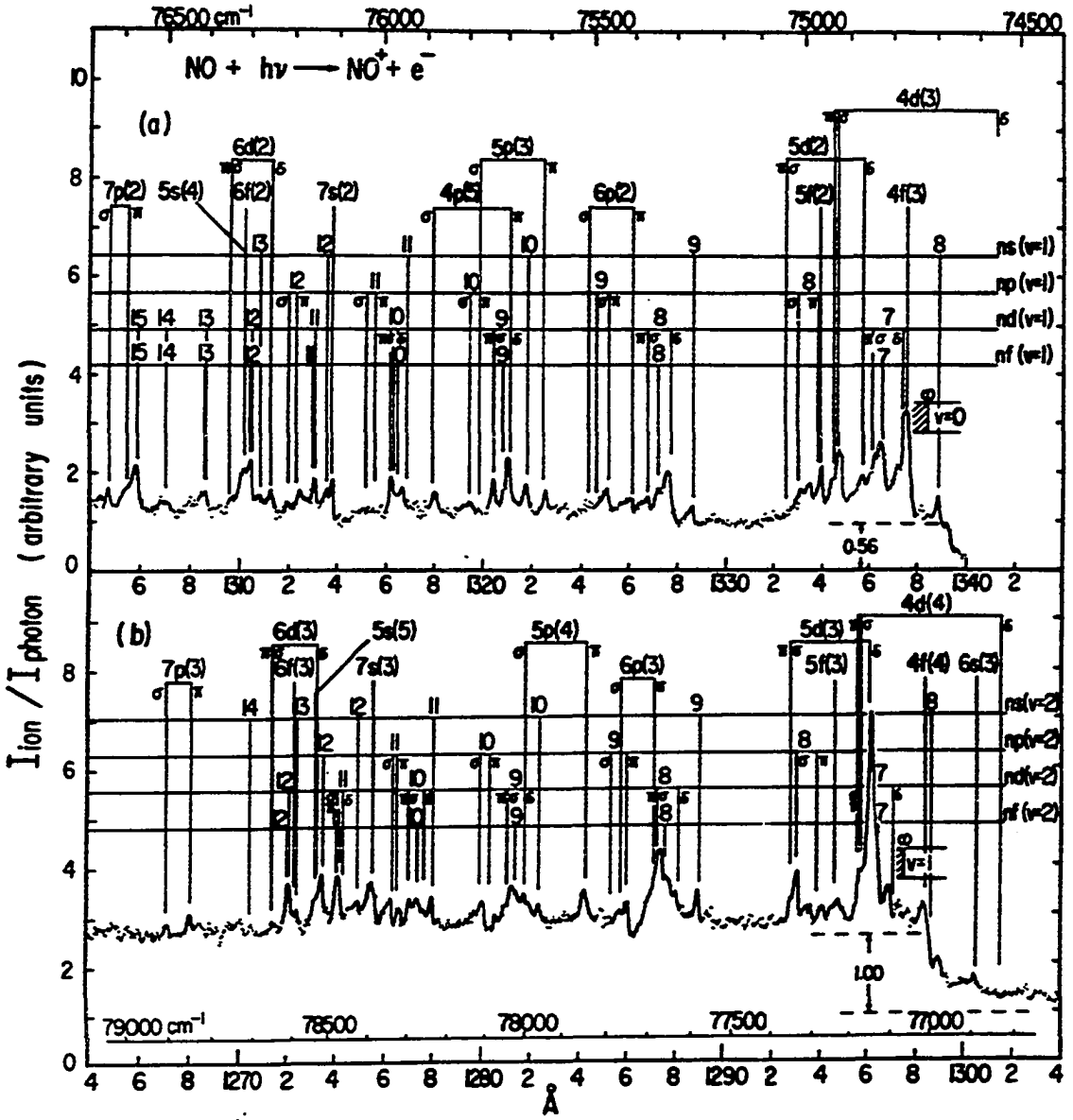

Figure 2. PIE curve for NO^+ obtained using the H_2 pseudocontinuum as the light source at a nozzle temperature of 150K and a nozzle stagnation pressure of ∿760 Torr (a) in the region 1304-1340 Å; (b) in the region 1264-1304 Å

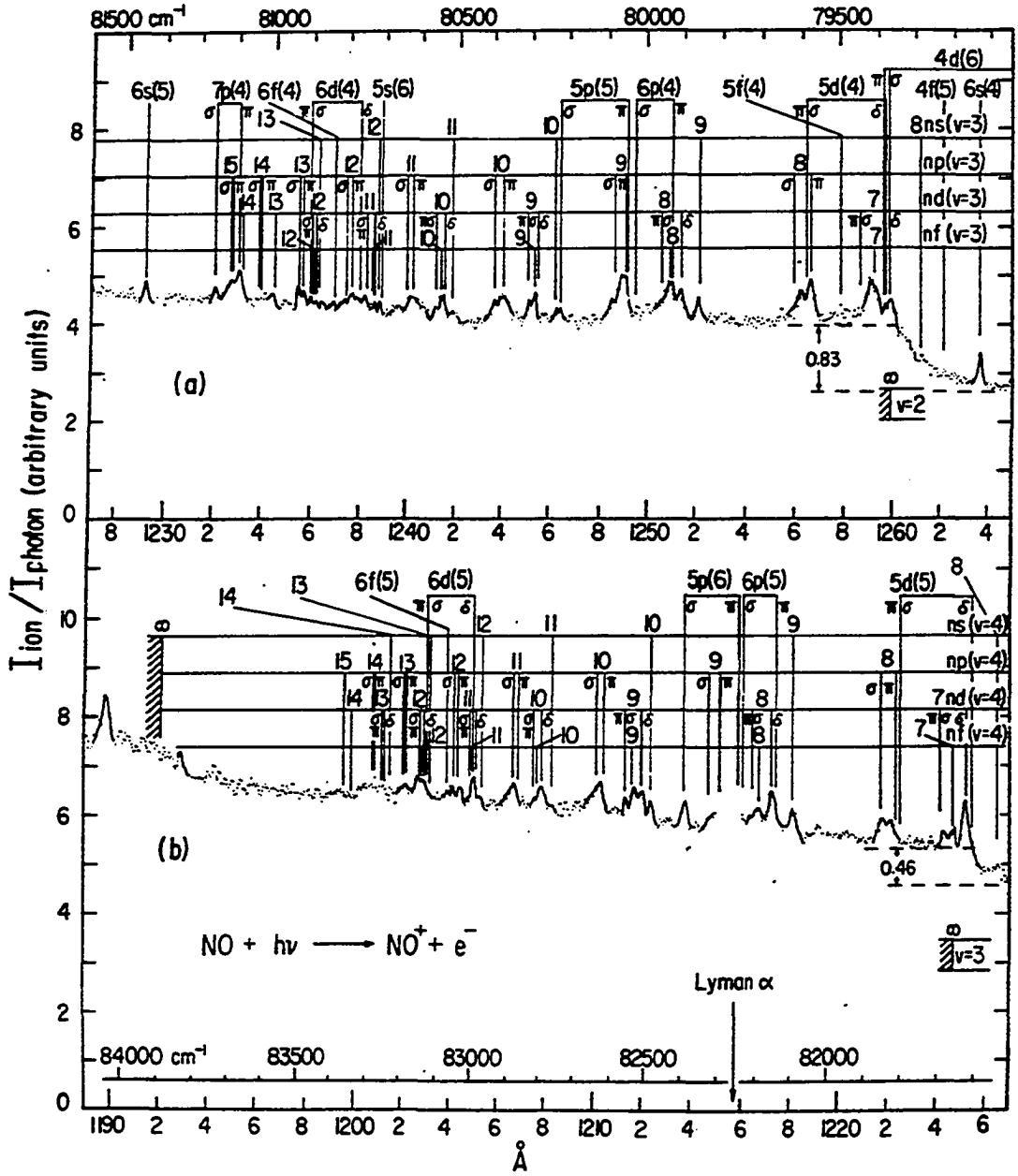

Figure 3. PIE curve for NO^+ obtained using the Ar continuum as the light source at a nozzle temperature of 150K and a nozzle stagnation pressure of ∿760 Torr (a) in the region 1227-1265 Å; (b) in the region 1189-1227 Å

uncertainty of the onset located in the present study is estimated to be <24 cm^{-1}. Therefore, the ionization potential of NO determined by the position of the first onset in the PIE curve for NO^+ is not consistent with the value deduced in Ref. 10. Further investigation is needed to clarify this discrepancy.

One of the uncertainties introduced in deducing the relative Franck-Condon factors from the step heights measured in a photoionization experiment is the ambiguity in correcting for the contribution from autoionization. At low resolution, autoionization peaks will not be completely resolved. Thus, it is not surprising to find that the Franck-Condon factors determined in photoionization are usually different from those derived from photoelectron spectroscopy. In the present experiment, the autoionization band structure in the region 1242-1340 Å seems to be quite well resolved. However, as the energy increases beyond 80515 cm^{-1} (1242 Å), the shape of the PIE curve gradually tilts upwards. The fifth step, which corresponds to the onset of the $NO(X^1\Sigma^+ v = 4) \leftarrow NO(X^2\Pi_{1/2})$ transition, is almost unrecognizable. Table 1 lists the relative Franck-Condon factors derived in this work and compared with the values obtained by other methods (16-18). The values determined in the present study are found to be in good agreement with those obtained in photoelectron spectroscopy (16,19) (Table 1).

The $^2\Pi_{3/2}$ state of NO is 124 cm^{-1} above the ground $^2\Pi_{1/2}$ state (20), hence, if a Boltzmann distribution is assumed, the ratio of the population of $NO(^2\Pi_{3/2})$ to that of $NO(^2\Pi_{1/2})$ is ~54% at 290K and ~30% at 150K. If the expansion process does not relax $NO(^2\Pi_{3/2})$, the relative

Table 1. Relative Franck-Condon factors (normalized for v = 1)

v	This Work (±0.03)	Photoelectron[a]	Calculated[b]
0	0.56	0.59	0.478
1	1.00	1.00	1.000
2	0.83	0.81	0.917
3	0.46[c]	0.40	0.484

[a]Ref. 16.

[b]Ref. 17 and 18.

[c]This value has been determined by adopting a base-line to compensate for the gradual rise of the PIE curve due to autoionization. The uncertainty of this value is, thus, much larger than 0.03.

intensities of the autoionization features originating from $^2\Pi_{1/2}$ and $^2\Pi_{3/2}$ should change correspondingly with the temperature. As shown in Figs. 1, 2(a) and 2(b), the structure of the 290K spectrum is very similar to that of the 150K except that the peak at 1337.47 Å becomes slightly stronger relative to other resonances in the 150K spectrum (21). A small step can be seen at 1341.5 Å (Fig. 1) which is about 124 cm^{-1} lower in energy than the first onset at 1339.32 Å. This step can be assigned to the threshold for the $NO^+(X^1\Sigma\ v = 0) \leftarrow NO(^2\Pi_{3/2})$ transition. By comparing the height of this step to that of the main step, an estimate for the population of $NO(^2\Pi_{3/2})$ to that of $NO(^2\Pi_{1/2})$ is ∿15% at the sampling region (22). This observation is consistent with the previous finding (23) that the relaxation from $^2\Pi_{3/2}$ to $^2\Pi_{1/2}$ is efficient.

Attempts to assign the autoionization structure were made by comparing the positions of the resonances resolved in the PIE curve with those of the Rydberg series (ns, npσ, npπ, nd and nf) observed in absorption (9,11). The nf levels are always close to the nd Rydberg levels and the assignments are uncertain. Many Rydberg levels which were not observed in previous absorption experiments in this spectral region have been calculated using the quantum defects of lower members of the appropriate Rydberg series (12). All the Rydberg levels in the region 1180-1255 Å were calculated. The series limits used were obtained from Miescher (10,13,24) and Alberti and Douglas (14). The data analysis employed here is similar to that of Ref. 11. A possible assignment of the autoionization structure is listed in Tables 2, 3, 4

Table 2. Autoionization peaks (I) superimposed on the first vibrational step of $NO^+(^1\Sigma^+ v = 0)$

I(cm^{-1})		A(cm^{-1})[a]	I-A(cm^{-1})	$n\ell\lambda(v)$[b]	Δv[c]
74695	(1338.77 Å)	74691	+ 4	8sσ(1)	-1
74768	(1337.47 Å)	74766	+ 2	4f(3)	-3
		74780	-12	7dδ(1)	-1
74790[d]	(1337.07 Å)	74780	+10	7dδ(1)	-1
74829	(1336.38 Å)	74818	+11	7f(1)	-1
74840[d]	(1336.18 Å)	74860[e]	-20	7dσ,π(1)	-1
74869	(1335.67 Å)	74860	+ 9	5dδ(2)	-2
74921	(1334.74 Å)	74929[e]	- 8	4dσ(3)	-3
74932[d]	(1334.54 Å)	74937[e]	- 5	4dπ(3)	-3
74960	(1334.04 Å)	74971	-11	5f(2)	-2
		74973[e]	-13	8pπ(1)	-1
74988	(1333.54 Å)	74973[e]	+15	8pπ(1)	-1
75011	(1333.14 Å)	75018	- 7	8pσ(1)	-1
75266	(1328.62 Å)	75261	- 1	9sσ(1)	-1
75326	(1327.57 Å)	75315	+11	8dδ(1)	-1

[a]Positions of Rydberg levels observed or calculated from absorption experiments (Ref. 9 and 11).

[b]n,ℓ,λ and (v) represents the principal, orbital angular momentum, projection (of ℓ along the internuclear axis) and vibrational quantum numbers, respectively.

[c]Δv = vibrational change in autoionization.

[d]Shoulder (unresolved).

[e]Calculated.

Table 2. Continued

I(cm^{-1})	A(cm^{-1})[a]	I-A(cm^{-1})	$n\ell\lambda(v)$[b]	Δv[c]
75346[d] (1327.21 Å)	74345	+ 1	8f(1)	-1
75372 (1326.75 Å)	75370[e]	+ 2	8dσ,π(1)	-1
75412 (1326.05 Å)	75400	+12	6pπ(2)	-2
75465 (1325.11 Å)	75460	+ 5	9pπ(1)	-1
75609 (1322.59 Å)	75620	-11	5pπ(3)	-3
75658 (1321.74 Å)	75657	+ 1	10sσ(1)	-1
75698 (1321.04 Å)	75690	+ 8	9dδ(1)	-1
	75690[e]	+ 8	4pπ(5)	-5
	75706	- 8	9f(1)	-1
75729 (1320.49 Å)	75728[e]	+ 1	9dσ,π(1)	-1
75799 (1319.27 Å)	75803	- 4	10pσ(1)	-1
75877 (1317.92 Å)	75872	+ 5	4pσ(5)	-5
75948 (1316.69 Å)	75932	+16	11sσ(1)	-1
	75960	-12	10dδ(1)	-1
	75965	-17	10f(1)	-1
75977 (1316.19 Å)	75965	+12	10f(1)	-1
	75988[e]	-11	10dσ,π(1)	-1
76114 (1313.82 Å)	76113	+ 1	7sσ(2)	-2
76126 (1313.62 Å)	76128[e]	- 2	12sσ(1)	-1
76153 (1313.15 Å)	76150[e]	+ 3	11dδ(1)	-1
76187 (1312.55 Å)	76170[e]	+17	11dσ,π(1)	-1
	76201[e]	-14	12pπ(1)	-1
76216 (1312.05 Å)	76210[e]	+ 6	12pσ(1)	-1
76251 (1311.45 Å)	76240	+11	6dδ(2)	-2
76301 (1310.60 Å)	76300[e]	+ 1	12dδ(1)	-1
	76301	0	12f(1)	-1

Table 2. Continued

I(cm^{-1})		A(cm^{-1})[a]	I-A(cm^{-1})	$n\ell\lambda(v)$[b]	Δv[c]
76321[d]	(1310.25 Å)	76316[e]	+ 5	12dσ,π(1)	-1
		76316	+ 5	5sσ(4)	-4
		76317	+ 4	6f(2)	-2
		76336[e]	-15	13pπ(1)	-1
76353	(1309.70 Å)	76344[e]	+ 9	13pσ(1)	-1
		76365	-12	6dσ,π(2)	-2
76415	(1308.65 Å)	76409	+ 6	13dδ(1)	-1
		76414	+ 1	13f(1)	-1
76508	(1307.05 Å)	76500[e]	+ 8	14dδ(1)	-1
		76503	+ 5	14f(1)	-1
76578	(1305.85 Å)	76573[e]	+ 5	15dδ(1)	-1
		76575	+ 3	15f(1)	-1
76596[d]	(1305.55 Å)	76590	+ 6	7pπ(2)	-2
76643	(1304.75 Å)	76650	- 7	7pσ(2)	-2
76893	(1300.50 Å)	76890	+ 3	6sσ(3)	-3
76984	(1298.98 Å)	77002	-18	8sσ(2)	-1

Table 3. Autoionization peaks (I) superimposed on the second vibrational step of $NO^+(^1\Sigma^+ v = 1)$

I(cm^{-1})		A(cm^{-1})	I-A(cm^{-1})	nℓλ(v)	Δv
77019	(1298.38 Å)	77011	+ 8	4f(4)	-3
77102	(1296.98 Å)	77085	+17	7dδ(2)	-1
77144	(1296.28 Å)	77130	+14	7f(2)	-1
		77150	- 6	5dδ(3)	-2
77167[a]	(1295.88 Å)	77165[b]	+ 2	7dσ,π(2)	-1
		77170[b]	- 3	4dσ(4)	-3
		77178	-11	4dπ(4)	-3
77235	(1294.75 Å)	77248	-13	5f(3)	-2
77276	(1294.06 Å)	77290	-14	8pπ(2)	-1
77330	(1293.16 Å)	77332	- 2	8pσ(2)	-1
77348[a]	(1292.86 Å)	77358[b]	-10	5dσ,π(3)	-2
77578	(1289.02 Å)	77572	+ 6	9sσ(2)	-1
77635[a]	(1288.08 Å)	77630	+ 5	8dδ(2)	-1
77656[a]	(1287.73 Å)	77657	- 1	8f(2)	-1
77674	(1287.43 Å)	77670	+ 4	6pπ(3)	-2
		77685	-11	8dσ,π(2)	-1
77753	(1286.13 Å)	77752	+ 1	9pπ(2)	-1
		77760	- 7	6pσ(3)	-2
77770[a]	(1285.83 Å)	77760	+10	6pσ(3)	-2
77854	(1284.46 Å)	77850	+ 4	5pπ(4)	-3
77964	(1282.64 Å)	77962	+ 2	10sσ(2)	-1

[a]Shoulder (unresolved).

[b]Calculated.

Table 3. Continued

I (cm^{-1})		A (cm^{-1})	I-A (cm^{-1})	nℓλ(v)	Δv
78001	(1282.04 Å)	78000[b]	+ 1	5pσ(4)	-3
		78000	+ 1	9dδ(2)	-1
78019	(1281.74 Å)	78018	+ 1	9f(2)	-1
78031[a]	(1281.54 Å)	78038[b]	- 7	9dσ,π(2)	-1
78110	(1280.24 Å)	78090[b]	+20	10pπ(2)	-1
		78118	- 8	10pσ(2)	-1
78244	(1278.05 Å)	78237	+ 7	11sσ(2)	-1
78263[a]	(1277.75 Å)	78270[b]	- 7	10dδ(2)	-1
78280	(1277.45 Å)	78270[b]	+10	10dσ(2)	-1
		78276	+ 4	10f(2)	-1
78299	(1277.15 Å)	78298	+ 1	10dσ,π(2)	-1
78327	(1276.70 Å)	78337[b]	-10	11pπ(2)	-1
78348	(1276.35 Å)	78348[b]	0	11pσ(2)	-1
78400	(1275.51 Å)	78391	+ 9	7sσ(3)	-2
78437	(1274.91 Å)	78438	- 1	12sσ(2)	-1
78479	(1274.22 Å)	78460[b]	+19	11dδ(2)	-1
		78467	+12	11f(2)	-1
		78480[b]	- 1	11dσ,π(2)	-1
78519	(1273.57 Å)	78513[b]	+ 6	12pπ(2)	-1
		78516[b]	+ 3	5sσ(5)	-4
		78522[b]	- 3	12pσ(2)	-1
		78530	-11	6dδ(3)	-2
78590[a]	(1272.43 Å)	78590	0	13sσ(2)	-1
		78596	- 6	6f(3)	-2
78608	(1272.13 Å)	78596	+12	6f(3)	-2
		78605[b]	+ 3	12d(1)	-1
		78611	- 3	12f(1)	-1

Table 3. Continued

I(cm^{-1})	A(cm^{-1})	I-A(cm^{-1})	$n\ell\lambda(v)$	Δv
78849 (1268.24 Å)	78850	- 1	$7p\pi(3)$	-2
78905 (1267.34 Å)	78910[b]	- 5	$7p\sigma(3)$	-2
79136 (1263.64 Å)	79134	+ 2	$6s\sigma(4)$	-3

Table 4. Autoionization peaks (I) superimposed on the third vibrational step of $NO^+(^1\Sigma^+ v = 2)$

I (cm^{-1})		A (cm^{-1})[a]	I-A (cm^{-1})	nℓλ(v)	Δv
79378	(1259.80 Å)	79375	+ 3	7dδ(3)	-1
		79385	- 7	5dδ(4)	-2
		79385	- 7	4dσ(5)	-3
		79393	-15	4dπ(5)	-3
79417	(1259.17 Å)	79409	+ 8	7f(3)	-1
79579	(1256.62 Å)	79570	+ 9	8pπ(3)	-1
		79593	-14	5dσ,π(4)	-2
79607	(1256.17 Å)	79613	- 6	8pσ(3)	-1
79865	(1252.12 Å)	79854	+11	9s(3)	-1
79912	(1251.37 Å)	79910	+ 2	8dδ(3)	-1
79938	(1250.97 Å)	79930	+ 8	6pπ(4)	-2
		79941	- 3	8f(3)	-1
80060	(1249.07 Å)	80045	+15	5pπ(5)	-3
		80051	+ 9	8pπ(3)	-1
80088[b]	(1248.62 Å)	80076	+12	9pσ(3)	-1
80277	(1246.47 Å)	80225	+ 2	5pσ(5)	-3
80239	(1246.27 Å)	80238	+ 1	10sσ(3)	-1
80291	(1245.47 Å)	80280	+11	9dδ(3)	-1
		80301	-10	9f(3)	-1
80314	(1245.12 Å)	80301	+13	9f(3)	-1
		80318	- 4	9dσ,π(3)	-1
80385	(1244.02 Å)	80379	+ 6	10pπ(3)	-1

[a]All positions of the Rydberg levels are calculated except 5dδ(4).

[b]Shoulder (unresolved).

Table 4. Continued

I(cm^{-1})		A(cm^{-1})[a]	I-A(cm^{-1})	nℓλ(v)	Δv
80404	(1243.72 Å)	80399	+ 5	10pσ(3)	-1
80520	(1241.92 Å)	80513	+ 7	11sσ(3)	-1
80550	(1241.47 Å)	80543	+ 7	10dδ(3)	-1
		80559	- 9	10f(3)	-1
80569[b]	(1241.17 Å)	80571	- 2	10dσ,π(3)	-1
80628	(1240.27 Å)	80616	+12	11pπ(3)	-1
		80630	- 2	11pσ(3)	-1
80722	(1238.82 Å)	80714	+ 8	5sσ(6)	-4
		80729	- 7	12sσ(3)	-1
80735	(1238.62 Å)	80729	+ 6	12sσ(3)	-1
		80735	0	11dδ(3)	-1
		80749	-14	11f(3)	-1
80761	(1238.22 Å)	80749	+12	11f(3)	-1
		80755	+ 6	11dσ,π(3)	-1
80784	(1237.87 Å)	80780	+ 4	6dδ(4)	-2
		80792	- 8	12pπ(3)	-1
80797	(1237.67 Å)	80792	+ 5	12pπ(3)	-1
		80801	- 4	12pσ(3)	-1
80931	(1235.62 Å)	80927	+ 4	13pπ(3)	-1
80941	(1235.47 Å)	80934	+ 7	13pσ(3)	-1
81010	(1234.42 Å)	80999	+11	13dδ(3)	-1
		81006	+ 4	13f(3)	-1
81102	(1233.02 Å)	81090	+12	14dδ(3)	-1
		81096	+ 6	14f(3)	-1
		81100	+ 2	7pπ(4)	-2
81125[b]	(1232.67 Å)	81117	+ 8	15pπ(3)	-1
		81122	+ 3	15pσ(3)	-1

Table 4. Continued

I(cm^{-1})	A(cm^{-1})[a]	I-A(cm^{-1})	nℓλ(v)	Δv
81168 (1232.02 Å)	81170	- 2	7pσ(4)	-2
81352 (1229.22 Å)	81353	- 1	6sσ(5)	-3

and 5. In many cases, multiple assignments are still unavoidable. In general, the correlation as shown in Fig. 2(a), 2(b), 3(a), and 3(b) is quite satisfactory and all peaks in the PIE curve can be accounted for as originating from $NO(X^2\Pi_{1/2})$. This also supports the earlier discussion about the efficient relaxation of $NO(^2\Pi_{3/2})$ in a supersonic expansion. The only exception is a peak at 74695 cm^{-1} (1338.77 Å) which is found to be very close to the 8sσ Rydberg level observed at 14691.1 cm^{-1}. The origin of this peak is not clear, since it is lower in energy than the ionization potential of NO as deduced from high resolution absorption in this region (10,25).

Figures 2(a), 2(b), 3(a) and 3(b) are intentionally arranged to bring out the similarity of the structure on different vibrational steps despite the differences in relative intensity. This similarity has helped in assigning the structure on vibrational steps v = 2 and 3.

From the analysis, autoionization resonances due to $\Delta v < -1$ transitions are clearly evident. Consistent with the observation in absorption experiments that most of the np-X bands and many ndδ-X bands are diffuse, many of the strong peaks in the PIE curve are found to correlate quite well with np and ndδ levels. Some Rydberg levels which have not been observed in absorption are also evident. The strong peak at 74921 cm^{-1} (1334.74 Å) is most likely to arise from the 4dσ, π(3) levels. Although the ns and nf rotational levels that appear in absorption are sharp within the instrumental width of 0.1 cm^{-1}, this fact itself does not exclude the possibility of the autoionization of these levels. In fact,

Table 5. Autoionization peaks (I) superimposed on the fourth vibrational step of $NO^+(^1\Sigma^+ v = 3)$

I (cm^{-1})		A (cm^{-1})[a]	I-A (cm^{-1})	$n\ell\lambda(v)$	Δv
81621	(1225.17 Å)	81601	+20	5dδ(5)	-2
		81615	+ 6	7dδ(4)	-1
81655	(1224.67 Å)	81662	- 7	7f(4)	-1
81688	(1224.17 Å)	81695	- 7	7dσ,π(4)	-1
81828	(1222.07 Å)	81809	+19	5dσ,π(5)	-2
		81820	+ 8	8pπ(4)	-1
81855	(1221.67 Å)	81865	-10	8pσ(4)	-1
82100	(1218.02 Å)	82098	+ 2	9sσ(4)	-1
82154	(1217.22 Å)	82150	+ 4	6pπ(5)	-2
		82156	- 2	8dδ(4)	-1
82192	(1216.67 Å)	82187	+ 5	8f(4)	-1
82391	(1213.72 Å)	82391	0	5pσ(6)	-3
82490	(1212.27 Å)	82485	+ 5	10sσ(4)	-1
82517	(1211.87 Å)	82525	- 8	9dδ(4)	-1
82538	(1211.57 Å)	82547	- 9	9f(4)	-1
82558	(1211.27 Å)	82563	- 5	9dσ,π(4)	-1
82633	(1210.17 Å)	82622	+11	10pπ(4)	-1
		82641	- 8	10pσ(4)	-1
82763[b]	(1208.27 Å)	82759	+ 4	11sσ(4)	-1
82794[b]	(1207.82 Å)	82788	+ 6	10dδ(4)	-1

[a] Calculated.

[b] Shoulder (unresolved).

Table 5. Continued

I(cm^{-1})		A(cm^{-1})[a]	I-A(cm^{-1})	nℓλ(v)	Δv
82811	(1207.57 Å)	82816	- 5	10dσ,π(4)	-1
82873	(1206.67 Å)	82860	+13	11pπ(4)	-1
		82874	- 4	11pσ(4)	-1
82976[b]	(1205.17 Å)	82961	+11	12sσ(4)	-1
82990	(1204.97 Å)	82983	+ 7	11dδ(4)	-1
		82992	- 2	6dδ(4)	-2
		83003	-13	11dσ,π(4)	-1
83031	(1204.37 Å)	83036	- 5	12pπ(4)	-1
83052	(1204.07 Å)	83047	+ 5	12pσ(4)	-1
83065	(1203.87 Å)	83068	- 3	6f(5)	-2
83141	(1202.77 Å)	83117	+14	6dσ,π(5)	-2
		83131	+10	12dδ(4)	-1
		83147	- 6	12dσ,π(4)	-1
83183	(1202.17 Å)	83172	+11	13pπ(4)	-1
		83180	+ 3	12pσ(4)	-1

there are many peaks in the spectrum that can be definitely identified as ns levels.

One of the most important objectives of this experiment, besides identifying the Rydberg levels, is to examine the autoionization processes and coupling mechanisms between the excited Rydberg states, ionic states and dissociative states. The strength of the band near 76596 cm^{-1} (1305.55 Å) is most likely due to the $7p\pi(2)$ Rydberg level which must autoionize via a $\Delta v = -2$ autoionization process. The band is found to be at least as strong as other autoionization peaks which autoionize by the $\Delta v = -1$ processes. It is interesting to compare the PIE curve with the photoelectrically scanned absorption spectrum of NO (11,26). As shown in Fig. 2 of Ref. 11, the $7p\pi(2)$ broad absorption band is also comparable in strength with other np and nd levels which converge to $v = 1$. If autoionization by $\Delta v = -1$ is a more favorable process than those via $\Delta v < -1$, one would expect the peak corresponding to the $7p\pi(2)$ level in the PIE curve to be reduced relative to the Rydberg levels converging to $v = 1$, contrary to the experimental observation. This suggests that autoionization via $\Delta v = -1$ processes are not strongly favored as compared to $\Delta v < -1$ processes in NO.

REFERENCES

1. K. Watanabe, F. F. Marmo and E. C. Y. Inn, Phys. Rev. 91, 1155 (1953).

2. K. Watanabe, J. Chem. Phys. 22, 1564 (1954).

3. K. Watanabe, F. M. Matsunaga and H. Sakai, Appl. Opt. 6, 391 (1967).

4. H. Hurzeler, M. G. Inghram and J. D. Morrison, J. Chem. Phys. 28, 76 (1958).

5. A. J. C. Nicholson, J. Chem. Phys. 43, 1171 (1965).

6. R. M. Reese and H. M. Rosenstock, J. Chem. Phys. 44, 2007 (1966).

7. P. C. Killgoar, Jr., G. E. Leroi, J. Berkowitz and W. A. Chupka, J. Chem. Phys. 58, 803 (1973).

8. C. Y. Ng, B. H. Mahan and Y. T. Lee, J. Chem. Phys. 65, 1956 (1976).

9. E. Miescher and F. Alberti, J. Chem. Phys. Ref. Data 5, 309 (1976).

10. E. Miescher, Can. J. Phys. 54, 1074 (1976).

11. E. Miescher, Y. T. Lee and P. Gürtler, J. Chem. Phys. 68, 2753 (1978).

12. E. Miescher and K. P. Huber, Electronic Spectrum of the NO Molecule. International Review of Science, Physical Chemistry (2), (Butterworths, London, 1976), Vol. 3, p. 37.

13. E. Miescher, Helv. Phys. Acta 29, 135 (1956).

14. F. Alberti and A. E. Douglas, Can. J. Phys. 53, 1179 (1975).

15. The rotational temperature of CS_2 achieved in a supersonic expansion under similar nozzle conditions was estimated to be $\leq$20K by the sharpness of the first onset in the PIE curve for CS_2^+ (Section 2).

16. D. A. S. Vroom, Ph.D. Thesis, The University of British Columbia, 1966.

17. M. E. Wacks, J. Chem. Phys. 41, 930 (1964).

18. M. Halmann and I. Lanlicht, J. Chem. Phys. 43, 1503 (1965).

19. The Franck-Condon factors obtained by PES at 584 Å need not be the same as those obtained by measuring the step heights at threshold in photoionization. They could be the same if the cross section for each step was independent of energy over a range of a few eV.

20. R. H. Gillette and E. H. Eyster, Phys. Rev. 56, 1113 (1939).

21. A PIE curve (1330-1342 Å) for NO^+ has also been obtained at a nozzle temperature of ~600K; autoionization features are found to be suppressed and poorly resolved in the 600K spectrum and, thus, are not helpful for this comparison.

22. The influence on the accuracy of the ionization potential of NO, determined in this experiment by the unrelaxed $NO(^2\Pi_{1/2})$ molecules, is unknown.

23. Ref. 8 of Ref. 11.

24. We have not been able to fit the autoionization features observed in the PIE curve for NO^+ by using the positions of the onsets determined in the present experiment as the series limits and the quantum defects from Ref. 12.

25. If the ionization potential of NO is 74721 cm^{-1} as deduced in Ref. 10, one possible explanation for the peak observed at 74695 cm^{-1} is that it is due to rotationally excited NO molecules. The absorption line observed at 74691.1 cm^{-1} is specified as Q_{11} (3 1/2) in Ref. 9, and it is below the ionization energy (74721 cm^{-1}) by 26 cm^{-1}. The molecule that absorbs at this energy is in the rotational state J = 3 1/2 of 8sσ (1). The core, therefore, has the rotational energy $F_{rot} = BR(R+1)$, where B = 2 cm^{-1} is the rotational constant of the Rydberg state, and R = J-1/2 = 3. Thus, F_{rot} = 24 cm^{-1} is approximately the additional energy needed for ionization.

26. The photoelectrically scanned absorption spectrum reported in Ref. 11 has not been corrected for the spectral distribution of the synchrotron light source and the response of the detector. However, a substantial change in relative intensity is not expected in a small spectral range after the corrections.

SECTION II.

A PHOTOIONIZATION STUDY OF CARBON DISULFIDE AND ITS CLUSTERS

INTRODUCTION

It has been shown recently, in a series of molecular beam photoionization experiments (1-14), that by using the supersonic beam method to relax the rotational envelope of the target gases, higher resolution PIE data for condensible gases can be obtained. Van der Waals dimers and clusters produced in a free jet expansion are excellent molecular precursors for the investigation of ion-neutral interaction energies. Photoionization of these precursors produce molecular ions which cannot be obtained from ordinary stable molecules, thus making it a useful means of determining thermochemical quantities. From the point of view of chemical dynamics, photoionization of dimers offers a direct and general route for preparation of collision complexes and allows direct measurements of fragmentation channels of these complexes as a function of internal excitation, hence it is a valuable tool for the investigation of ion-molecule reaction dynamics.

Unfortunately, molecular beam photoionization experiments are subject to more severe sensitivity problems than conventional gas cell experiments. In order to maintain a "collision free" environment in the ionization region, extensive differential pumping is required which limits the number density of target gas molecules at the collision center to a density of $\sim$0.1 to 1 m Torr as compared to $\geq$10 m Torr employed in gas cell studies. Furthermore, the concentration of dimers and higher clusters formed in the beam is usually only a fraction of that of the monomer. This and the low intensity of available VUV photons make photoionization studies of van der Waals molecules difficult. The

highest resolution PIE data (3) obtained previously using the molecular beam method correspond to 0.83 Å (FWHM), whereas in conventional photoionization studies, a photon bandwidth of 0.14 Å (FWHM) is used routinely. The signal level of the previous dimer experiments generally ranged from ∿0.1 c/s to ∿1000 c/s at optical resolutions of 1 to 3 Å. Near the ionization thresholds where the Franck-Condon factors are unfavorable and the photoionization cross sections are small, there is evidence that the low signal level may prevent the determination of the true adiabatic ionization potentials of the dimer ions. Therefore, it is fair to assert that the full potential of the molecular beam photoionization method can only be realized if the sensitivity of the method can be improved substantially. In this paper, the results obtained using the new molecular beam photoionization apparatus to study carbon disulfide, carbon disulfide dimer and clusters are reported. Judging from the signal level obtained using this new apparatus, an improvement of about three orders of magnitude in sensitivity has been achieved over that (10) used previously for the study of this system. Experiments performed on NO in the region 1350-1250 Å also indicate that this apparatus is about two orders of magnitude more sensitive than the one described by Ng et al. (3) using the same optical resolution.

In 1979, Trott, Blais and Walters (14) published PIE data for CS_2^+ and $(CS_2)_2^+$ from 1000 to 1295 Å. From the measured monomer and dimer IE's, they deduced the binding energy of $CS_2^+ \cdot CS_2$ to be 11.3 kcal/mol which is significantly below the enthalpy change at ∿620K for the CS_2^+-CS_2 ion-molecule association reaction ($-\Delta H^\circ_{f620}$ = 21.9 ± 2.5 kcal/mol)

determined in a pulsed high pressure mass spectrometric experiment by Meot-Ner and Field (15). In comparing the monomer and dimer PIE data, Trott et al. observed a very close correspondence of autoionization features of both species in the region 1000-1050 Å. In contrast, autoionization structure in the PIE data for $(CS_2)_2^+$ between 1100-1125 Å was markedly shifted in energy and broadly distributed. These changes were interpreted in terms of the geometry of the carbon disulfide dimer. Due to the low signal intensity, only a few data points were obtained in the region 1000-1050 Å. In order to explore fully the implication of these changes, it is necessary to investigate this system at a higher signal-to-noise level and to extend the measurements to higher members of Rydberg series III and IV. This system has been re-examined at a higher resolution in the wavelength region 650 to 1350 Å and photoionization data with better statistics have been obtained. Because of the improved sensitivity of the present instrument, we have also been able to include a study of $(CS_2)_n^+$ where n is 3, 4 and 5.

EXPERIMENTAL

The CS_2 molecular beam was produced by seeding CS_2 vapor (~270 Torr) at approximately 18°C in 450 Torr of Ar, then expanding the mixture through a 70 μm diameter nozzle. Mallinckrodt analytical grade CS_2 was used without further purification. The Ar used in this experiment was obtained from Matheson (≥99.995% Ar).

The PIE curves for CS_2^+ near the threshold (1232-1210 Å and 1075-1130 Å) were obtained using an optical resolution of 0.14 Å (FWHM) and the Ar continuum as the light source. Data are plotted at intervals of 0.05 Å. The remainder of the PIE curves in this experiment were obtained using a resolution of 1.4 Å (FWHM). The counting rates at 1050 Å for $(CS_2)_2^+$, $(CS_2)_3^+$, $(CS_2)_4^+$, and $(CS_2)_5^+$ were about 18,000 c/s, 4,300 c/s, 3,100 c/s, and 1,800 c/s, respectively. The counting time varied from 5 to 50s. Each PIE curve was based on at least two scans and the detailed structure in the curves was found to be reproducible.

RESULTS AND DISCUSSION

The PIE curve for CS_2^+ near the threshold (1210-1232 Å) is depicted in Fig. 1(a). The coarse structure of the PIE curve is similar to that obtained by Trott et al. (14). Since the resolution used in this experiment was ten times better than that previously used to study this system, the step function behavior is much more apparent. Nine autoionization peaks are resolved on the first vibration step of the PIE curve for CS_2^+. Four of the autoionization resonances are found to be coincident with previously observed members of Rydberg series I (16,17) which converge to the spin-orbit state, $^2\Pi_{1/2}$, of CS_2^+. The positions of these autoionization peaks are listed and compared in Table 1 with the corresponding Rydberg transitions observed in absorption (17). The assignment of the principal quantum numbers for members of this series is based on the recent studies by Larzilliere and Damany (18) and Greening and King (19). One of the most interesting results of this study is the identification of the Rydberg member, n = 16, of series I as a strong autoionization peak in the PIE curve for CS_2^+. Since the position in energy of this resonance is 81274 cm^{-1}, this observation essentially supercedes any previous measurements (16,17,20,21) which are higher than this value.

The rotational temperature of CS_2 achieved in a supersonic expansion under the present conditions can be estimated by the sharpness of the first onset. The uncertainty of the initial threshold was found to be 0.25 Å (0.0020 eV) which corresponds to a rotational temperature of $\leq$20K. Thus, the IE's for the ground state $X^2\Pi_{3/2}$, and the $^2\Pi_{1/2}$ state

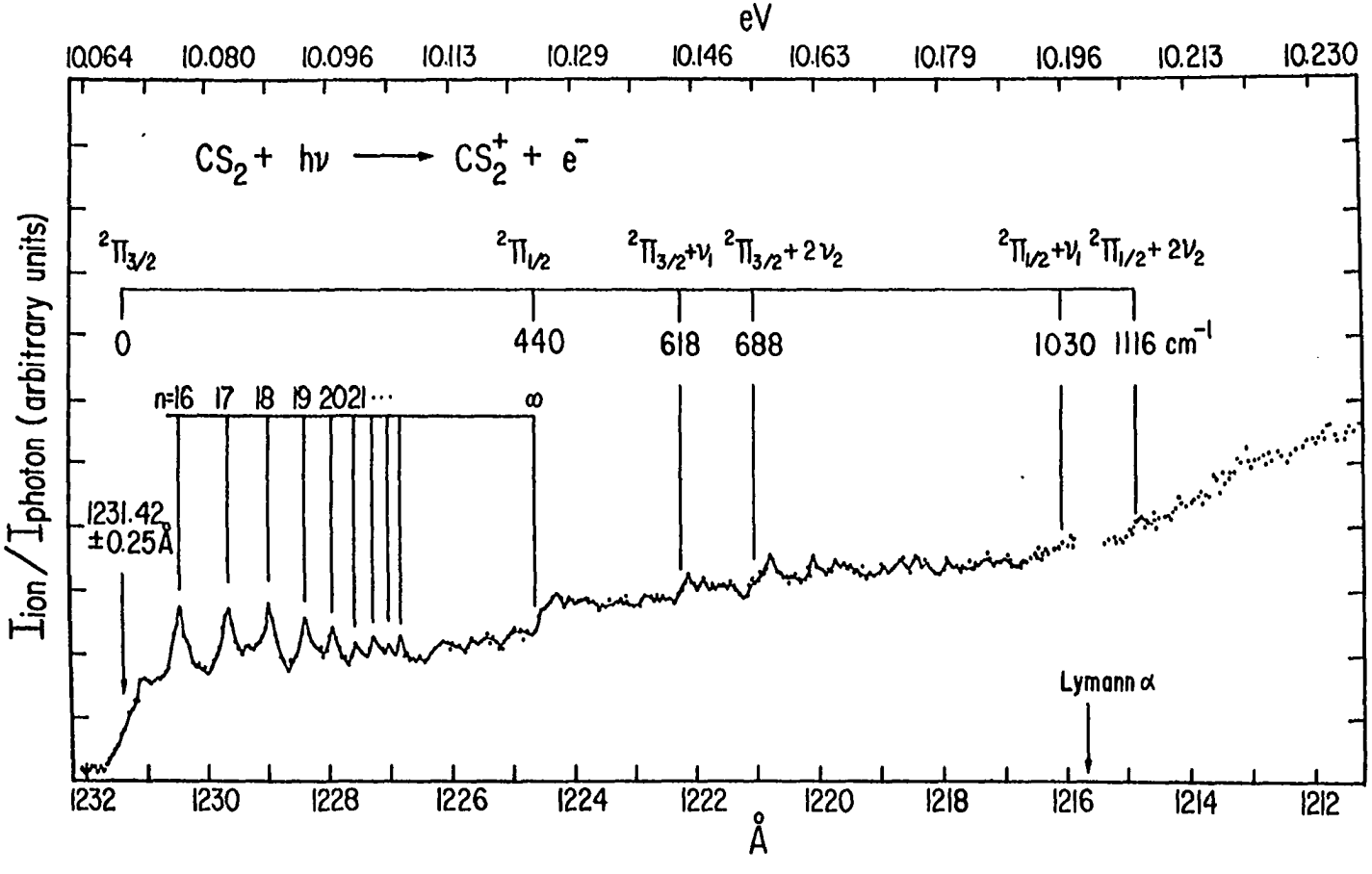

Figure 1a. PIE curve for CS_2^+ in the region 1210-1232 Å obtained with a photon bandwidth of 0.14 Å (FWHM) and using the Ar continuum as the light source

Table 1. Rydberg series I of CS_2

n[a]	ν(cm^{-1}) This Work (±10 cm^{-1})	Ref. 7
16	81274 (1230.4 Å)	81281
17	81327 (1229.6 Å)	81327
18	81377 (1228.85 Å)	81371
19	81410 (1228.35 Å)	81409
20	81440 (1227.9 Å)	--
21	81463 (1227.55 Å)	--
22	81483 (1227.25 Å)	--
23	81500 (1227.0 Å)	--
24	81513 (1226.8 Å)	--
	IE. ($^2\Pi_{1/2}$) = 81650 ± 16 cm^{-1}	

[a]Refs. 18 and 19.

are determined to be 10.0685 ± 0.0020 eV and 10.1230 ± 0.0020 eV, respectively. These values are in excellent agreement with values derived from photoelectron spectroscopy (22) and photoionization studies (14, 23). The spin-orbit splitting is determined to be 440 ± 32 cm^{-1} which is again consistent with previous measurements (14,16,17,22,23).

With the assistance of previous studies (14,21,24,25,26), satisfactory assignments of the PIE curve for CS_2^+ in this region can be obtained. According to the selection rules, the symmetric stretching mode for CS_2^+, ν_1, can appear in a single quantum while the bending mode of CS_2^+, ν_2, appear in double quanta. As shown in Fig. 1(a), the slight steps at 618, 688, 1030 and 1116 above the first onset are attributed to the onsets of $^2\Pi_{3/2} + \nu_1$, $^2\Pi_{3/2} + 2\nu_2$, $^2\Pi_{1/2} + \nu_1$ and $^2\Pi_{1/2} + 2\nu_2$, respectively. Therefore, $\nu_1(^2\Pi_{3/2})$, $\nu_2(^2\Pi_{3/2})$, $\nu_1(^2\Pi_{1/2})$ and $\nu_2(^2\Pi_{1/2})$ determined in this experiment are 618 ± 32 cm^{-1}, 344 ± 32 cm^{-1}, 590 ± 32 cm^{-1} and 338 ± 32 cm^{-1}, respectively.

It appears that autoionization contributes significantly to the first step, and if the resolution used in this study is still not high enough to completely resolve the autoionization structure, then the relative heights of the first and second steps may not give the relative Franck-Condon factors for the transition from the neutral ground state to the ionic $^2\Pi_{3/2}$ and $^2\Pi_{1/2}$ states, however, the heights of the steps which correspond to excitation to the states, $\tilde{X}^2\Pi_{3/2} + \nu_1$ and $\tilde{X}^2\Pi_{3/2} + 2\nu_2$, are substantially smaller than that of the first step, thus revealing the nonbonding nature of the $\tilde{X}^2\Pi_g$ state of CS_2.

Due to the nature of the H_2 many-lined pseudocontinuum, there has been concern about the suitability of using it as the light source for high resolution studies. Since the H_2 pseudocontinuum is more economical, easier to operate, and the average output light intensity is higher than other laboratory light sources in the region 1000-1600 Å, its performance as a light source for higher resolution experiments has been examined. Figure 1(b) shows the PIE curve for CS_2^+ in the region 1210-1232 Å obtained with a photon band width of 0.28 Å (FWHM) using the H_2 pseudocontinuum as the light source. All the main features which are resolved in Fig. 1(a) are also evident in Fig. 1(b). Based on our experience, the reliability of the H_2 pseudocontinuum for higher resolution works depends on the accuracy of measuring the light intensity. With proper compensation for the photomultiplier noise and scattered background light, satisfactory photoionization data can be obtained using this light source.

The PIE curve for CS_2^+ in the region 1075-1130 Å obtained with an optical resolution of 0.14 Å (FWHM) is shown in Fig. 2. Progressions of broad vibrational bands of CS_2 can be observed which was also evident in previous photoionization studies (14,23,27). The first two resonances at 89542 cm^{-1} (1116.8 Å) and 89928 cm^{-1} (1112.0 Å) are coincident with the members of Rydberg series III, n = 4, observed in absorption (17). The remaining features arise by autoionization from different vibrational states of the $\tilde{J}$ electronic state (28) of CS_2. Table 2 lists the centers of the bands and compares them with those reported in Ref. 17. Because of the diffuseness of these bands, and probably due to the

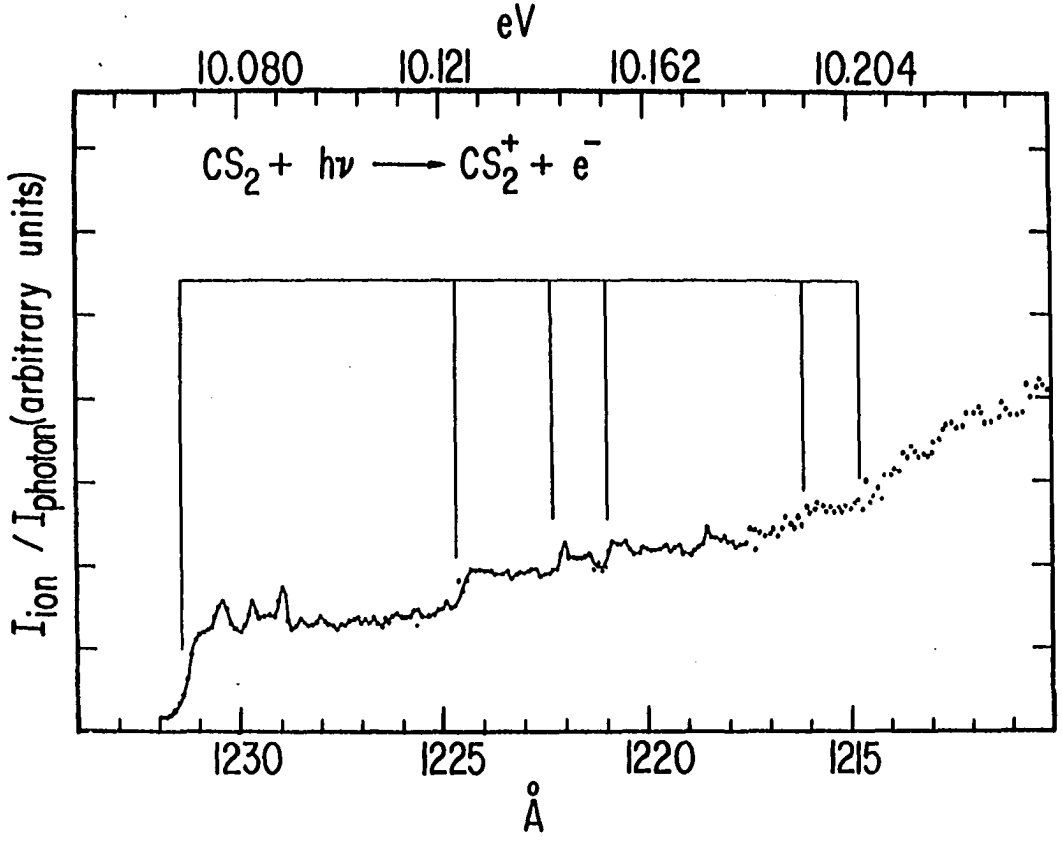

Figure 1b. PIE curve for CS_2^+ in the region 1210-1232 Å obtained with a photon bandwidth of 0.28 Å (FWHM) and using the H_2 many-lined pseudocontinuum as the light source

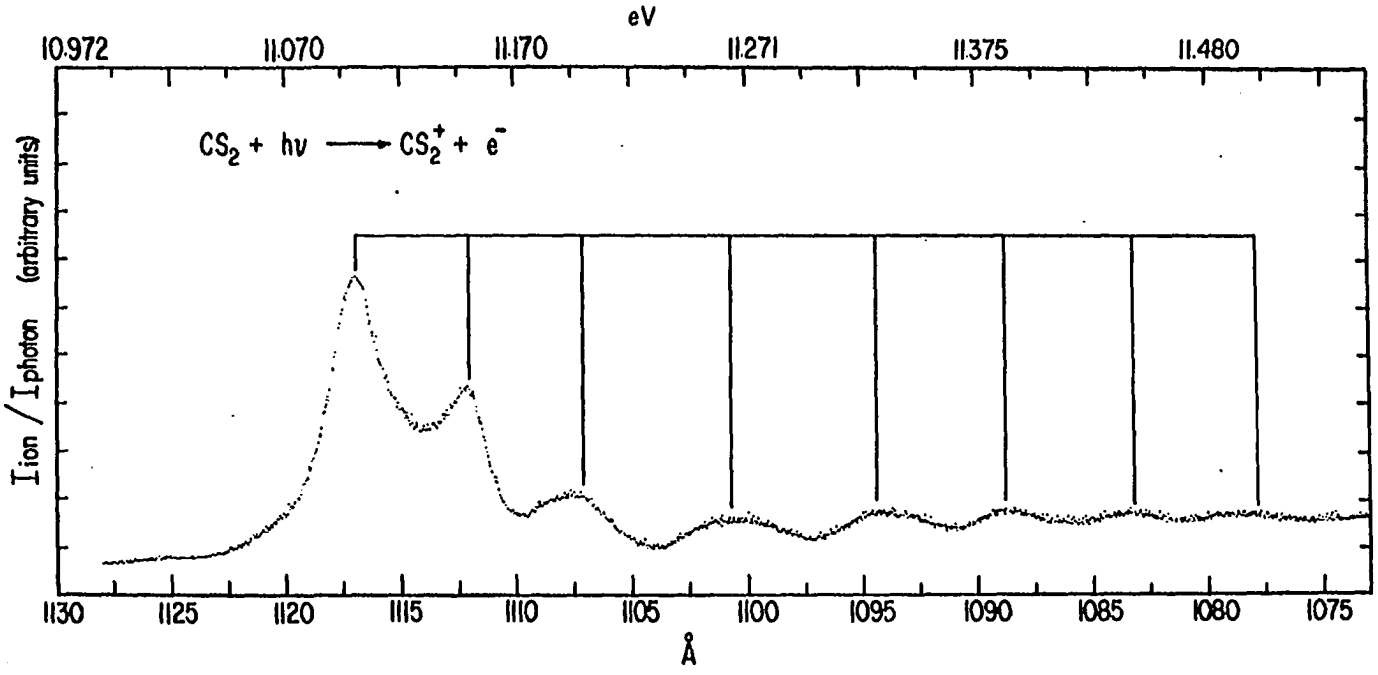

Figure 2. PIE curve for CS_2^+ in the region 1075-1130 Å obtained with a photon bandwidth of 0.14 Å (FWHM)

Table 2. Progression of absorption bands of CS_2

This Work		Ref. 17	
$\nu(cm^{-1})$	$\Delta\nu(cm^{-1})$	$\nu(cm^{-1})$	$\Delta\nu(cm^{-1})$
--		88834	
90326		90293	
	525		525
90851		90818	
	514		515
91365		91333	
	496		486
91861		91819	
	475		474
92336		92293	
	454		489
92790		92782	
			482
--		93266	
	$\Delta\nu_{Av} = 493$		$\Delta\nu_{Av} = 495$

different rotational and vibrational temperatures of CS_2 employed in the two experiments, the positions of the corresponding bands resolved in both experiments are slightly different. A smooth vibrational progression can be seen in Table 2 from the analysis of the results of the present experiment. The analysis gives an average vibrational spacing of 493 cm^{-1} for the $\tilde{J}$ state of CS_2, which is in excellent agreement with the previous value. Autoionization features corresponding to absorption bands observed previously at 88834 cm^{-1} and 93266 cm^{-1}, however, cannot be found in the PIE curve for CS_2^+.

Figure 3(a) shows the PIE curve for $(CS_2)_2^+$ in the region 970-1350 Å which is found to be in general agreement with that obtained previously (14). The PIE near the threshold is approximately four orders of magnitude smaller than the strong resonance at 1035 Å. The measured IE for $(CS_2)_2^+$ in this experiment is 9.36 ± 0.02 eV, compared to a previous value of 9.63 eV (14). This, together with the IE of CS_2 and the binding energy, 0.05 eV, of $(CS_2)_2$ derived by using second virial coefficients (14,29) are used to calculate a binding energy of 0.76 ± 0.04 eV (17.5 ± 1 kcal/mol) between CS_2^+ and CS_2. Because of the high degree of rotational and low frequency vibrational relaxation in the supersonic expansion, this value can be taken to be the enthalpy change, ΔH°_{fo}, for the ion-molecule association reaction

$$CS_2^+ + CS_2 \rightarrow CS_2^+ \cdot CS_2$$

at 0K. The enthalpy change at approximately 620K for this reaction has been measured recently in a high pressure mass spectrometry experiment

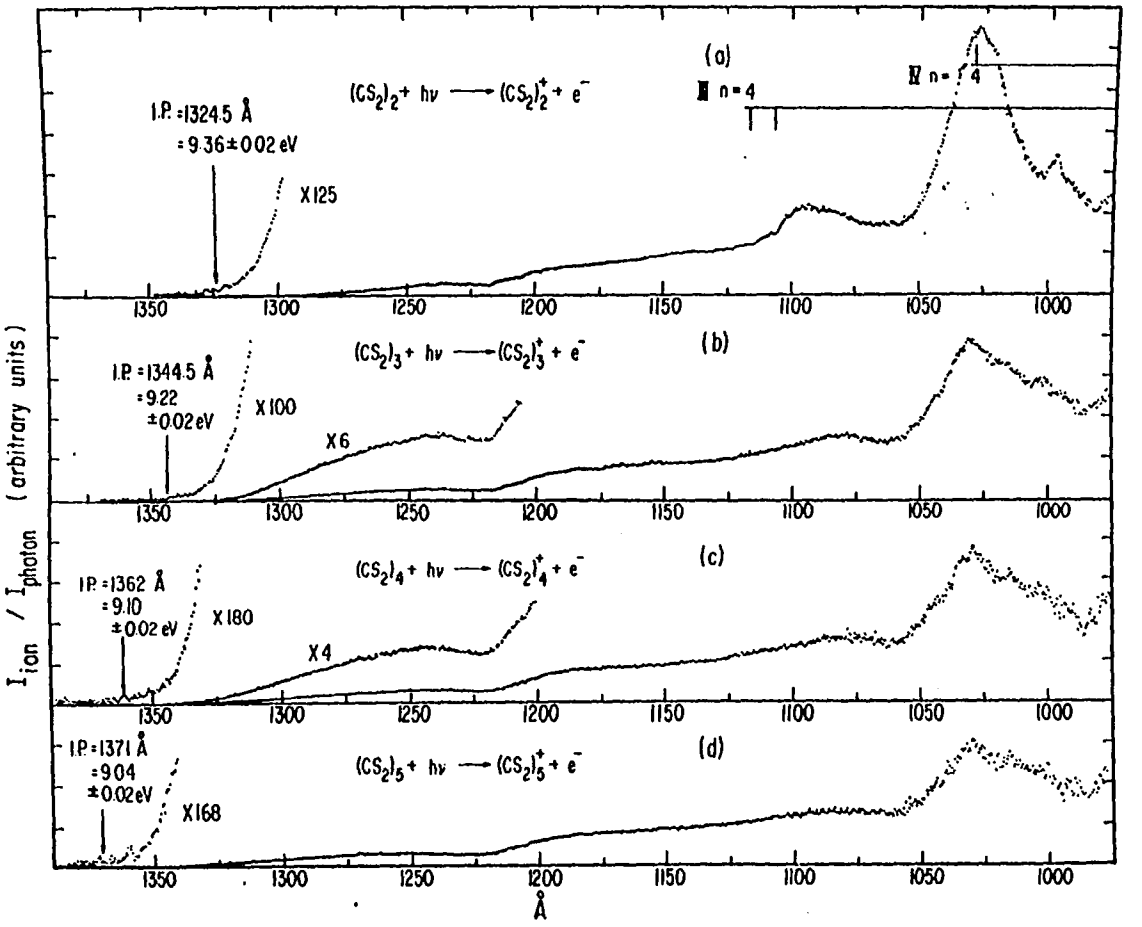

Figure 3. PIE curve in the region 970-1350 Å for (a) $(CS_2)_2^+$, (b) $(CS_2)_3^+$, (c) $(CS_2)_4^+$, and (d) $(CS_2)_5^+$

by Meot-Ner and Field (15) to be 21.9 ± 2.5 kcal/mol. In order to compare these two values, they must be converted to the same temperature (30). ΔH°_{f620} is related to ΔH_{fo} by the relation

$$\Delta H^\circ_{fo} = \Delta H^\circ_{f620} - \int_0^{620} [Cp((CS_2)_2^+) - Cp(CS_2) - Cp(CS_2^+)]dT$$

where $Cp((CS_2)_2^+)$, $Cp(CS_2)$ and $Cp(CS_2^+)$ are the heat capacities at constant pressure of $(CS_2)_2^+$, CS_2 and CS_2^+, respectively. Assuming an ideal gas model and excluding any vibrational and electronic contributions to Cp, a value of 18.2 ± 2.5 kcal/mol (31) can be derived for ΔH°_{fo} from the value for ΔH°_{f620}. Taking into account the uncertainty of these measurements, this value is within the limits of error of the binding energy deduced for $(CS_2)_2^+$ in the present photoionization study.

The PIE curves for $(CS_2)_3^+$, $(CS_2)_4^+$ and $(CS_2)_5^+$ in the region of 970-1400 Å are shown in Fig. 3(b), (c) and (d), respectively. These curves have been arbitrarily normalized to the PIE for $(CS_2)_2^+$ at 1150 Å. The IE's for $(CS_2)_3$, $(CS_2)_4$ and $(CS_2)_5$ are found to be 9.22 ± 0.02 eV, 9.10 ± 0.02 eV and 9.04 ± 0.02 eV, respectively. The uncertainties of these values are taken to be more than or equal to the largest difference of the results of two to three scans. By assuming the binding energy of $(CS_2)_n$, n = 2-4, with CS_2 to be the same as $(CS_2)_2$, the solvation energies of a carbon disulfide ion by two, three and four carbon disulfide molecules can be calculated via the cycles shown in Fig. 4.

Recently, in a molecular beam photoionization study of acetone clusters (10), Trott et al. found that the measured IE's for $(CH_3COCH_3)_n$,

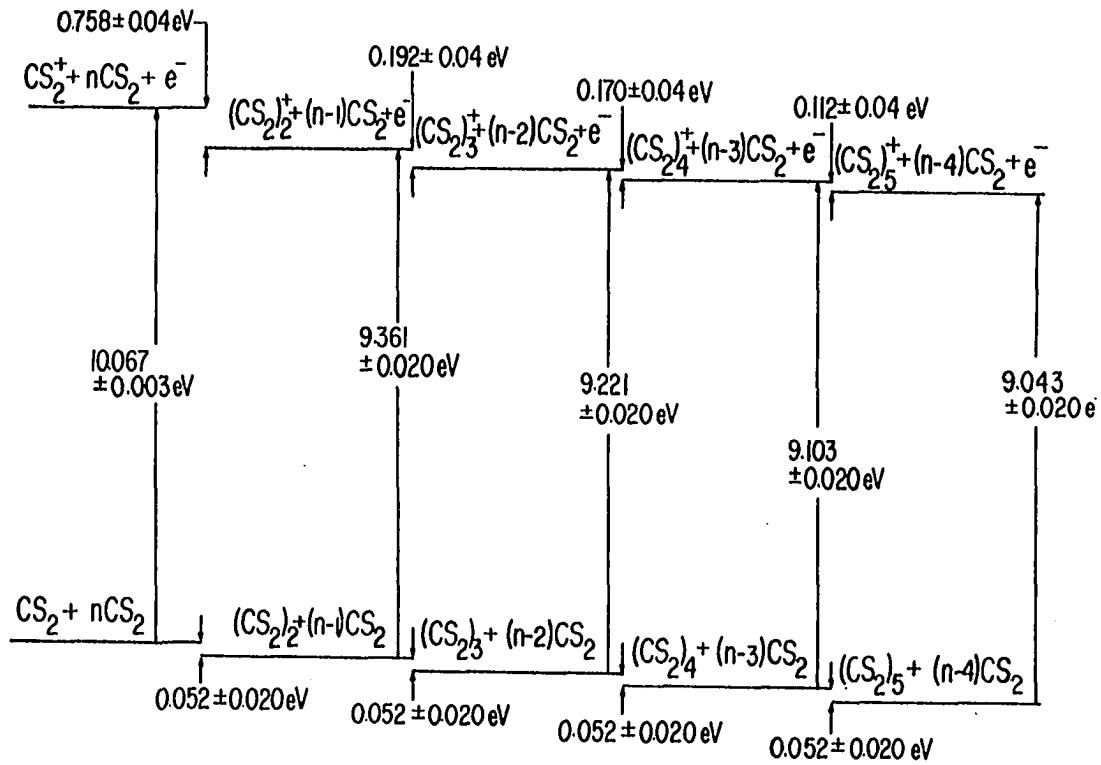

Figure 4. Energetics of $(CS_2)_n^+$, n = 1-5, system

n = 1-4, fall squarely on a straight line when plotted as a function of 1/n, and this functional dependence is consistent with the prediction of a simple independent-systems model for the cluster ion system (32). A plot of the measured IEs for $(CS_2)_n$, n = 1-5, as a function of 1/n is shown in Fig. 5. Except for a small deviation of the IE for $(CS_2)_2$, the correlation of the IEs with cluster size is consistent with the prediction of this simple model. If the IEs for $(CS_2)_n$, n > 5, continue to decrease linearly as a function of 1/n, a value of approximately 8.77 eV is predicted for the bulk IE of carbon disulfide. The surprisingly good agreement between the prediction of this simple independent-systems model and experimental results certainly warrants future investigations.

The general profiles of the PIE curves for $(CS_2)_n^+$, n = 2-5, are very similar. Consistent with the previous observation (14), the autoionization structure in the PIE curve for $(CS_2)_2^+$ which corresponds to a member of Rydberg series III, n = 4, at approximately 1116 Å is found to be broadened and appears to be blue-shifted whereas the position of the resonance which correlates to Rydberg series IV, n = 4, at 1035 Å remains relatively unchanged. As a consequence of the higher signal-to-noise level achieved in this experiment, the peak height of the autoionization feature at 1035 Å in the PIE curve for $(CS_2)_2^+$ can be seen to be reduced almost by half if the dimer spectrum is normalized to the monomer spectrum at a structureless region such as 1150 Å. The broadening of the autoionization structure can be attributed partly to perturbation of the Rydberg orbitals when a dimer is formed. Using the measured effective quantum number (n^*), 2.009, for series III (n = 4),

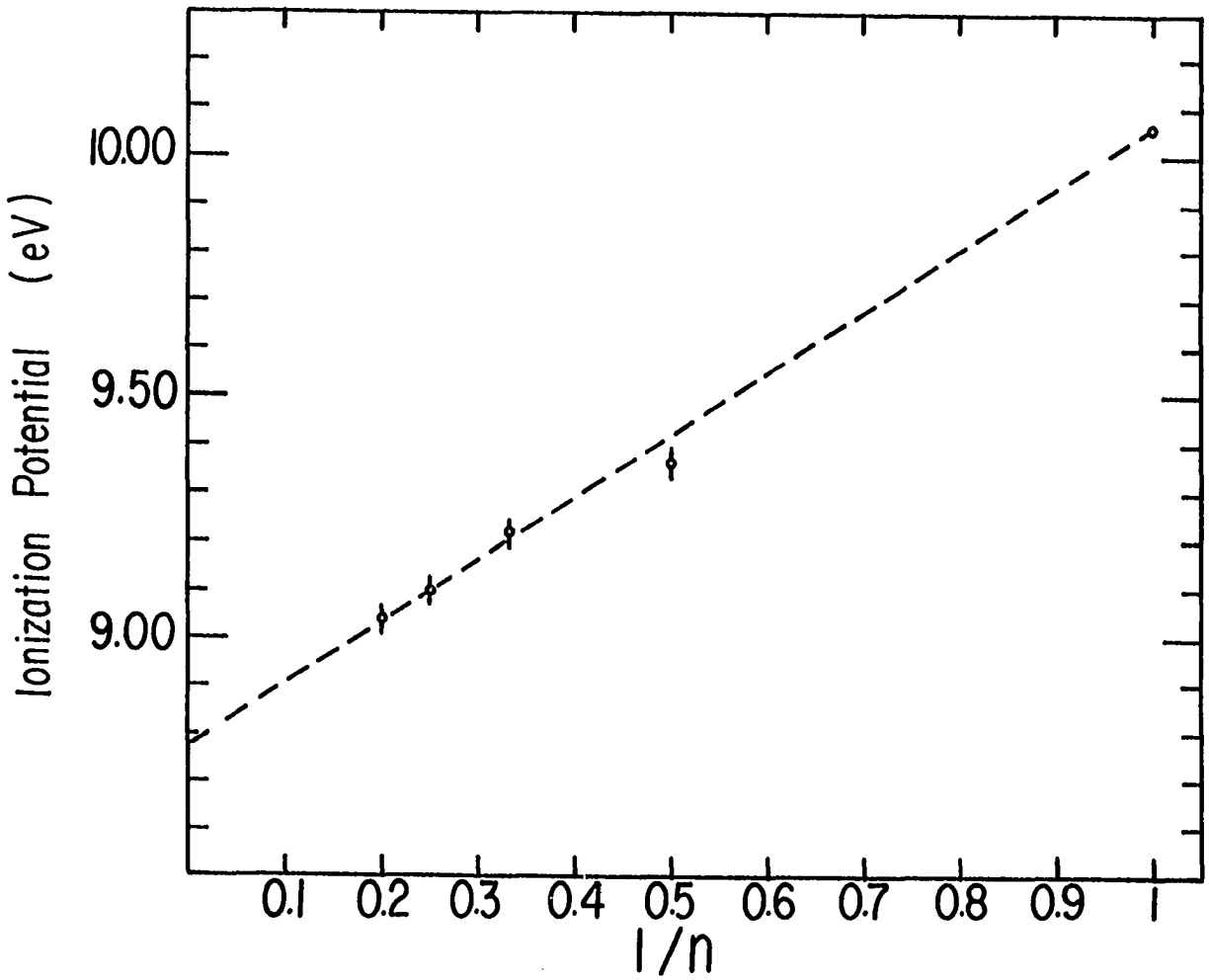

Figure 5. Plot of the IE of $(CS_2)_n$ vs. 1/n

and 2.312 for series IV (n = 4) (33), the Rydberg orbitals responsible for the autoionization features at 1116 and 1035 Å have Bohr radii of 2.14 Å and 2.83 Å, respectively. By comparison, the C-S bond distance in CS_2 is 1.554 Å (34). Although the structure of the $(CS_2)_2$ dimer is unknown, the equilibrium separation between CS_2 and CS_2 can be estimated from the crystal structure of solid CS_2 (34) to be approximately 3.5 to 4.0 Å. Hence, while these two orbitals are large enough when compared with the size of the CS_2 monomer to have hydrogenic characteristics, they are not large enough to remain unperturbed when a dimer is formed. Actually, these low lying Rydberg states may mix strongly with the valence states of the same symmetry and participate in the bonding of a dimeric ion. Another reason for the reduction in peak heights of the autoionization resonances observed in the PIE curve for $(CS_2)_2^+$ is due to the dissociation of the dimeric ions resulting from autoionization. In this spectral region, autoionization can only lead to the ground electronic state, $\tilde{X}^2\Pi_g$, and the resultant dimeric ions, $CS_2^+(\tilde{X}^2\Pi_g, v') \cdot CS_2(X^1\Sigma_g^+)$ (35), probably consists of a distribution of vibrational states. Since these Rydberg levels are more than 1 eV above the onset of the $\tilde{X}^2\Pi_g$ state which is greater than the binding energy for $(CS_2)_2^+$, it is likely that a fraction of the dimeric ions derived from autoionization will have enough energy to dissociate $(CS_2)_2^+$ into $CS_2^+ + CS_2$. If this dissociation process takes place in less than the flight time from the ionization region to the detector, they will not be detected. The binding energies for higher clusters, $\sim$0.1-0.2 eV, which are substantially smaller than that of $(CS_2)_2^+$ implies that $(CS_2)_n^+$, n > 2, will be

more susceptible to dissociation. The observed gradual smoothing of the autoionization structure as the size of cluster increases (Fig. 3) is consistent with this argument.

A similar trend is also evident for higher members of these Rydberg series. Figure 6(b) and (c) show the PIE curves for $(CS_2)_2^+$ and $(CS_2)_3^+$ in the wavelength region from 600 to 1050 Å. The PIE curve for CS_2^+ obtained with the same optical resolution is also depicted in Fig. 6(a) for comparison. The autoionization resonances which correlate with Rydberg series III and IV that converge to the $\tilde{B}^2\Sigma_u^+$ state of CS_2^+ are found to be greatly suppressed in the PIE curve for $(CS_2)_2^+$, and this structure is almost completely absent in the PIE curve for $(CS_2)_3^+$. The positions of the autoionization peaks resolved in the dimer curve are listed in Table 3 and compared with those of the corresponding members of series III and IV observed in absorption spectra with comparable resolution (36). The autoionization structure correlating with Rydberg series V which converges to the $\tilde{C}^2\Sigma_g^+$ state of CS_2^+ is hardly discernible in the PIE curves for $(CS_2)_2^+$ and $(CS_2)_3^+$. In this wavelength region, the $CS_2^+ \cdot CS_2$ or $CS_2^*(n) \cdot CS_2$ formed will have enough internal energy to cause fragmentation to take place. Resonances correlating to Rydberg series V were found in the PIE curves for CS_3^+, S_2^+ and $C_2S_3^+$ (37).

As expected, the positions of the Rydberg series observed in the PIE curve for $(CS_2)_2^+$ are red-shifted in energy when compared with the positions of the corresponding series in the monomer spectrum. Similar phenomena have been observed previously in the photoionization studies of rare gas dimers. However, the most interesting result is that the

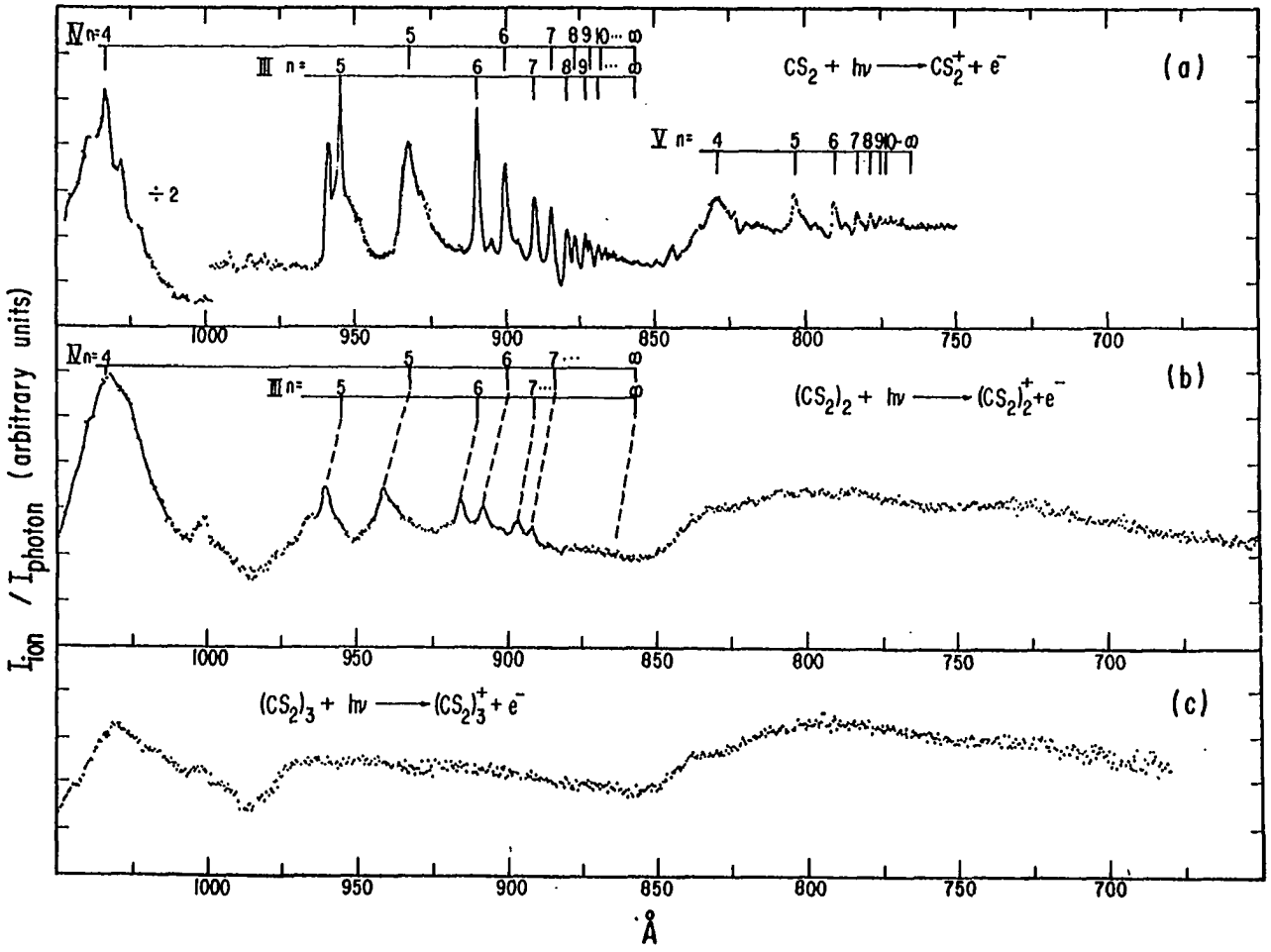

Figure 6. Photoionization efficiency curves for (a) CS_2^+, (b) $(CS_2)_2^+$ and (c) $(CS_2)_3^+$ in the region ~600-1050 Å

Table 3. Potential energy of CS_2^*(III or IV, n)-CS_2 at the equilibrium nuclear configuration of $(CS_2)_2$

CS_2 Rydberg Series[a] (eV)		n^*[b]	Bohr Radius (Å)	$E_1^*(n)$[c] (eV)	$E_2^*(n)$[d] (eV)	$\Delta E(n)$[e] (eV)	$D^*(n)$[f] (eV)
III(nsσ)							
n = 5	12.983 (955 Å)	3.025	4.8	12.983 (955 Å)	12.908 (960.5 Å)	0.074	0.124
6	13.632 (909.5 Å)	4.037	8.3	13.640 (909 Å)	13.365 (914 Å)	0.075	0.125
7	13.939 (889.5 Å)	5.056	13.5	13.939 (889.5 Å)	13.814 (897.5 Å)	0.125	0.175
IV(npπ)							
n = 5	13.303 (932 Å)	3.386	6.1	13.303 (932 Å)	13.155 (942.5 Å)	0.148	0.198
6	13.776 (900 Å)	4.405	10.3	13.776 (900 Å)	13.640 (909 Å)	0.136	0.186
7	14.010 (885 Å)	5.402	15.5	14.018 (884.5 Å)	13.876 (893.5 Å)	0.142	0.192
Series limit					Series limit		
	14.464 (857.2 Å)	--	--	$E_1^*(n\to\infty)$ = 14.464	$E_2^*(n\to\infty)$ = 14.309 (866.5 Å)	0.155	$D^*(n\to\infty)$ = 0.205

[a]Ref. 36.

[b]Ref. 33.

[c]Autoionization peak observed in the PIE curve for CS_2^+.

[d]This value is interpreted as the energy difference between the potential energy curve of $(CS_2)_2$ and $CS_2^*(n) \cdot CS_2$ at the equilibrium geometry of $(CS_2)_2$.

[e]$\Delta E(n) = E_1^*(n) - E_2^*(n)$.

[f]The potential energy of CS_2^*(III or IV, n) $\cdot CS_2$ at the equilibrium nuclear configuration of $(CS_2)_2$.

shifts, $\Delta E(n)$, of the Rydberg series IV are nearly a factor of two greater than those of Rydberg series III. Although the binding energy, ($\sim$0.8 eV), of CS_2^+ is relatively weak, it is still much stronger than the van der Waals bond ($\sim$0.05 eV) between CS_2 and CS_2. Thus, the equilibrium bond distance between CS_2^+ and CS_2 in $(CS_2)_2^+$ is expected to be substantially shorter than that in $(CS_2)_2$. It is important to emphasize that the Bohr radii of all Rydberg orbitals of Rydberg series III ($n > 4$) and IV ($n > 4$) are greater than 4.8 Å (Table 3). Since these values are appreciably larger than or at least comparable to the size of $(CS_2)_2$, an electron excited to one of these Rydberg levels will only play a very minor role and give rise to only a minor perturbation in the bonding of an excited dimer, $CS_2^*(n) \cdot CS_2$. Higher members of the Rydberg levels, $CS_2^*(n>4) \cdot CS_2$, which converge to the ionic state of $(CS_2)_2^+$ will have a potential energy curve resembling that of $(CS_2)_2^+$, however, the existence of an electron in a particular Rydberg orbital, n, mainly introduces the Pauli exclusion force and weakens the bonding of the ion core, $(CS_2)_2^+$, hence the depth of the well in the Rydberg potential curve for $CS_2^*(n) \cdot (CS_2)$ should be shallower than that of $(CS_2)_2^+$. A schematic representation showing the relationship of these potential curves is given in Fig. 7, where $E_1^*(n)$ and $E_2^*(n)$ represent the excitation energies from CS_2 to $CS_2^*(n)$ and from $(CS_2)_2$ to $CS_2^*(n) \cdot CS_2$, respectively. Since photoexcitation is a vertical process, and the transition takes place primarily at the potential energy well of $(CS_2)_2$, $E_2^*(n)$ which is measured by the peak position of the autoionization resonance in the PIE curve can be taken to be the difference in energy between the potential energy

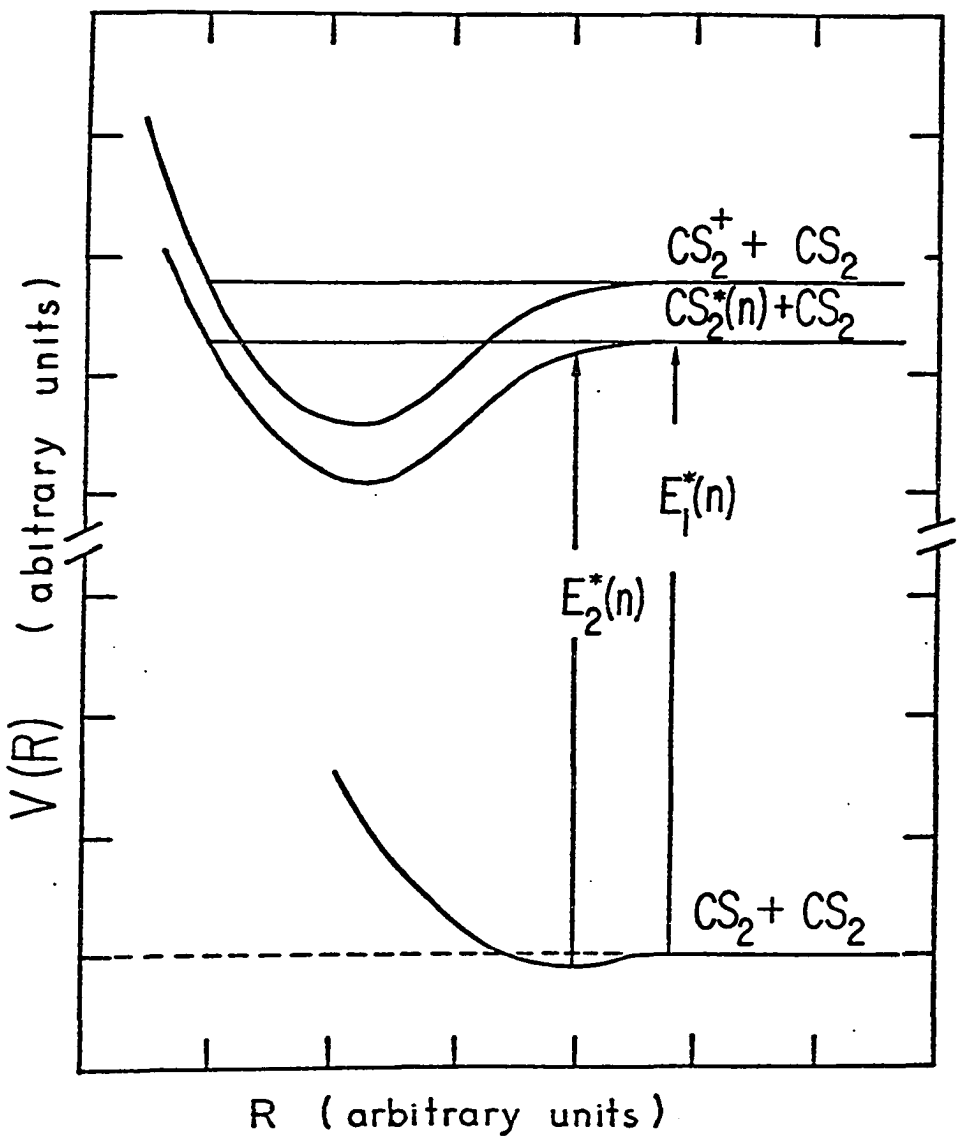

Figure 7. Schematic diagram illustrating the relationship of the potential curves of $(CS_2)_2$, $CS_2^*(n) \cdot CS_2$ and $(CS_2)_2^+$. R and V(R) represent the separation between two CS_2 molecules and potential energy, respectively

curve of $(CS_2)_2$ and that of $CS_2^*(n) \cdot CS_2$ at the equilibrium nuclear configuration of $(CS_2)_2$. Knowing $E_1^*(n)$ and $E_2^*(n)$ from the PIE curves for CS_2^+ and $(CS_2)_2^+$, along with the known dissociation energy, 0.05 eV, for $(CS_2)_2$, makes it possible to deduce the potential energy of $CS_2^*(n) \cdot CS_2$, $D^*(n)$, at the equilibrium nuclear configuration of the neutral dimer through the relationship

$$D^*(n) = E_1^*(n) - E_2^*(n) + 0.05 \text{ eV} \quad .$$

The calculated values for $D^*(n)$ are listed in Table 3. The series limit $E_2^*(n\to\infty)$, for series III and IV of $(CS_2)_2$ is determined to have the value, 14.309 eV (37). From this, the potential energy for $(CS_2)_2^+$ at the equilibrium nuclear configuration of $(CS_2)_2$, $D^*(n\to\infty)$, is deduced to be 0.205 eV.

The nature of Rydberg series III and IV for CS_2 has been investigated by Ogawa and Chang (33). They suggested that series III is an nsσ-type series while series IV consists of ndσ-type transitions. However, more recently, a re-examination of the quantum defects of these series by Larzilliere and Damany (18) leads to the conclusion that series IV is an npπ series. These authors identify series III to be an nsσ series. Thus, the label of series III and IV in this report follows the assignments of Larzilliere and Damany (18). As indicated in Table 3, $D^*(n)$, $n = 5$, 6 and 7, for Rydberg series III is appreciably smaller than $D^*(n\to\infty)$ whereas $D^*(n)$, $n = 5$, 6 and 7, deduced for Rydberg series IV is very close to $D^*(n\to\infty)$. This difference implies that the perturbation introduced by an electron in an nsσ orbital to the bonding of the ion

core, $(CS_2)_2^+$, is more substantial than that induced by an electron in an npπ orbital. Since one expects an appreciable perturbation of an nsσ orbital for any dimer geometry and a linear or near linear geometry for CS_2 is the most favorable configuration for minimization of the perturbation of an electron in an npπ orbital, from a symmetry point of view, the CS_2 dimer is expected to have a near linear configuration.

In order to explore further the validity of the above argument, a photoionization study was made of $Ar \cdot CS_2$ in the wavelength region 800-960 Å. The PIE curve for $(ArCS_2)^+$ obtained with a photon bandwidth of 1.4 Å (FWHM) is shown in Fig. 8. It is interesting to note that the Rydberg feature in the PIE curve for $(ArCS_2)^+$ is much sharper than that in the $(CS_2)_2^+$ spectrum. The autoionization resonances observed in the PIE curve for $(ArCS_2)^+$ are listed in Table 4 where they can be compared with the corresponding Rydberg series III and IV of CS_2.

Since Ar and CS_2 are held together mainly by long range van der Waals forces, and the size of Ar (38) (covalent radius ∿1.74 Å) is comparable to the equilbrium distance between the two sulfur atoms in CS_2, the most stable geometry for $ArCS_2$ should be for Ar to be close to the center of CS_2 such that both sulfur atoms are in the proximity of Ar. Therefore, according to this symmetry picture, we expect to find similar shifts in energy for both series III and IV in the PIE curve for $(ArCS_2)^+$ as compared to that in the CS_2^+ spectrum. Within the uncertainties of this experiment, the shifts in energy, $\Delta E(n)$, observed in the $(ArCS_2)^+$ spectrum as indicated in Table 4 are nearly the same for Rydberg series

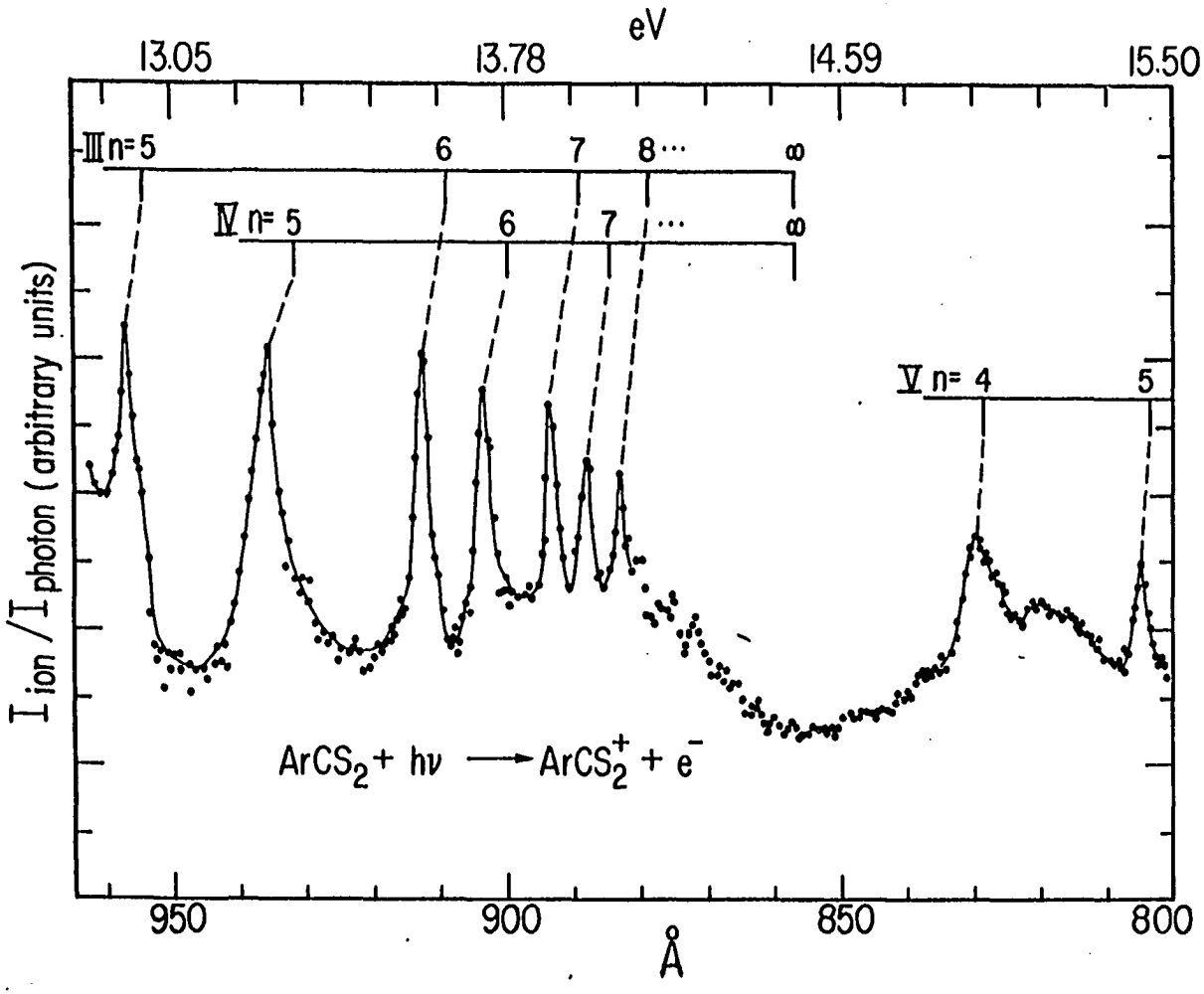

Figure 8. PIE curve for $(ArCS_2)^+$ in the region 800-965 Å

Table 4. Rydberg series of Ar-CS_2

CS_2 Rydberg Series $E_1^*(n)$[a] (eV)		Rydberg Series $E_2^*(n)$[b] (eV)	$\Delta E(n)$[c] (eV)
III(nsσ)			
n = 5	12.983 (955 Å)	12.949 (957.5 Å)	0.044
6	13.640 (909 Å)	13.580 (913 Å)	0.060
7	13.939 (889.5 Å)	13.876 (893.5 Å)	0.063
IV(npπ)			
n = 5	13.303 (932 Å)	13.253 (935.5 Å)	0.050
6	13.776 (900 Å)	13.723 (903.5 Å)	0.053
7	14.018 (884.5 Å)	13.962 (888 Å)	0.056

[a]Autoionization peak observed in the PIE curve for CS_2^+.

[b]This value is interpreted as the energy difference between the potential energy curve of $ArCS_2$ and Ar-CS_2 equilibrium nuclear configuration of $ArCS_2$.

[c]$\Delta E(n) = E_1^*(n) - E_2^*(n)$.

III and IV, supporting the symmetry argument for a near linear configuration for $(CS_2)_2^+$.

REFERENCES

1. G. R. Parr and J. W. Taylor, Rev. Sci. Instrum. 44, 1578 (1973).

2. G. R. Parr and J. W. Taylor, Int. J. Mass Spectrom. Ion Phys. 14, 467 (1974).

3. C. Y. Ng, B. H. Mahan and Y. T. Lee, J. Chem. Phys. 65, 1956 (1976).

4. C. Y. Ng, D. J. Trevor, B. H. Mahan and Y. T. Lee, J. Chem. Phys. 65, 4327 (1976).

5. C. Y. Ng, D. J. Trevor, B. H. Mahan and Y. T. Lee, J. Chem. Phys. 66, 446 (1977).

6. C. Y. Ng, P. W. Tiedemann, B. H. Mahan and Y. T. Lee, J. Chem. Phys. 66, 3985 (1977).

7. C. Y. Ng, P. W. Tiedemann, B. H. Mahan and Y. T. Lee, J. Chem. Phys. 66, 5737 (1977).

8. C. Y. Ng, D. J. Trevor, P. W. Tiedemann, S. T. Ceyer, P. L. Kronebush, B. H. Mahan and Y. T. Lee, J. Chem. Phys. 67, 4235 (1977).

9. G. G. Jones and J. W. Taylor, J. Chem. Phys. 68, 1768 (1978).

10. W. M. Trott, N. C. Blais and E. A. Walters, J. Chem. Phys. 69, 3150 (1978).

11. S. T. Ceyer, P. W. Tiedemann, B. H. Mahan and Y. T. Lee, J. Chem. Phys. 70, 14 (1979).

12. S. T. Ceyer, P. W. Tiedemann, C. Y. Ng, B. H. Mahan and Y. T. Lee, J. Chem. Phys. 70, 2138 (1979).

13. P. W. Tiedemann, S. L. Anderson, S. T. Ceyer, T. Hirooka, C. Y. Ng, B. H. Mahan and Y. T. Lee, J. Chem. Phys. 71, 605 (1979).

14. W. M. Trott, N. C. Blais and E. A. Walters, J. Chem. Phys. 71, 1692 (1979).

15. M. Meot-Ner (Mautner) and F. H. Field, J. Chem. Phys. 66, 4527 (1977).

16. W. C. Price and D. M. Simpson, Proc. R. Soc. London Ser. A 165, 272 (1938).

17. Y. Tanaka, A. S. Jursa and F. J. LeBlanc, J. Chem. Phys. 32, 1205 (1960).

18. M. Larzilliere and N. Damany, Can. J. Phys. 56, 1150 (1978).

19. F. R. Greening and G. W. King, J. Mol. Spectrosc. 59, 312 (1976).

20. J. H. D. Eland and C. J. Danby, Int. J. Mass Spectrom. Ion Phys. 1, 111 (1968).

21. M. J. Schirmer, W. Domeke, L. S. Cedarbaum, W. von Niessen and L. Asbrink, Chem. Phys. Lett. 61, 30 (1979).

22. C. R. Brundle and D. W. Turner, Int. J. Mass Spectrom. Ion Phys. 2, 195 (1969).

23. V. H. Dibeler and J. A. Walker, J. Opt. Soc. Am. 57, 1007 (1967).

24. R. Frey, B. Gotchov, W. B. Peatman, H. Pollak and E. W. Schlag, Int. J. Mass Spectrom. Ion Phys. 26, 137 (1978).

25. V. E. Bondybey, J. H. English and T. A. Miller, J. Chem. Phys. 70, 1621 (1979).

26. J. Wayne Rabalais, Principles of Ultraviolet Photoelectron Spectroscopy (Wiley, New York, 1977).

27. P. Coppens, J. C. Raynaert and J. Drowart, J. Chem. Soc. Faraday Trans. 2 75, 292 (1979).

28. G. Herzberg, Molecular Spectra and Molecular Structure III Electronic Spectra and Electronic Structure of Polyatomic Molecules (Van Nostrand, Princeton, 1966), p. 600.

29. J. O. Hirschfelder, C. F. Curtiss and R. B. Bird, Molecular Theory of Gases and Liquids (Wiley, New York, 1964), p. 1112.

30. Ref. 14 took the value, ΔH°_{f620}, determined by Meot-Ner and Field and compared it directly with the binding energy deduced in the molecular beam photoionization experiment.

31. This assumption probably underestimates the contribution from the low frequency vibrational modes of $(CS_2)_2^+$.

32. W. T. Simpson, Theories of Electrons in Molecules (Prentice Hall, Englewoods Cliffs, NJ, 1962), Chapter 4.

33. M. Ogawa and H. C. Chang, Can. J. Phys. 48, 2455 (1970).

34. N. C. Baenziger and W. L. Daux, J. Chem. Phys. 48, 2974 (1968).

35. To a first approximation, a dimeric ion derived from autoionization can be considered to be composed of one CS_2^+ molecular ion at a given internal excitation resulting from autoionization and a CS_2 molecule in the $X^1\Sigma g^+$ state.

36. G. R. Cook and M. Ogawa, J. Chem. Phys. 51, 2419 (1969).

37. See Section 3.

38. Kr or Xe may seem to be a better choice due to its larger size in comparison with Ar. However, these atoms have many atomic transitions which lie in this energy region which may obscure the identification of the Rydberg series III and IV of CS_2 in the PIE curve for $(ArCS_2)^+$.

SECTION III.

A STUDY OF THE HIGH RYDBERG STATE AND ION-MOLECULE REACTIONS OF CARBON DISULFIDE USING THE MOLECULAR BEAM PHOTOIONIZATION METHOD

INTRODUCTION

The behavior of atoms and molecules in excited Rydberg states has been the subject of numerous experimental and theoretical investigations in recent years (1,2). By far the greatest experimental effort has been in the area of inelastic collisions between Rydberg atoms and other atoms and molecules. The chemistry of this class of atoms and molecules with the exception of metastable species is still relatively unexplored. One of the difficulties encountered in a collisional experiment involving Rydberg atoms or molecules, besides the preparation of these species, is their short radiative lifetimes. For example, consider a cross beam experiment in which the Rydberg atoms or molecules are prepared in a specific Rydberg state with one hundred percent purity at approximately 1 cm before the collision region. For a molecular beam at thermal velocity, it will take $\gtrsim 10^{-5}$ s to travel 1 cm. In order to preserve the purity and maintain sufficient intensity of the Rydberg atoms or molecules for a scattering experiment, the decay times of these Rydberg atoms or molecules must be $>10^{-6}$ s. This limits the quantitative studies of atoms and molecules to metastable or highly excited long-lived Rydberg states usually with principal quantum numbers $n > 10$. One method which overcomes this difficulty and allows a systematic measurement of the relative cross sections of a specific product channel as a function of Rydberg level (n,ℓ) is the molecular beam photoionization of van der Waals dimers. Since the equilibrium bond distance between the two moieties of a complex in a highly excited Rydberg state (or a dimeric ion) is substantially shorter than that in

the neutral van der Waals dimer, the complex in a highly excited Rydberg state (or the dimeric ion) formed by the absorption of a vacuum ultraviolet photon is expected to be close to the asymptotic region of the potential energy curve for the excited complex (or the dimeric ion). Thus, to a first approximation, the photoionization or photoexcitation of a van der Waals molecule can be viewed as ionization or excitation of only one moiety making up the dimer. Furthermore, the internal energy induced fragmentation of the excited complex (or the dimeric ion) can also be regarded as high Rydberg (or ion-molecule) reactions proceeding at zero kinetic energy.

Although the relative reaction probabilities for the formation of various product channels determined from these types of experiments are expected to be different from those measured in real collisional processes, this type of measurement will still be able to provide insight into the reaction mechanisms of this class of atoms and molecules. A study of the following Rydberg state reactions of carbon disulfide has been performed.

$$CS_2^*(V,n) \cdots CS_2 \rightarrow CS_3^+ + CS + e^- \quad (1)$$

$$\rightarrow S_2^+ + 2CS + e^- \quad (2)$$

$$\rightarrow C_2S_3^+ + S + e^- \quad (3)$$

$$\rightarrow CS_4^+ + C + e^- \quad (4)$$

$$\rightarrow (CS_2)_2^+ + e^- \quad (5)$$

In addition to the study of these Rydberg state reactions, the internal energy effects and the energetics of the following ion-molecule reactions of carbon disulfide has also been examined by this method.

$$CS_2^+(\tilde{A}^2\Pi_u,\ \tilde{B}^2\Sigma_u^+ \text{ or } \tilde{C}^2\Sigma_g^+) \cdots CS_2 \rightarrow CS_3^+ + CS \quad (6)$$

$$\rightarrow S_2^+ + 2CS \quad (7)$$

$$\rightarrow C_2S_3^+ + S \quad (8)$$

$$\rightarrow CS_4^+ + C \quad (9)$$

Since the lifetimes of the $\tilde{A}^2\Pi_u$ and $\tilde{B}^2\Sigma_u^+$ states are $\sim$2.5 μs and $\sim$300 ns (3,4), respectively, the lifetime consideration for a scattering experiment is also valid for the $\tilde{A}^2\Pi_u$ and $\tilde{B}^2\Sigma_u^+$ states of CS_2^+.

EXPERIMENTAL

The CS_2 molecular beam was produced by seeding CS_2 vapor ($\sim$270 Torr) at $\sim$18°C in 450 Torr of argon, then expanding the mixture through a 70 μm diameter nozzle orifice. Mallinckrodt analytical grade CS_2 was used without further purification. The argon was obtained from Matheson ($\gtrsim$99.995% purity).

The PIE curves obtained for CS_3^+ (735-950 Å), S_2^+ (650-880 Å), $C_2S_3^+$ (800-885 Å), CS^+ (680-810 Å), and $(CS_2)_2^+$ (680-1050 Å) using the helium Hopfield continuum light source with a wavelength resolution of 1.4 Å (FWHM) are shown in Figs. 1, 2, 3(a), 4 and 6(b), respectively. The PIE curves for CS_2^+ obtained with the same optical resolution are also plotted in Figs. 1, 2 and 6(a) for comparison with the structure observed in the PIE curves for CS_3^+, S_2^+ and $(CS_2)_2^+$. Data points are plotted at intervals of 0.5 Å. Figures 3(b) and 5 depict the PIE curves for $C_2S_3^+$ (715-880 Å) and CS_4^+ (700-820 Å), respectively, and due to low signal levels, data points were obtained at wavelength intervals of 1 Å. Each of the spectra was scanned at least twice and the prominent structures were found to be reproducible.

RESULTS AND DISCUSSION

The PIE curve for CS_3^+ resulting from the fragmentation of $(CS_2)_2^+$ is shown along with a portion of the CS_2^+ PIE curve in Fig. 1. The PIE curve for CS_3^+ increases gradually above the threshold until a step-like structure is observed at 14.3 eV (866.5 Å). A similar structure at the same energy is evident in the S_2^+ spectrum (Fig. 2). In a gas cell photoionization study of the ion-molecule reaction $CS_2^+ + CS_2$, Eland and Berkowitz (5) observed a clear step at 14.464 eV (857.2 Å) which is the energy of the $\tilde{B}^2\Sigma_u^+$ state of CS_2^+. Below the step, they found the ratio of the signal of S_2^+ to that of CS_2^+ to be much smaller than above it, showing that S_2^+ is formed more readily when CS_2^+ is in the $\tilde{B}^2\Sigma^+$ state in comparison to the $\tilde{A}^2\Pi_u$ state. Taking into account the lifetime of the $\tilde{B}^2\Sigma_u^+$ and $\tilde{A}^2\Pi_u$ states, they estimated the cross sections for the reaction ascribed to $CS_2^+(\tilde{B}^2\Sigma_2^+)$ and $CS_2^+(\tilde{A}^2\Pi_u)$ to be 1.8×10^{-14} cm^2 and 7×10^{-17} cm^2, respectively. The difference in energy of the step observed in the PIE data for CS_3^+ and S_2^+ at 866.5 Å and the step found at 857.2 Å in Ref. 5 is 0.155 eV. Since this value is very close to the shifts in energy observed for the higher members of Rydberg series III and IV in the PIE curve for $(CS_2)_2^+$ relative to the corresponding resonances resolved in the CS_2^+ spectrum, the step at 866.5 Å is assigned as the converging limit for Rydberg series III and IV in $(CS_2)_2$. The red-shift in energy of the series limit in the dimer as compared to that of the monomer simply indicates that the potential energy of $CS_2^+ \cdot CS_2$ at the equilibrium nuclear configuration of $(CS_2)_2$ is larger than the well depth of the neutral carbon disulfide dimer. Using the binding energy

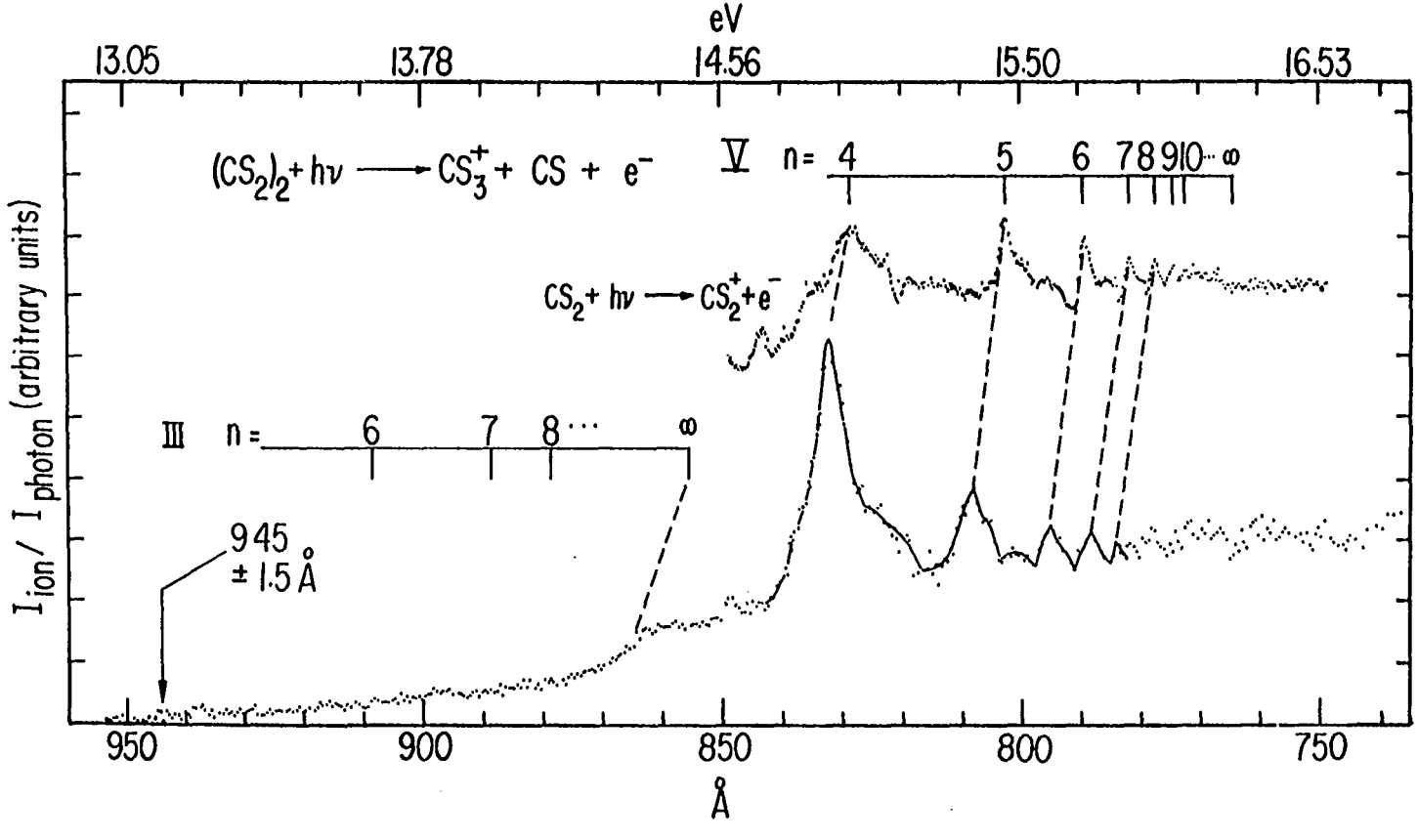

Figure 1. PIE curve for CS_3^+ in the region 735-950 Å

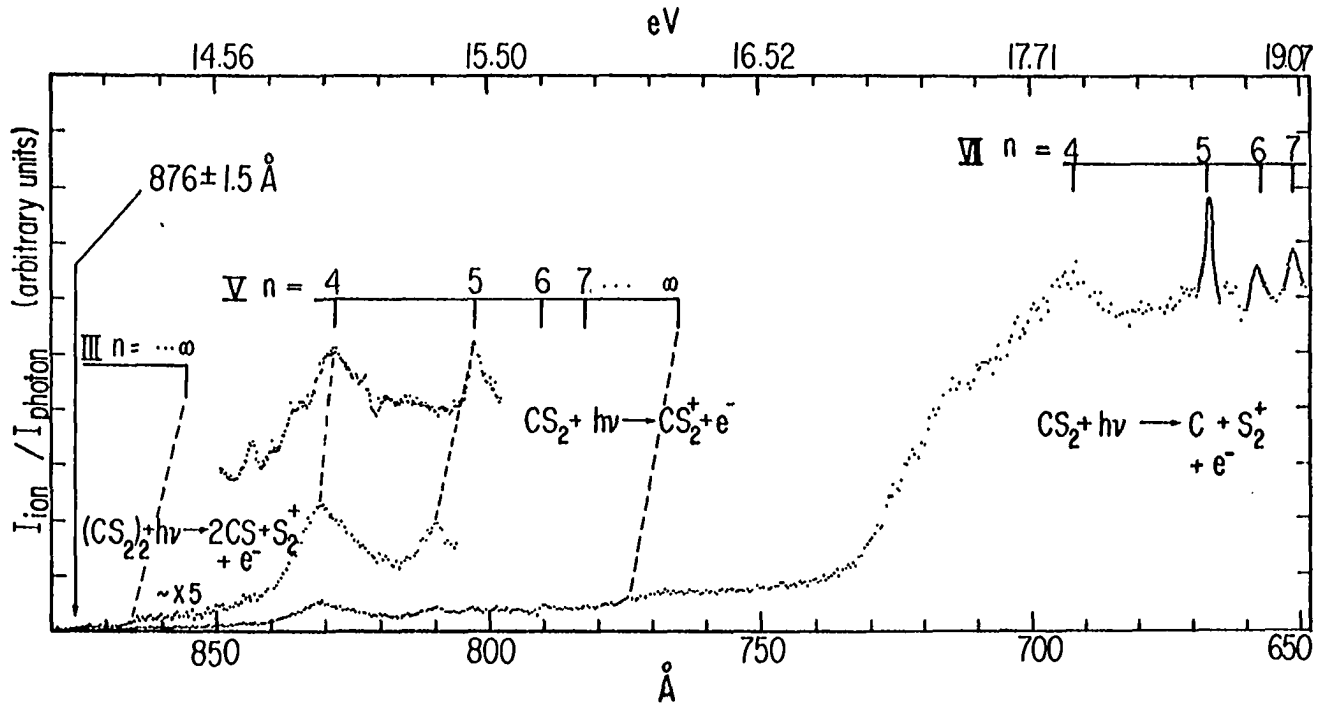

Figure 2. PIE curve for S_2^+ in the region 650-880 Å

(0.052 eV) of $(CS_2)_2$ derived by using second virial coefficients (6,7), along with the series limits of Rydberg series III and IV for CS_2 (8) and $(CS_2)_2$, the potential energy, $D(\tilde{B}^2\Sigma_u^+)$, for $CS_2^+(\tilde{B}^2\Sigma_u^+) \cdot CS_2$ at the equilibrium nuclear geometry of $(CS_2)_2^+$ is deduced to be 0.205 eV.

Since the S_2^+ ions formed in the gas-cell photoionization experiment are promoted by internal energy as well as kinetic energy in secondary collisional processes, Eland and Berkowitz were not able to locate the appearance energy for S_2^+ formation in the previous experiment. This is not a problem here. The shifts of Rydberg series III, IV and V and their converging limits of $(CS_2)_2$ as compared to those of CS_2 unambiguously indicates that CS_3^+ and S_2^+ are formed predominately by the fragmentation of $(CS_2)_2$ and the contributions from secondary collisional processes are negligible in this experiment. The appearance energy for S_2^+ is determined to be 14.15 ± 0.02 eV (876 ± 1.5 Å). Within the uncertainties of this experiment, this value is found to be equal to the thermochemical threshold for the reaction, $CS_2^+(\tilde{X}^2\Pi_g) + CS_2 \rightarrow S_2^+ + 2CS$. In other words, the activation energy for this reaction is zero. Furthermore, the substantial increase in the yields of CS_3^+ and S_2^+ above the $\tilde{B}^2\Sigma_u^+$ state also indicates that the cross sections for the ion-molecule reactions 6 and 7 with CS_2^+ in the $\tilde{B}^2\Sigma_u^+$ state are much higher than those of the corresponding reactions with CS_2^+ in the $\tilde{A}^2\Pi_u$ state, an observation in agreement with the conclusions of a previous experiment (5).

According to photoelectron spectroscopy (PES) (9), the band of the $\tilde{A}^2\Pi_u$ state of CS_2^+ consists of a series of peaks spreading over

approximately 1 eV. At energies higher than ~13.2 eV, the Franck-Condon factors for excitation to $(\nu_1 > 7,0,0)$ of CS_2^+ become vanishingly small. Probably, the yield of CS_3^+ and S_2^+ below the excitation energy of the $\tilde{B}^2\Sigma_u^+$ state and above the appearance energies of these two species have their origin from autoionization processes involving the Rydberg states in this spectral region. Although resonances which arise from Rydberg series III and IV are not observed in the PIE data for CS_3^+, Rydberg series V(n = 4, 5, 6, 7 and 8) is quite well-resolved. The autoionization peaks observed are listed in Table 1 where they can be compared with the corresponding members of series V of CS_2. With a data analysis similar to that given in Section II, the potential energy, $D^*(n)$, of the excited dimer $CS_2^*(V,n) \cdot CS_2$ at the equilibrium nuclear geometry of $(CS_2)_2$ can be deduced. $D^*(n)$ is found to increase smoothly as a function of the principal quantum number n. Larzilliere and Damany (10) suggested Rydberg series V to be an npσ-series. Adapting the linear or near linear configuration for $(CS_2)_2$ as discussed in the previous section, the perturbation introduced by an electron in a lower member of a npσ-series (series V) to the bonding of the ion core $(CS_2)_2^+$ at the equilibrium nuclear geometry of $(CS_2)_2$ is expected to be more substantial than that caused by an electron in a Rydberg orbital with higher n value. Using similar arguments as discussed in Section II, the functional dependence of $D^*(n)$ on n observed here is consistent with the linear picture for $(CS_2)_2$.

Only two members, n = 4 and 5 of Rydberg series V, can be identified in the PIE curve for S_2^+. The shifts in energy of these peaks are found

Table 1. Potential energy of $CS_2^*(V,n)$-CS_2 at the equilibrium nuclear configuration of $(CS_2)_2$

CS_2 Rydberg Series[a] V ($np\sigma$) (eV)	$E_1^*(n)$[b] (eV)	$E_2^*(n)$[c] (eV)	$\Delta E(n)$[d] (eV)	$D^*(n)$[e] (eV)
n = 4 14.938 (830 Å)	14.943 (829.7 Å)	14.882 (833.1 Å)	0.061	0.113
5 15.427 (803.7 Å)	15.431 (803.5 Å)	15.333 (808.6 Å)	0.098	0.150
6 15.694 (790 Å)	15.694 (790 Å)	15.584 (795.6 Å)	0.110	0.162
7 15.845 (782.5 Å)	15.841 (782.7 Å)	15.722 (788.6 Å)	0.119	0.171
8 15.926 (788.5 Å)	15.926 (778.5 Å)	15.802 (784.6 Å)	0.124	0.176
Series limit				
16.187 (765.95 Å)	$E_1^*(n\to\infty)$ = 16.187	$E_2^*(n\to\infty)$ = 16.029 (773.5 Å)	$\Delta E(n\to\infty)$ = 0.158	$D(\tilde{C}^2\Sigma_g^+)$[f] = 0.210 eV

[a] Ref. 8.

[b] Autoionization peak observed in the PIE curve for CS_2^+.

[c] This value is interpreted as the energy difference between the potential energy curve of $(CS_2)_2$ and $CS_2^*(n) \cdot CS_2$ at the equilibrium geometry of $(CS_2)_2$.

[d] $\Delta E(n) = E_1^*(n) - E_2^*(n)$.

[e] The potential energy of $CS_2^*(V,n) \cdot CS_2$ at the equilibrium nuclear configuration of $(CS_2)_2$.

[f] The potential energy of $CS_2^+(\tilde{C}^2\Sigma_g^+) \cdot CS_2$ at the equilibrium nuclear configuration of $(CS_2)_2$.

to be the same as those resolved in the CS_3^+ spectrum. Another interesting feature observed in the S_2^+ spectrum is the step at 16.03 eV (773.5 Å). The difference in energy of this step and the converging limit of series V of CS_2 (16.187 eV) is 0.158 eV. The fact that this value is very close to the shifts in energy measured for the higher members of Rydberg series V, lead us again to identify the step at 16.03 eV (773.5 Å) as the converging limit for series V of $(CS_2)_2$. A simple calculation gives a value for the potential energy, $D(\tilde{C}^2\Sigma_g^+)$, for $CS_2^+(\tilde{C}^2\Sigma_g^+) \cdot CS_2$ at the equilibrium nuclear configuration of $(CS_2)_2$ to be 0.210 eV. Since one would expect $D(\tilde{B}^2\Sigma_u^+)$ and $D(\tilde{C}^2\Sigma_g^+)$ to depend strongly upon charge multipole interactions between CS_2^+ and CS_2, and thus the charge distribution of CS_2, it is quite interesting to find that $D(\tilde{B}^2\Sigma_u^+)$ is essentially equal to $D(\tilde{C}^2\Sigma_g^+)$ within the uncertainties of this experiment. Furthermore, if the reaction cross sections for 7 is the same for CS_2^+ in the $\tilde{B}^2\Sigma_u^+$ and $\tilde{C}^2\Sigma_g^+$ states, one would expect to find a smooth transition in the region of the converging limit for series V as shown in the PIE curve for CS_2^+ in Fig. 6(a). The observation of an increase in the S_2^+ PIE at the converging limit of series V in CS_2 clearly reveals that the reaction cross sections for reaction 7 with CS_2^+ in the $\tilde{C}^2\Sigma_g^+$ state is higher than when CS_2^+ is in the $\tilde{B}^2\Sigma_u^+$ state. Since no autoionization structure is evident in the PIE curve for CS_2^+ beyond the $\tilde{C}^2\Sigma_g^+$ state, it is assumed that the relative populations of the $\tilde{X}^2\Pi_g$, $\tilde{A}^2\Pi_u$, $\tilde{B}^2\Sigma_u^+$ and $\tilde{C}^2\Sigma_g^+$ states resulting from photoionization with photon energy higher than the $\tilde{C}^2\Sigma_g^+$ state at ∿765 Å are equal to the relative Franck-Condon factors derived from HeI (584 Å) photoelectron spectroscopic

data of CS_2. However, $CS_2^+(\tilde{X}^2\Pi_g,v)$ and $CS_2^+(\tilde{A}^2\Pi_u,v)$ produced by direct ionization will not have sufficient energy for reaction 7 to proceed because the experimental appearance energy for 7 is higher than the energy contents of $CS_2^+(\tilde{X}^2\Pi_g)$ or $CS_2^+(\tilde{A}^2\Pi_u)$ in vibrational states which are accessible to direct ionization processes. Therefore, we can further assume that the S_2^+ ions arise mainly from CS_2^+ populated in various vibrational levels of the $\tilde{B}^2\Sigma_u^+$ and $\tilde{C}^2\Sigma_g^+$ states (11). From the relative Franck-Condon factors for the $\tilde{B}^2\Sigma_u^+$ and $\tilde{C}^2\Sigma_g^+$ states obtained from PES, and attributing the increase in PIE for S_2^+ to higher reactivity of $CS_2^+(\tilde{C}^2\Sigma_g^+)$, the ratio of the cross sections for reaction 7 with CS_2^+ in the $\tilde{B}^2\Sigma_g^+$ state to that with CS_2^+ in the $\tilde{C}^2\Sigma_g^+$ state is deduced to be 0.34.

In the wavelength region 740-773.5 Å, the PIE of S_2^+ remains nearly constant. Starting at ∿740 Å, an abrupt increase in the PIE for S_2^+ can be seen. The general shape of the PIE curve for S_2^+ in this region is consistent with that obtained in a high resolution photoionization study of CS_2 by Eland and Berkowitz (5). Discrete structure resolved here is found to match the members of Rydberg series VIII (n = 4, 5 and 6) observed in absorption experiments (12,13), which converge to a sixth ionization potential of CS_2 at 19.38 eV. In addition, a slight step or a change in slope which can be seen at 16.837 eV (746.4 ± 1.5 Å) is found to be equal to the thermochemical threshold for the process, $CS_2 + h\nu \rightarrow S_2^+ + C + e^-$. This value is also in good agreement with the threshold for formation of the S_2^+ ion located by Coppens, Raynaert and Drowart (14).

The general shape of the PIE curve for $C_2S_3^+$ is found to increase monotonically above the threshold (Fig. 3(b)). Figure 3(a) shows a portion of the curve depicted in Fig. 3(b) obtained with longer counting times. Structure which can be correlated with members of Rydberg series V (n = 4 and 5) is also resolved. The red-shifts of these peaks determined from the $C_2S_3^+$ spectrum are again in agreement with those observed in the CS_3^+ and S_2^+ curves. This observation suggests that CS_3^+, S_2^+ and $C_2S_3^+$ at the peaks are formed via the same intermediate complex, which in this case is primarily the excited dimer, $CS_2^*(V,n) \cdot CS_2$.

At present, there appears to be some controversy about the shape at the threshold for the fragmental process, $CS_2 + h\nu \rightarrow CS^+ + S + e$. According to Coppens et al. (14), a step at 787 ± 1 Å is observed in the PIE curve for CS^+. However, Eland and Berkowitz found the PIE curve tails away smoothly below the $\tilde{C}^2\Sigma_g^+$ state and there is no step visible at this wavelength. The PIE curve for CS^+ in the region 680-800 Å has been re-examined and the spectrum obtained is shown in Fig. 4. The structure observed by Coppens et al. is clearly evident. Due to collisional dissociation processes in the gas-cell experiment, this slight structure was probably smeared out to become unrecognizable. The appearance energy for the formation of CS^+ from CS_2 is determined to be 15.80 ± 0.03 eV (784.5 ± 1.5 Å) which is in agreement with the value obtained by Coppens et al. and is found to coincide with the thermochemical threshold for CS^+ formation from CS_2. The smoothly diminishing structure in the PIE curve for CS^+ below the $\tilde{C}^2\Sigma_g^+$ state probably has its origin in the predissociation of CS_2^+. From arguments similar to those

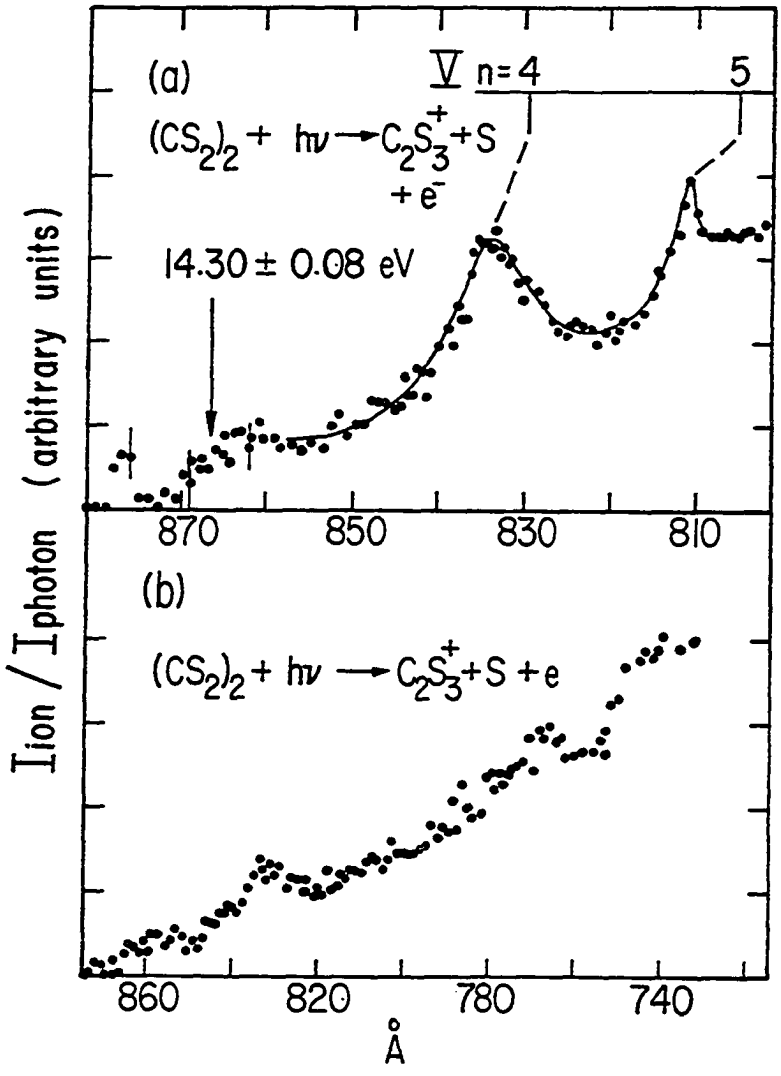

Figure 3. PIE curve for $C_2S_3^+$ (a) in the region 800-885 Å and (b) in the region 715-880 Å plotted at intervals of 1 Å

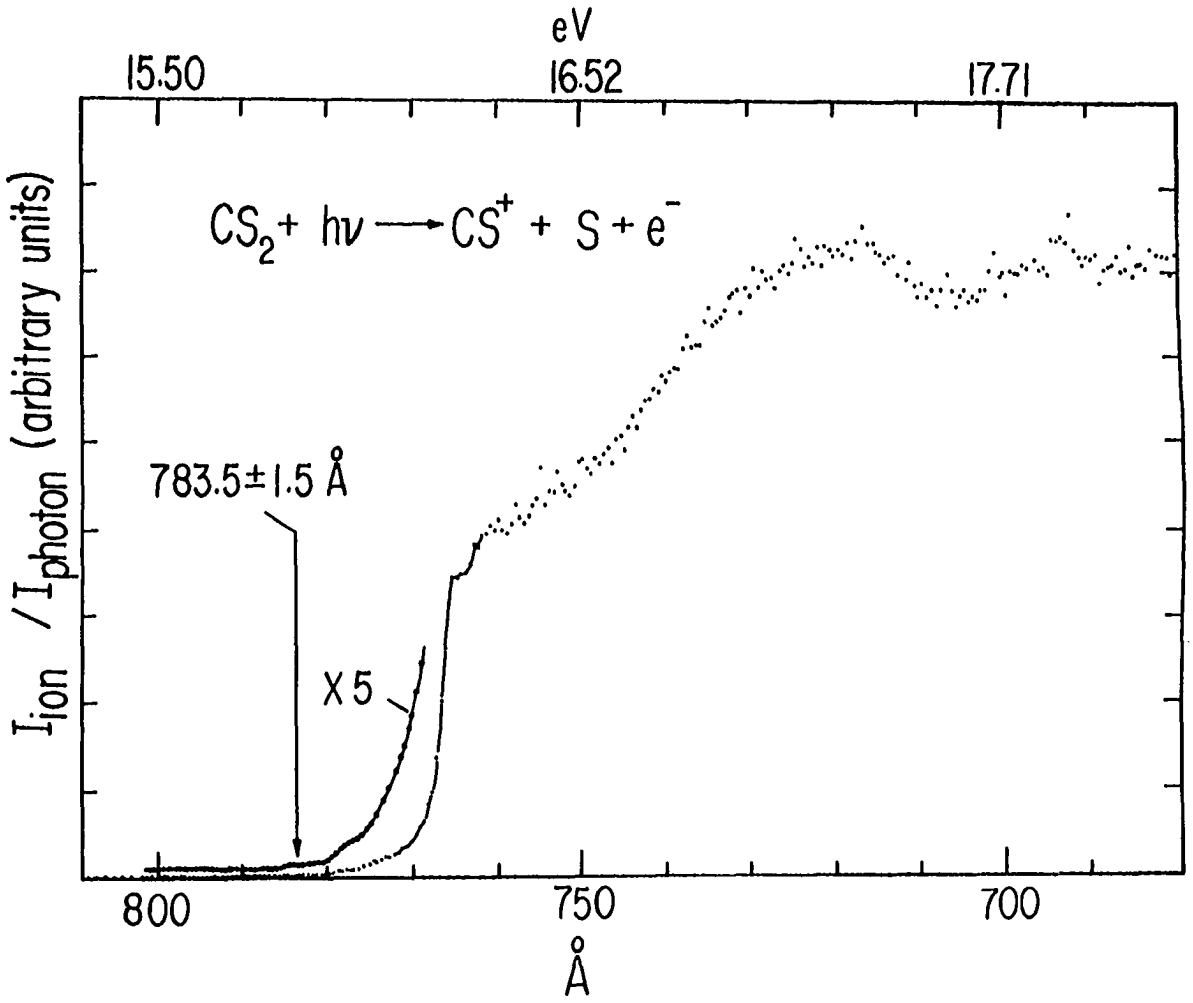

Figure 4. PIE curve for CS^+ in the region 680-810 Å

discussed in a recent paper on the observation of the OH^+ fragment threshold from H_2O (15), an increase in the ion intensity at the fragment onset is anticipated if predissociation leading to the fragment occurred so rapidly that the ionic processes will compete more effectively with the neutral processes above the onset of the fragmentation. The observation of the step-like structure or changes in slope at the onset of S_2^+ at 736.4 ± 1.5 Å and CS^+ at 784.5 ± 1.5 Å seems to be in accordance with this expectation.

The PIE curve for CS_4^+ is shown in Fig. 5. A very weak CS_4^+ signal was found to persist at photon wavelengths longer than 800 Å. The PIE for CS_4^+ below ∿15.50 eV (800 Å) essentially remains constant. A pressure dependence study of the CS_4^+ signal in the range ∿800-900 Å showed that the pressure dependence of CS_4^+ was identical to that of $(CS_2)_3^+$ leading to the conclusion that CS_4^+ formed in this region originates primarily from the reaction, $(CS_2)_3 + h\nu \rightarrow CS_4^+ + 2CS + e$; however, due to the extremely low signal level for CS_4^+ in this wavelength region, it was not possible to obtain a reliable value for the threshold of this process. If it is assumed that the CS_4^+ PIE originating from $(CS_2)_3$ remains constant at wavelengths shorter than 800 Å, the appearance energy for the process, $(CS_2)_2 + h\nu \rightarrow CS_4^+ + C + e$ is determined to be 15.66 ± 0.20 eV.

The relative intensities of $(CS_2)_2^+$, CS_3^+, S_2^+, $C_2S_3^+$ and CS_4^+ at 833 Å, the peak position of Rydberg series V (n = 4) in $(CS_2)_2$, are found to be 1, 0.12, 0.02, 0.003 and 0.001, respectively. From this, the PIE curves for $(CS_2)_2^+$, CS_3^+, S_2^+, $C_2S_3^+$ and CS_4^+ can be normalized. The relative

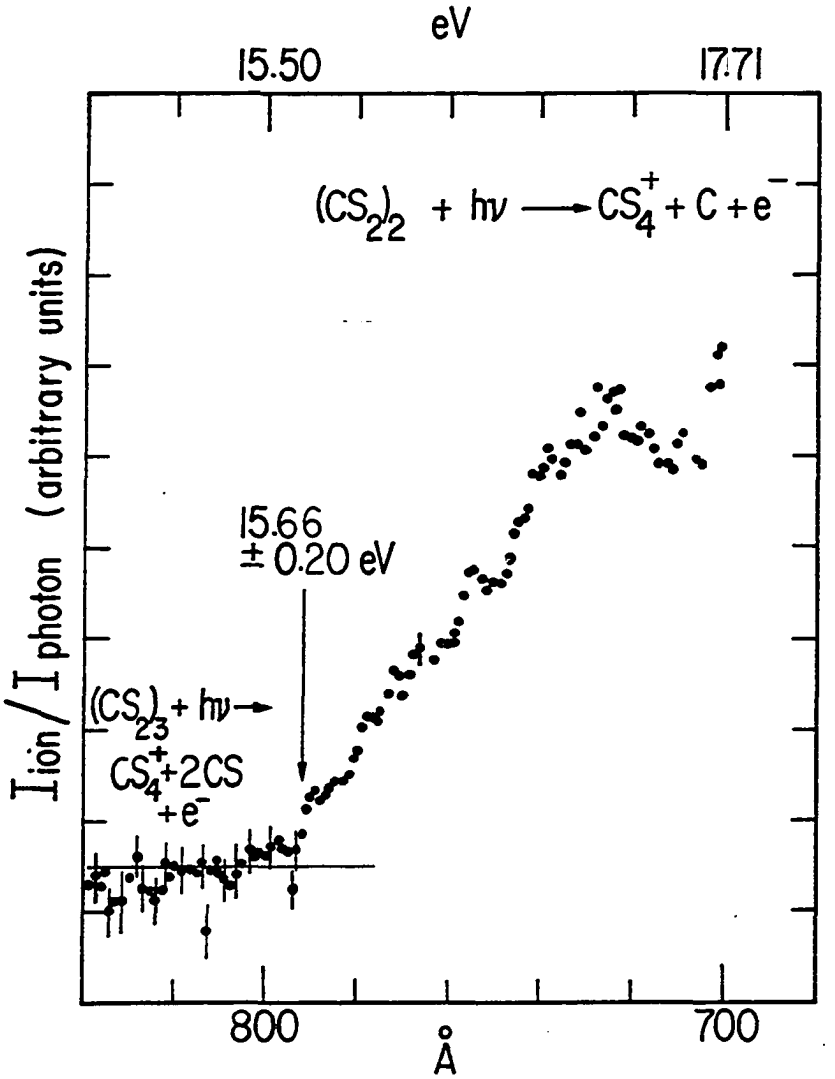

Figure 5. PIE curve for CS_4^+ in the region 700-820 Å plotted at intervals of 1 Å

cross sections, $\sigma CS_3^+(n)$, $\sigma S_2^+(n)$ and $\sigma C_2S_3^+(n)$, for the chemiionization processes, 1, 2 and 3, respectively, are deduced and listed in Table 2, where $\sigma CS_3^+(n)$, $\sigma S_2^+(n)$ and $\sigma C_2S_3^+(n)$ have been normalized for $\sigma CS_3^+(V,n=4)$.

The appearance of the $C_2S_3^+$ and CS_4^+ channels, and the monatonical increases in PIE for these species towards higher energy are consistent with the decreasing trend of the yield for $(CS_2)_2^+$ in the same wavelength region. The discrete structure corresponding to Rydberg series V(n), which is resolved in the CS_3^+, S_2^+ and $C_2S_3^+$ spectra, is not evident in the PIE curve for $(CS_2)_2^+$, thus it is difficult to determine accurately the portion of $(CS_2)_2^+$ formed by the autoionization processes. It is possible, however, to estimate the relative importance of $(CS_2)_2^+$ arising from autoionization compared to that produced by direct ionization processes if the following assumptions are made. Since the oscillator strength for the excitation to a Rydberg level (n) approaches zero as $n \to \infty$, one would expect that no $(CS_2)_2^+$ ions will be produced by autoionization at wavelengths shorter or equal to the converging limit (773.5 Å) of series V of $(CS_2)_2$. Furthermore, from the PIE curves of CS_3^+, $C_2S_3^+$ and S_2^+, Rydberg series V(n = 4) is found to shift towards the red by ∿3 Å with respect to the corresponding autoionization peak observed in the CS_2^+ spectrum. Hence, it is reasonable to assume that the curved structure of the $(CS_2)_2^+$ spectrum in the region ∿833-860 Å is also shifted by the same amount. Adapting these assumptions, a base line can be drawn as shown in Fig. 6(b), which allows an estimate of the contribution of $(CS_2)_2^+$ formed from the associative ionization processes 5. The estimated reaction cross sections, $\sigma C_2S_4^+(n)$, for 5 which have

Table 2. Relative cross sections for the chemiionization processes $CS_2^*(V,n) + CS_2 \rightarrow CS_3^+ + CS + e$, $S_2^+ + 2CS + e$, $C_2S_3^+ + S + e$, and $(CS_2)_2^+ + e$ [normalized for $\sigma CS_3(n = 4)$]

Rydberg Series V $np\sigma$	$\sigma CS_3^+(n)$	$\sigma S_2^+(n)$	$\sigma C_2S_3^+(n)$	$\sigma C_2S_4^+(n)$[a]
4	1	0.19	0.02	1.3
5	0.32	0.10	0.01	2.0
6	0.24	--	--	2.2
7	0.23	--	--	2.5
8	0.23	--	--	3.0

[a]Since the structure is not well resolved, these values must be considered as crude estimates.

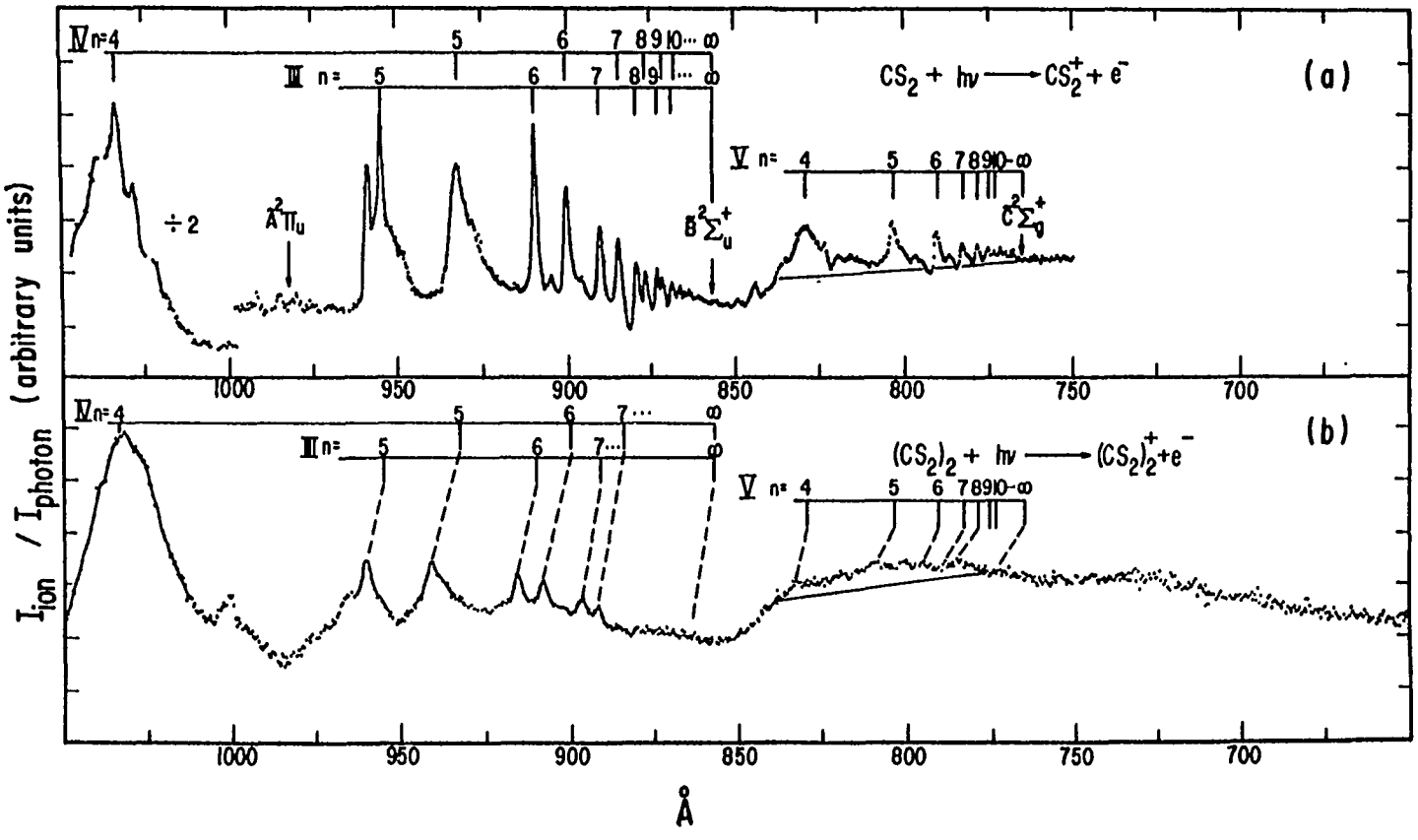

Figure 6. The CS_2 monomer and dimer curves. (a) PIE curve for CS_2^+ in the region 750-1050 Å. (b) PIE curve for $(CS_2)_2^+$ in the region 600-1050 Å

been normalized to $\sigma CS_3^+(n = 4)$, are included in Table 2. A noticeable trend for the relative chemiionization cross sections derived in this experiment is that $\sigma CS_3^+(n)$, $\sigma S_2^+(n)$ and $\sigma C_2S_3^+(n)$ decrease as n increases, whereas $\sigma C_2S_4^+(n)$ is found to have the opposite functional behavior on n. For the energy of a Rydberg electron to be effective in promoting the chemical reactions such as 1, 2 and 3, the Rydberg electron has to be able to couple with the ion core efficiently. Since the coupling between a Rydberg electron and the ion core, $(CS_2)_2^+$, decreases as n increases (16), $\sigma CS_3^+(n)$, $\sigma S_2^+(n)$ and $\sigma C_2S_3^+(n)$ should be larger for the electron in the lower member of a Rydberg series. On the other hand, the energy which is needed to ionize the molecule becomes smaller for an electron in a Rydberg level with higher n values, therefore, the behavior of $\sigma C_2S_4^+(n)$ as a function of n observed here also seems to be in accordance with this interpretation.

From the relative intensities of CS_3^+, S_2^+ and $C_2S_3^+$ at ~855 Å, the relative cross sections, σCS_3^+, σS_2^+ and $\sigma C_2S_3^+$, for the ion-molecule reactions 6, 7 and 8, with CS_2^+ in the $\tilde{B}^2\Sigma_u^+$ state are deduced (17). Similarly, from the relative intensity of S_2^+ and CS_4^+ at ~765 Å, σS_2^+ and σCS_4^+ for the reactions 7 and 9 can be derived. The relative values for σCS_3^+, σS_2^+, $\sigma C_2S_3^+$ and σCS_4^+ which have been normalized for $\sigma CS_3^+(\tilde{B}^2\Sigma_u^+$ v = 0), determined in this experiment are listed in Table 3. The geometry of the CS_3^+ ion is unknown, however, since the electronegativities for C and S are almost the same and the size of S is larger than that of C, the S^+ ion is probably attached to an S atom in CS_3^+. Considering the experimental appearance energy for S_2^+ is greater than that

Table 3. Relative cross sections for the ion-molecule reactions $CS_2^+(\tilde{B}^2\Sigma_u^+$ or $\tilde{C}^2\Sigma_g^+) + CS_2 \rightarrow CS_3^+ + CS$, $S_2^+ + 2CS$, $C_2S_3^+ + S$, and $CS_4^+ + C$ [normalized for $\sigma CS_3^+(\tilde{B}^2\Sigma_u^+$, $v = 0)$]

States[a]	$\sigma(CS_3^+)$	$\sigma(S_2^+)$	$\sigma(C_2S_3^+)$	$\sigma(CS_4^+)$
$\tilde{B}^2\Sigma_u^+$ $v = 0$	1	0.13	0.03	--
$\tilde{C}^2\Sigma_g^+$ $v = 0$	-	0.38	--	~0.09

[a]Ref. 11.

for CS_3^+, it is likely that CS_3^+ is the intermediate for the formation of S_2^+. If the $(CS_2)_2$ is indeed linear as suggested by the symmetry argument, we might be sampling the reactions, CS_2^+(or $CS_2^*(n)$) + CS_2, colliding in a linear configuration. Higher values for $\sigma CS_3^+(n)$, $\sigma S_2^+(n)$, σCS_3^+ and σS_2^+ in comparison to $\sigma CS_4^+(n)$, $\sigma C_2S_3^+(n)$, σCS_4^+ and $\sigma C_2S_3^+$ could probably result from a more favorable collisional complex prepared in this study. Using this picture, one can also rationalize the observed relative cross sections for the formation of CS_3^+ and S_2^+ with CS_2^+ in the $\tilde{B}^2\Sigma_u^+$ and $\tilde{A}^2\Pi_u$ states. The $\tilde{B}^2\Sigma_u^+$ and $\tilde{A}^2\Pi_u$ states are formed by ejecting the electrons from σ_u and π_u molecular orbitals to the continuum, respectively. The $CS_2^+(\tilde{B}^2\Sigma_u^+)$ ion which has a vacant site in the σ-type orbital should be more favorable for the attack of the neutral CS_2 molecule than the $CS_2^+(\tilde{A}^2\Pi_u)$ ion, if CS_2 comes in along the molecular axis of CS_2^+.

The appearance energies determined in the present experiment for the formation of CS_3^+, $C_2S_3^+$ and CS_4^+ from $(CS_2)_2$ are 13.12 ± 0.02 eV, 14.30 ± 0.08 eV and 15.66 ± 0.20 eV, respectively. From the known appearance energies of the fragmentation processes, $CS_2 + h\nu \rightarrow CS + S^+ + e$ (5), $CS^+ + S + e$ (14), and $S_2^+ + C + e$ (14), and the estimated binding energies for $CS_2 + S^+$, $CS_2 + CS^+$, and $CS_2 + S_2^+$ are deduced to be 1.72 ± 0.04 eV, 1.56 ± 0.06 eV, and 1.23 ± 0.25 eV, respectively. The latter value is found to be higher than that obtained previously in a high pressure mass spectrometry experiment (18). Using the known heats of formation at 0K for S, CS_2, C (19), CS_2^+ (20) and CS (21) from the literature, ΔH°_{f0} for CS_3^+, $C_2S_3^+$ and CS_4^+ are determined to be 291.7 ± 1.7 kcal/mol, 318 ± 3 kcal/mol, and 246 ± 6 kcal/mol, respectively. The

energetics of the CS_2^+ and $CS_2^+ + CS_2$ systems which have been determined in this experiment (22) are summarized and shown in Fig. 7.

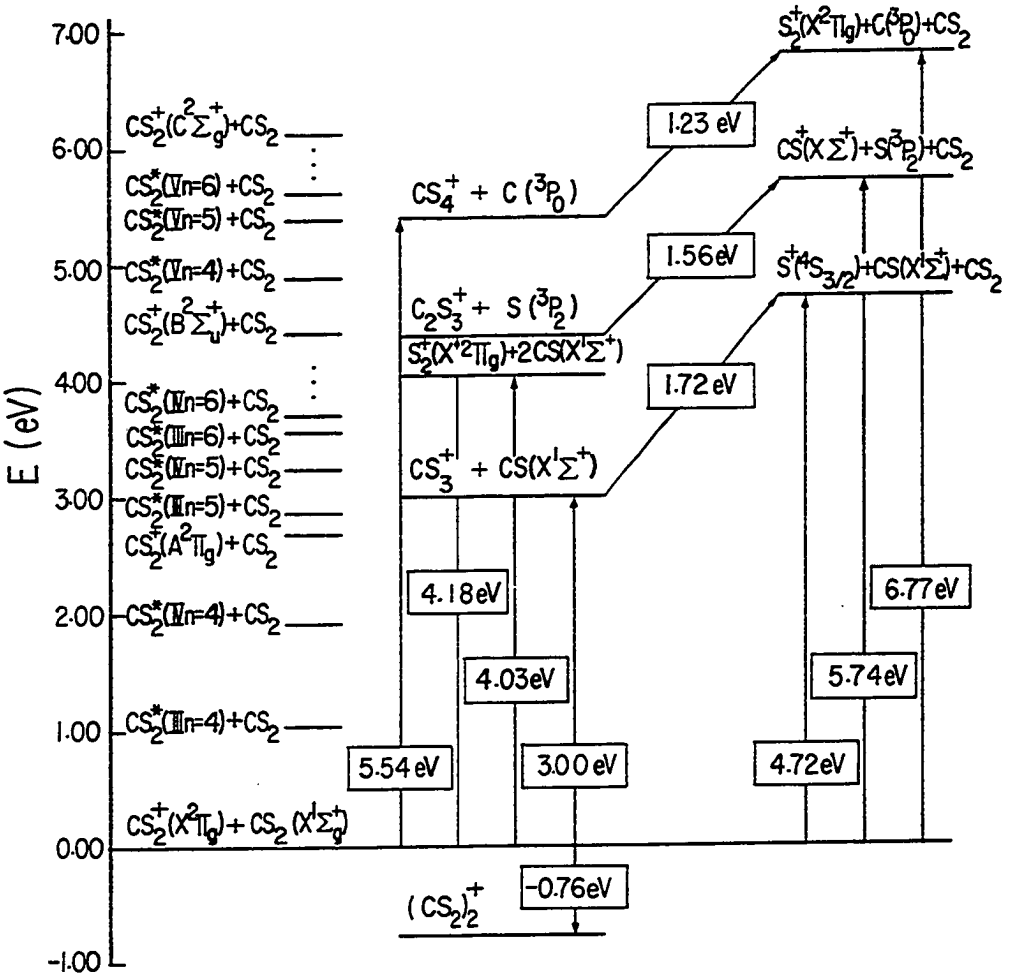

Figure 7. Energetics of the CS_2^+ and $CS_2^+ + CS_2$ systems

REFERENCES

1. R. F. Stebbings, in Proceedings of the International Conference on the Physics of Electronic and Atomic Collisions, No. 10 (North-Holland, Amsterdam, 1977), p. 549.

2. R. F. Stebbings, in Advances in Atomic and Molecular Physics, edited by D. R. Bates and B. Bederson (Academic, New York, 1979), Vol. 15, p. 77.

3. J. H. D. Eland, M. Devoret and S. Leach, Chem. Phys. Lett. 43, 97 (1976).

4. W. H. Smith, J. Chem. Phys. 51, 3410 (1969).

5. J. H. D. Eland and J. Berkowitz, J. Chem. Phys. 70, 5151 (1979).

6. W. M. Trott, N. C. Blais and E. A. Walters, J. Chem. Phys. 69, 3150 (1978).

7. J. O. Hirschfelder, C. F. Curtiss and R. B. Bird, Molecular Theory of Gases and Liquids (Wiley, New York, 1964), p. 1112.

8. G. R. Cook and M. Ogawa, J. Chem. Phys. 51, 2419 (1969).

9. C. R. Brundle and D. W. Turner, Int. J. Mass Spectrom. Ion Phys. 2, 195 (1969).

10. M. Larzilliere and N. Damany, Can. J. Phys. 56, 1150 (1978).

11. Since both the $\tilde{B}^2\Sigma_u^+$ and $\tilde{C}^2\Sigma_g^+$ states of CS_2 are nonbonding states, the $CS_2^+(\tilde{B}^2\Sigma_u^+$ or $\tilde{C}^2\Sigma_g^+)$ ions formed by direct ionization are predominately in the ground vibrational state, v = 0.

12. Y. Tanaka, A. S. Jursa and F. J. LeBlanc, J. Chem. Phys. 32, 1205 (1960).

13. M. Ogawa and H. C. Chang, Can. J. Phys. 48, 2455 (1970).

14. P. Coppens, J. C. Reynaert and J. Drowart, J. Chem. Soc. Faraday Trans. 2 75, 292 (1979).

15. R. Stockbauer, J. Chem. Phys. 72, 5277 (1980).

16. For a Rydberg state of sufficiently large n, the wavefunction for the Rydberg electron in the region of the core is proportional to $(n^*)^{-3/2}$, where n^* is the effective principal quantum number. The probability density of the Rydberg electron in the region of the core is thus proportional to $(n^*)^{-3}$.

17. It is assumed that the perturbation from autoionization is negligible and the CS_2^+ ions are only produced by direct ionization processes at this wavelength. Furthermore, the relative population of CS_2^+ formed in the vibrational levels of the $\tilde{X}^2\Pi_g$, $\tilde{A}^2\Pi_u$, and $\tilde{B}^2\Sigma_u^+$ states are also assumed to be governed only by the relative Franck-Condon factors derived from PES.

18. M. Meot-Ner (Mautner) and F. H. Field, J. Chem. Phys. 66, 4527 (1977).

19. JANAF Thermochemical Tables, Nat. Stand. Ref. Data Ser. Nat. Bur. Stand. 37 (1971).

20. Energetics of gaseous ions, J. Phys. Chem. Ref. Data, edited by H. M. Rosenstock, K. Draxl, B. W. Steiner and J. T. Herron, (Nat. Bur. Stand.) (1977), Vol. 6, Suppl. 1, p. 420.

21. The value for $\Delta H^\circ_{f0}(CS) = 65.3 \pm 0.3$ kcal/mol is obtained from Ref. 5.

22. The dissociation energy of $(CS_2)_2^+$ is taken from Section II. The appearance energy for the formation of S^+ from CS_2 is obtained from Ref. 5.

SECTION IV.

A MOLECULAR BEAM PHOTOIONIZATION STUDY OF OCS, $(OCS)_2$, $(OCS)_3$, AND $OCS \cdot CS_2$

INTRODUCTION

One of the most accurate methods of determining ionization energies (IE) is vacuum ultraviolet (VUV) absorption spectroscopy. In an absorption experiment, when high enough resolution can be employed to resolve the rotational structure of the Rydberg series and the higher members of the series can be identified, rotational analysis of this structure can lead to very accurate values for the IEs. At sufficiently large n values, however, there are often strong interactions between Rydberg states of different n and ℓ values, where n and ℓ are the principle and orbital angular momentum quantum numbers, respectively. The coupling conditions and the rotational structure of the bands which result from this mixing are often complicated (1). Although a substantial number of Rydberg series have been observed in the spectra of diatomic molecules, only a few of these have been analyzed in detail. In the cases where the rotational structure has not been resolved, the band origins of members of Rydberg series will be difficult to establish due to finite rotational and vibrational temperatures of the sample gas, as well as the differences in structure of the higher Rydberg states and that of the ground state. Individual bands will be shaded either to the red or to the blue depending on the direction and magnitude of the geometry change. The IEs determined from fitting these Rydberg series will thus suffer from some appreciable uncertainties. In the photoionization study of CS_2, it was shown by using the molecular beam method to relax the rotational temperature of the sample gas that high resolution photoionization studies provide a direct and accurate means of determining IEs. In

this paper, a high resolution photoionization study of OCS near the threshold is reported.

The previous studies of $(CS_2)_2$ (2,3) suggest that by measuring the shifts in energy of the Rydberg series of the monomer in the dimer, and from the symmetry of the Rydberg orbital, structural information of the neutral dimer can be obtained. This idea has been extended to the study of heterogeneous dimers. Measuring the shifts in energy of the corresponding Rydberg series of OCS and CS_2 in the dimer $OCS \cdot CS_2$ should provide insights concerning the orientation of CS_2 and OCS with respect to one another. This is the primary motive in the photoionization study of the $OCS \cdot CS_2$ dimer. The PIE curve for $(OCS)_2^+$ has also been measured so that a comparison can be made with the $(OCS \cdot CS_2)^+$ spectrum.

Rydberg transitions in the VUV region of many molecules, in the presence of a moderate pressure of perturber gases, are found to broaden asymmetrically to the high (4) or low (5) frequency sides. Blue shifts of Rydberg absorption bands of many molecules in the solid state have also been identified (6). These shifts are attributed to the exchange repulsion experienced by an absorber-perturber pair when the absorber increases its effective diameter as occurs in Rydberg excitations. Since a dimer will provide an isolated absorber-perturber pair with a given geometry for the study of this mechanism, photoionization studies of dimers are expected to also provide insights into pressure effects on VUV spectra.

EXPERIMENTAL

The carbonyl sulfide molecular beam was produced by expanding the gas through a 50 μm diameter nozzle orifice at a stagnation pressure of ∿800 Torr. The OCS used was obtained from Matheson (97.5% minimum purity). The $OCS \cdot CS_2$ molecular beam was produced by seeding CS_2 vapor (∿130 Torr) at 0°C in ∿700 Torr of OCS, then expanding the mixture through the nozzle.

The PIE curve for OCS^+ near the threshold (Fig. 1) was obtained with an optical resolution of 0.14 Å (FWHM) and the Ar continuum as the light source. Data points were taken at 0.05 Å intervals. The remaining PIE curves were obtained with a resolution of 1.4 Å (FWHM) and using the He Hopfield continuum below ∿1000 Å. Each PIE curve was scanned at least twice and the structure in the curves was found to be reproducible.

RESULTS AND DISCUSSION

As shown in Fig. 1, the PIE curve for OCS^+ in the region 1080-1111 Å is dominated by complicated autoionization structures. The first onset is very sharp with an uncertainty for the initial threshold of ±0.15 Å. The next step was found to be at 1104.95 Å. Thus, the IEs for the $\tilde{X}^2\Pi_{3/2}$ and $^2\Pi_{1/2}$ states of OCS were determined to be 11.1736 ± 0.0015 eV and 11.2207 ± 0.0015 eV, respectively. Similar to the PIE curve for CS_2^+, Rydberg series manifested as autoionization peaks on the first step can be seen in the PIE curve for OCS^+. Assuming the converging limit of this series to be the $^2\Pi_{1/2}$ threshold at 90502 cm^{-1}, autoionization peaks have been fit with the Rydberg equation

$$\nu_n = [90502 - R/(n + 0.6)^2] \text{ cm}^{-1}$$

where R is the Rydberg constant, n is the nominal principal quantum number, and ν_n is the peak position in cm^{-1}. The calculated values of ν_n are listed in Table 1 where they can be compared with the observed peak positions of the autoionization features. It is interesting to note that the intensities of members n = 20, 21 and n > 22 are much weaker than that of other members of the series. A previous study (7) indicated that nearly half of the absorption leads to dissociation in this region. The weakness of these features is probably due to stronger predissociation in comparison to autoionization for these members. The fit in general is satisfactory except for member n = 20. In view of the expectation that Rydberg series converging to a different threshold could interact with each other in this region, it is fortuitous to find a good

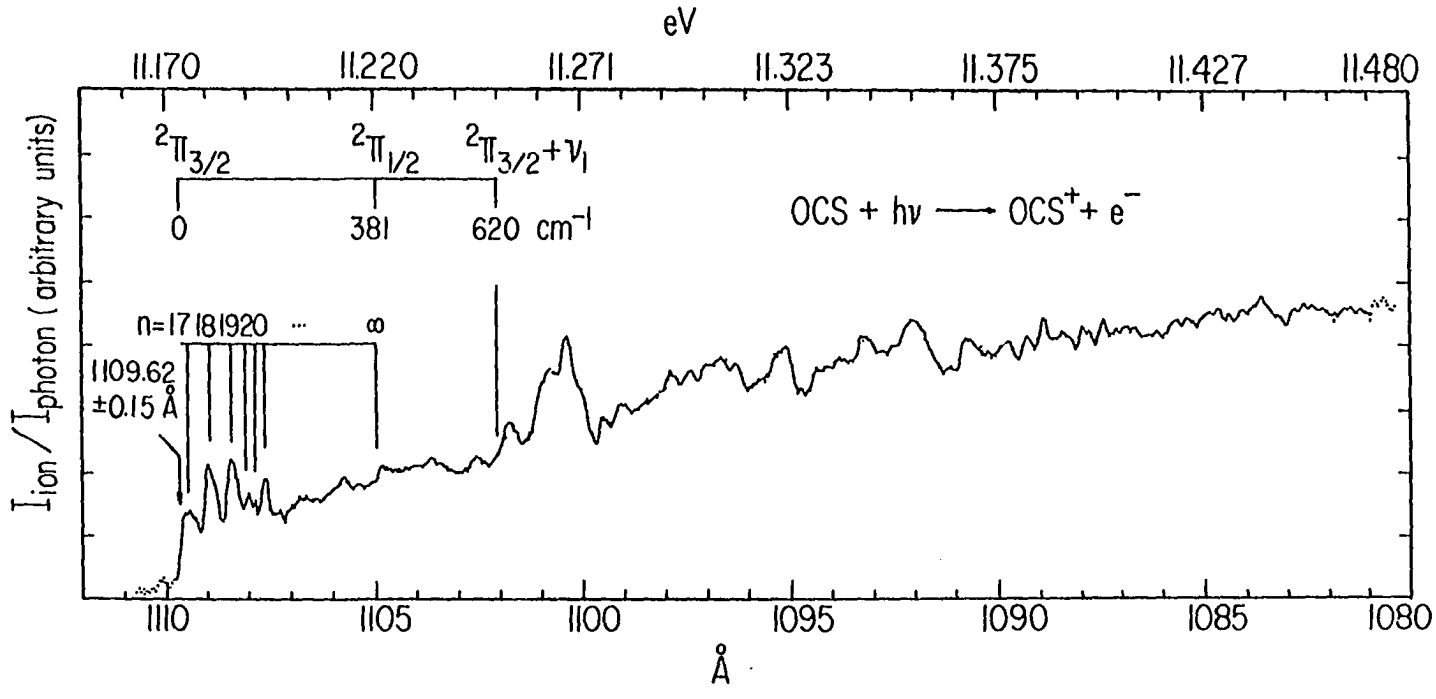

Figure 1. PIE curve for OCS^+ in the region 1080-1111 Å obtained using a wavelength resolution of 0.14 Å (FWHM) and the Ar continuum as the light source

Table 1. Rydberg series converging to the $^2\Pi_{1/2}$ threshold

n	ν_{obs} (cm^{-1})(10 cm^{-1})	ν_n (cm^{-1})[a]
17	90143 (1109.35 Å)	90148
18	90184 (1108.85 Å)	90185
19	90220 (1108.40 Å)	90216
20	90257 (1107.95 Å)	90243
21	90269 (1107.80 Å)	90267
22	90285 (1107.60 Å)	90287

$IE(^2\Pi_{1/2}) = 90502 \pm 12\ cm^{-1}$

[a] $\nu_n = 90502 - R/(n+0.6)^2$.

fit of the series with a constant quantum defect. The measured IEs for the $\tilde{X}^2\Pi_{3/2}$ and $^2\Pi_{1/2}$ states for OCS in this study are found to be in good agreement with values obtained from photoelectron spectroscopy (8), photoionization mass spectrometry (7,9), and absorption spectroscopy (7) (see Table 2). The spin-orbit splitting is determined to be 381 ± 24 cm^{-1} which is also consistent with previous measurements (7-12).

The step at 1102.05 Å is attributed to the onset of $\tilde{X}^2\Pi_{3/2} + \nu_1$, where ν_1 represents the symmetric stretching mode of OCS^+. This gives a value of 620 ± 24 cm^{-1} for ν_1 and is in agreement with values obtained in Refs. 7 and 10. Following this assignment, a step found at 1094.6 Å which is 1237 cm^{-1} above the first onset can be assigned as the threshold of $\tilde{X}^2\Pi_{3/2} + 2\nu_1$. Based on photoelectron data (10) and the analysis of the emission spectrum (13) of OCS^+, the vibrational frequency for the asymmetric stretching mode, ν_3, of the $\tilde{X}^2\Pi_{3/2}$ state is equal to 2000 ± 50 cm^{-1}. Thus, the slight step at 1085.95 Å, which is 1964 cm^{-1} above the the first onset, probably corresponds to the threshold for excitation of $^2\Pi_{3/2} + \nu_3$. Due to interference of autoionization features, a structure corresponding to the onset of $^2\Pi_{1/2} + \nu_1$ is not evident.

The PIE curves for $(OCS)_2^+$ and $(OCS)_3^+$ in the region 750-1200 Å, obtained using a wavelength resolution of 1.4 Å (FWHM), are shown in Figs. 2(b) and 2(c), respectively. The PIE curve for OCS^+, measured using the same optical resolution, is plotted in Fig. 2(a) for comparison. The PIE spectrum for OCS^+ measured in this experiment is consistent with that obtained previously by Dibeler and Walker (9) and essentially reproduces most of the prominent structures resolved in a high resolution

Table 2. Summary of energetic information for OCS, OCS_2, $(OCS)_3$, and $OCS\text{-}CS_2$

Ion	Ionization energies (eV)	
	This Work	Other Techniques
$OCS^+(^2\Pi_{3/2})$	11.1736 ± 0.0015	11.18(9) ± 0.005[a]
		11.18 ± 0.01[b,c]
		11.190 ± 0.003[d]
		11.174 ± 0.003[e]
$OCS^+(^2\Pi_{1/2})$	11.2207 ± 0.0015	11.23(3) ± 0.005[a]
		11.22 ± 0.01[b,c]
		11.235 ± 0.003[d]
		11.220 ± 0.003[e]
$(OCS)_2^+$	10.456 ± 0.026	---
$(OCS)_2^+$	10.408 ± 0.026	---
$(OCS \cdot CS_2)^+$	9.858 ± 0.024	---
	Vibrational Frequency ν_1 (cm^{-1})	
$CS_2^+(^2\Pi_{3/2})$	620 ± 24	650 ± 50[a]
		610[b]

[a] Ref. 10.

[b] Ref. 7.

[c] Ref. 9.

[d] Ref. 12.

[e] Ref. 8.

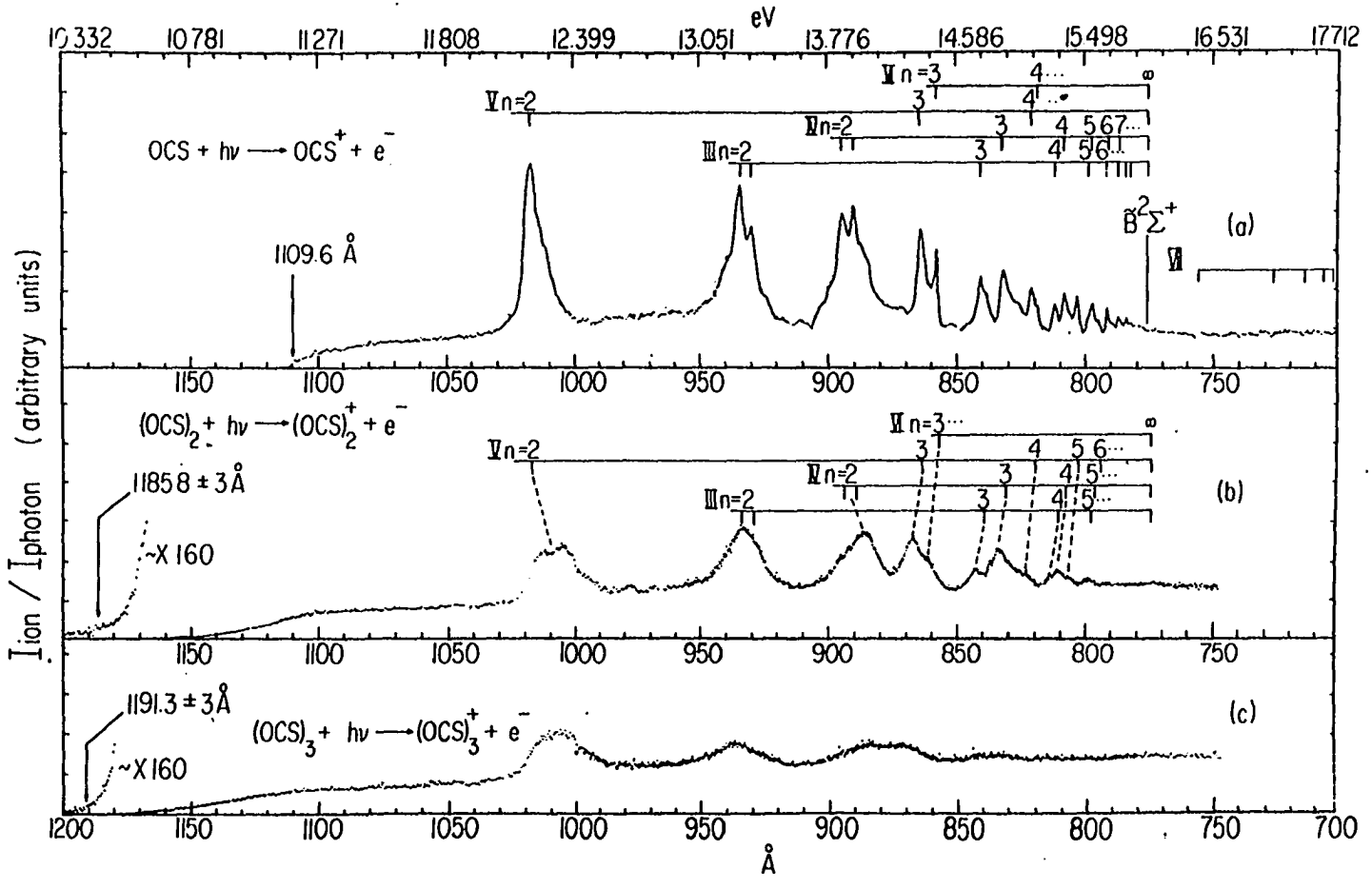

Figure 2. PIE curves for (a) OCS^+, (b) $(OCS)_2^+$, and (c) $(OCS)_3^+$ in the region 750-1200 Å

PIE curve published recently by Eland and Berkowitz (14). The PIE curves for OCS^+, $(OCS)_2^+$ and $(OCS)_3^+$ are arbitrarily normalized at a structureless region (∿1050 Å).

From the observed IE (10.456 ± 0.026 eV) for $(OCS)_2$ and the estimated binding energy (0.029 eV) (15) for $(OCS)_2$, a binding energy of 0.75 ± 0.04 eV (17.2 ± 1 kcal/mol) is deduced for $(OCS)_2^+$. Within the uncertainty of this experiment, this value is found to be equal to the binding energy (0.76 ± 0.04 eV) for $(CS_2)_2^+$ determined in a previous experiment (2). By assuming the binding energy of $(OCS)_2$ with OCS to be the same as in $(OCS)_2$ and using the measured IE (10.408 ± 0.026 eV) for $(OCS)_3$, the energy released by adding a carbonyl sulfide molecule to a carbonyl sulfide dimer ion is found to be only ∿0.07 eV.

Similar to previous observations in the PIE curves for $(CS_2)_2^+$ and $(CS_2)_3^+$, intensities of the autoionization peaks resolved in the PIE curves for $(OCS)_2^+$ and $(OCS)_3^+$ are greatly reduced. This is believed to be due in part to the dissociation of the dimeric ions resulting from autoionization. The peak positions of these autoionization features are also found to be shifted with respect to those in the monomer spectrum. Positions of the Rydberg series III, IV, V and VI of OCS, designated $E_1^*(n)$ in this study, are in excellent agreement with previous measurements (14,16,17). These Rydberg series have recently been assigned (14) as npσ(III), ndπ(V), and nsσ(VI) with quantum defects equal to 0.65, 0.12 and 0.05, respectively. However, since the lowest member of series V at 1015.6 Å (18) was observed, Delwiche et al. (8) have interpreted this series as an nsσ-series with a quantum defect,

$\delta = 1.12$ instead of $nd\pi$ with $\delta = 0.12$. In addition, they suggested that the series labeled $ns\sigma$(VI) should be labeled $nd\pi$. The nature of series IV is not clear. According to its quantum defect 0.48, this series is consistent with an $nd\sigma$ or an np series (19).

The peak positions of the autoionization resonances observed in the PIE curve for $(OCS)_2^+$, $E_2^*(n)$, are listed and compared with $E_1^*(n)$ in Table 3. Mulliken (20) points out that the value for the radius (r_n) of a Rydberg orbital at which the radial density is maximal is directly proportional to $(n^*)^2$, and can be approximated as $(n^*)^2 a_o$, where n^* and a_o are the effective principal quantum number and the Bohr radius, respectively. This is taken to be an approximation of the size of a Rydberg orbital with an effective principal quantum number n^*. The computed values for r_n are thus included in Table 3. The shifts in energy of Rydberg transitions observed in the dimer are related to the sizes of the Rydberg orbitals as well as the size and geometry of the neutral dimer. Neither the geometry of the carbonyl sulfide dimer nor the crystal structure of OCS are known. Since the Lennard-Jones diameter of OCS is approximately 4.1 Å (15), it is reasonable to assume that the intermolecular distance in $(OCS)_2$ is $\sim$4 Å. According to the analysis shown in Table 3, the Rydberg states having radii (r_n) larger than 4 Å are all found to be red-shifted. This observation is consistent with the expectation that when the size of the Rydberg orbital becomes sufficiently large and the electron density becomes sufficiently diffuse, the short-range repulsion arising from the exchange force, which is operative upon the overlap of the interacting charge distributions, will be

Table 3. Potential energy of OCS^* (III, IV, V or VI, n)-OCS at the equilibrium nuclear configuration of $(OCS)_2$

OCS Rydberg Series[a] (eV)		n^{*}[b]	r_R[c] (Å)	$E_1^*(n)$[d] (eV)	$E_2^*(n)$[e] (eV)	$\Delta E(n)$[f] (eV)	$D^*(n)$[g] (eV)
III(npσ)							
n = 2	13.297 (932.4 Å)	2.19	2.5	13.299 (932.3 Å)	13.303 (932 Å)		
	13.365 (927.7 Å)			13.363 (927.8 Å)			
3	14.794 (838.1 Å)	3.28	5.7	14.790 (838.3 Å)	14.729 (841.8 Å)	-0.061	-0.090
4	15.316 (809.5 Å)	4.31	9.8	15.311 (809.8 Å)	15.245 (813.3 Å)	-0.066	-0.095
IV(npσ?/ndσ?)							
n = 2	13.893 (892.4 Å)	2.52	3.4	13.895 (892.3 Å)	14.013 (884.8 Å)	+0.083[h]	+0.054
	13.965 (877.8 Å)			13.965 (887.8 Å)			
3	14.943 (829.7 Å)	3.51	6.5	14.942 (829.8 Å)	14.879 (833.3 Å)	-0.063	-0.092
4	15.377 (806.3 Å)	4.55	11.0	15.377 (806.3 Å)	15.307 (810.0 Å)	-0.070	-0.099
5	15.594 (795.1 Å)	5.50	16.0	15.594 (795.1 Å)	15.527 (798.5 Å)	-0.067	-0.096

V(ndπ or nsσ)							
n = 2		1.88	1.9	12.208 (1005.6 Å)	12.301 (1007.9 Å)	+0.093	+0.064
3	14.398 (861.1 Å)	2.85	4.3	14.388 (861.7 Å)	14.315 (866.1 Å)	-0.073	-0.102
4	15.155 (818.1 Å)	3.93	8.2	15.150 (818.4 Å)	15.078 (822.3 Å)	-0.072	-0.101
VI(nsσ or ndπ)							
n = 3	14.503 (854.9 Å)	2.96	4.6	14.494 (855.4 Å)	14.412 (860.3 Å)	-0.082	-0.111

[a]Ref. 17.

[b]n represents the nominal principal quantum number defined by Eqs. (11)-(14) of Ref. 17.

[c]$r_n = n^{*2}a_o$, where a_o is the Bohr radius.

[d]Autoionization peak observed in the PIE curve for OCS^+.

[e]This value is interpreted as the energy difference between the potential energy curve of $(OCS)_2$ and $OCS^*(n) \cdot OCS$ at the equilibrium geometry of $(OCS)_2$. Because of the relatively broad structure observed in the PIE curve for $(OCS)_2^+$, the accuracy of this value is ±1 Å.

[f]$\Delta E(n) = E_2^*(n) - E_1^*(n)$.

[g]The potential energy of OCS^*(III, IV, V or VI, n) · OCS at the equilibrium configuration of OCS.

[h]This is the average value of $E_2^*(n) - E_1^*(n)$ for the doublet of the member series IV, n = 2.

less important. Furthermore, as the shielding of the ion core by the Rydberg electron becomes less effective, charge-multipole attractive interactions and chemical forces will play more important roles in the bonding of the excited dimer $OCS^*(n) \cdot OCS$.

The red-shifts in energy of these Rydberg transitions in the dimer simply indicate that the potential energy, $D^*(n)$, of OCS^*(III, IV, V or VI, n) $\cdot$ OCS at the equilibrium configuration of $(OCS)_2$ is larger than the binding energy of the neutral carbonyl sulfide dimer. When the size of the Rydberg orbitals are smaller than the intermolecular distance of the dimer, the Rydberg electrons in these low lying Rydberg orbitals may still be relatively localized and the exchange repulsive interaction will be the dominating force. As shown in Table 3, D^*(IV,n=2) and D^*(V,n=2) are repulsive in nature (21). The equilibrium intermolecular distances of these types of excited dimers are expected to be larger than that of the neutral dimer. For example, the equilibrium nuclear distances ($\sim$6 Å) (22,23) for $He^*(2^1S$ or $2^3S)$ + Ne derived from molecular beam scattering experiments are substantially larger than the value ($\sim$3.2 Å) (24) for He + Ne.

In a compressed gas cell, the shape of these Rydberg absorption bands will not only depend on the relative positions of the potential energy curves for the ground and the excited states, but also on the ground state pair distribution. Therefore, the VUV absorption bands corresponding to low lying Rydberg transitions will appear to broaden asymmetrically toward the blue. A strong statistical preference for a neighbor at the equilibrium nuclear geometry of the neutral van der

Waals dimer will give rise to a satellite absorption peak having an energy shift characteristic of the equilibrium nuclear configuration for the dimer. The above discussions also infer that the absorption bands of higher Rydberg transitions having more diffuse Rydberg orbitals would respond by broadening asymmetrically to the low energy side.

Contrary to the blue-shifts observed for series IV n = 2 and series V n = 2, the peak position for series III n = 2 found in the PIE curve for $(OCS)_2^+$ seems to coincide with that in the OCS^+ spectrum. This can be taken as evidence that the perturbation of series III n = 2 (an npσ orbital) in comparison to that of series V n = 2 (an nsσ or ndπ orbital) is small during the time the dimer is formed. Considering the orbital symmetries, the perturbation of an npσ Rydberg orbital would be maximized if the perturber approaches along the molecular axis of the absorber. Therefore, assuming the validity of the symmetry arguments, it is unlikely for $(OCS)_2$ to have a collinear configuration. Due to the nature of this method, this experiment cannot provide any specific structural parameters for $(OCS)_2$, however, the shifts observed for the Rydberg series of OCS in the $(OCS)_2^+$ spectrum would be consistent with a near side-by-side or dihedral geometry for $(OCS)_2$. The symmetry properties of series IV are unknown. If the carbonyl sulfide dimer indeed possesses a near side-by-side or dihedral bonding geometry, the blue shift observed for the member n = 2 of series IV is consistent with an npπ or ndσ assignment for series IV.

Figure 3 shows the PIE curve for $OCS \cdot CS_2$ in the region 730-1270 Å. The measured IE for the $OCS \cdot CS_2$ dimer is 9.858 ± 0.024 eV (1257.7 ±

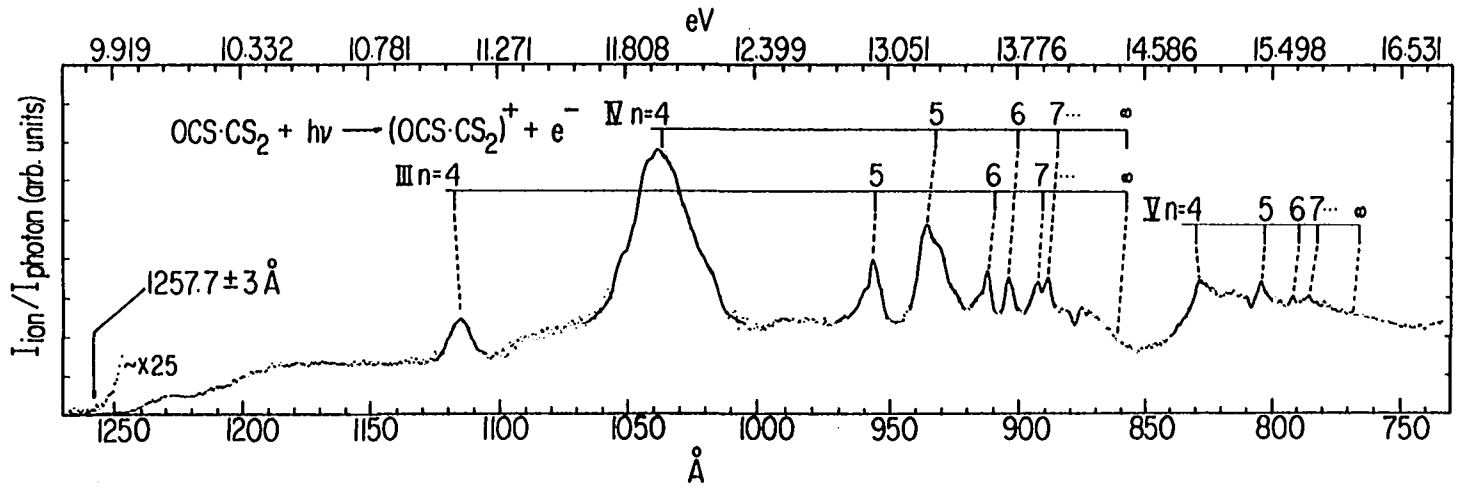

Figure 3. PIE curve for $(OCS \cdot CS_2)^+$ in the region 730-1270 Å

3 Å). From this, the IE for CS_2 (10.0685 ± 0.0020 eV) (2) and the estimated binding energy (0.039 eV) (25) between OCS and CS_2, the binding energy of CS_2^+ + OCS is deduced to be 0.25 ± 0.04 eV (5.8 ± 1 kcal/mol). This value is much smaller than the binding energies of $(OCS)_2^+$ and $(CS_2)_2^+$. The dissociation energies for symmetric dimeric ions are always found to be larger than the corresponding heterogeneous dimeric ions (26,27). This is believed to be due to stronger chemical bonding in symmetric dimeric ions than in asymmetric dimeric ions.

A comparison of the PIE curves for CS_2^+, $(CS_2)_2^+$, $(OCS)_2^+$ and $(OCS \cdot CS_2)^+$ leads us to conclude that the prominent structure observed in the $(OCS \cdot CS_2)^+$ spectrum originates mainly from CS_2. Although the absorption and the ionization coefficients of CS_2 (28) are similar in magnitude to those of OCS (16), the structure related to OCS is almost unrecognizable in the PIE curve for $(OCS \cdot CS_2)^+$. However, the anomalous increases in strength of the peaks at approximately 1040 Å, 930 Å and 940 Å etc., possibly have contributions from structures of both CS_2 and OCS. The $(OCS \cdot CS_2)^+$ ions observed at these peaks should consist of ions of the form $OCS^+ \cdot CS_2$ as well as $CS_2^+ \cdot OCS$. Attributing the autoionization features in the $(OCS \cdot CS_2)^+$ spectrum to CS_2, an analysis similar to that used above for the analysis of the $(OCS)_2^+$ spectrum has been carried out for the PIE curve for $(OCS \cdot CS_2)^+$. The result of this analysis is summarized in Table 4. The trends in the shifts in energy of Rydberg series III, IV and V of CS_2 are found to be almost identical to those found in $(CS_2)_2^+$, namely, the member n = 4 of series IV (an $np\pi$ series) appears to be unchanged in position whereas the member n = 4 of

Table 4. Potential energy of CS_2^* (III, IV or V, n)-OCS at the equilibrium nuclear configuration of $CS_2 \cdot OCS$

CS_2 Rydberg Series	$E_1^*(n)$[a] (eV)	n^*[b]	r_{6n} (Å)	$E_2^*(n)$[c] (eV)	$\Delta E(n)$[d] (eV)	$D^*(n)$[e] (eV)
III($ns\sigma$)						
n = 4	11.102 (1116.8 Å)	2.009	2.1	11.121 (1114.9 Å)	+0.019	-0.020
5	12.983 (955 Å)	3.025	4.8	12.962 (956.5 Å)	-0.021	-0.060
6	13.640 (909 Å)	4.037	8.6	13.602 (911.5 Å)	-0.038	-0.077
7	13.939 (889.5 Å)	5.056	13.5	13.900 (892 Å)	-0.039	-0.078
IV($np\pi$)						
n = 4	11.973 (1035.5 Å)	2.312	2.8	~11.973 (~1035.5 Å)		
5	13.303 (932 Å)	3.386	6.1	13.253 (935.5 Å)	-0.050	-0.089
6	13.776 (900 Å)	4.405	10.3	13.715 (904 Å)	-0.061	-0.100
7	14.018 (884.5 Å)	5.403	15.5	13.962 (888 Å)	-0.056	-0.095
V($np\sigma$)						
n = 4	14.943 (829.7 Å)	3.289	5.7	14.956 (829 Å)	+0.013	-0.026

5	15.431 Å (803.5 Å)	4.194	9.3	15.411 Å (804.5 Å)	-0.020	-0.059
6	15.694 (790 Å)	5.175	14.2	15.655 (792 Å)	-0.039	-0.078
7	15.841 (782.7 Å)	6.194	20.3	15.784 (785.5 Å)	-0.057	-0.096

[a]Autoionization peak observed in the PIE curve for CS_2^+ (Section II). The label of series III, IV and V follows the assignments of M. Larzilliere and N. Damany (29).

[b]M. Ogawa and H. C. Chang (30).

[c]This value is interpreted as the energy difference between the potential energy curves of $CS_2 \cdot OCS$ and $CS_2^*(n) \cdot OCS$ at the equilibrium geometry of $CS_2 \cdot OCS$.

[d]$\Delta E(n) = E_2^*(n) - E_1^*(n)$.

[e]The potential energy of $CS_2^*(III, IV \text{ or } V, n) \cdot OCS$ at the equilibrium nuclear configuration of $CS_2 \cdot OCS$.

series III (an npσ series) is blue-shifted. In addition, larger shifts for series III $n > 4$ than for series IV $n > 4$ relative to the positions in the monomer spectrum are observed. Using arguments similar to those discussed previously (2,3), these observations support a structure with OCS linked to CS_2 at an end sulfur. However, since the Rydberg series of OCS in the $(OCS \cdot CS_2)^+$ spectrum cannot be identified, this experiment does not provide any information concerning the orientation of OCS with respect to the molecular axis of CS_2. In other words, the molecular axis of OCS could be parallel with or perpendicular to that of CS_2. If the interpretations of the shifts of the Rydberg series of CS_2 and OCS observed in $(CS_2)_2$, $OCS \cdot CS_2$, and $(OCS)_2$ are correct, it is interesting that $OCS \cdot SCS$ and $SCS \cdot SCS$ are end-on complexes while $OCS \cdot OCS$ possesses a "side-by-side" geometry. The dipole moment of OCS and the large polarizability of CS_2 are probably responsible for these differences.

The first member $n = 4$ of series V is blue-shifted by ∿0.02 eV in the $(CS_2 \cdot OCS)^+$ spectrum as compared to a red-shift (∿0.06 eV) found in the PIE curve for $(CS_2)_2^+$. This can also be rationalized as being due to a stronger chemical interaction involved in $CS_2^*(n) \cdot CS_2$ than that in $CS_2^*(n) \cdot OCS$. Furthermore, a smooth change in the values of $D^*(n)$ for series IV (an npσ series) seems to be consistent with the suggested orientation of CS_2 with respect to OCS in the $OCS \cdot CS_2$ dimer.

Since the arguments used in Refs. 2 and 3 and in this section regarding the relation between red or blue shifting of Rydberg peaks, and molecular geometry completely neglect the possible effects of interaction of the Rydberg orbital with low-lying empty molecular orbitals of

the partner, the symmetry picture must be considered to be a crude one. Interactions of this nature, which would be symmetry selective and geometry dependent, are expected to play some role in $(CS_2)_2$ and $(OCS)_2$. Taking these interactions into account, the interpretations of wavelength shifts could be quite different from those discussed here and in Refs. 2 and 3. Therefore, the conclusions derived from the simple symmetry arguments must be subject to further examination. Even if the symmetry arguments and the assignments of series to particular orbital symmetries are completely valid, the geometry predictions obtained from photoionization studies are only qualitative. Recent calculations (31, 32) favor the staggered parallel configuration for the carbon dioxide dimer. If $(CS_2)_2$ also possesses a staggered parallel structure having a larger molecular distance as well as a smaller angle between the molecular axis of the carbon disulfide molecules and the intermolecular axis of $(CS_2)_2$ in comparison to those of $(CO_2)_2$, such that the perturbation of an nsσ orbital is larger than that of an npπ orbital with a similar Rydberg radius in size, the observations of the shifts for the Rydberg series of CS_2 in the $(CS_2)_2^+$ spectrum should still be considered as consistent with this dimer geometry.

In summary, this study has allowed us to determine the IEs for the $\tilde{X}^2\Pi_{3/2}$ and $^2\Pi_{1/2}$ states of OCS with higher accuracy. The stabilities of $(OCS)_2^+$, $(OCS)_3^+$ and $CS_2^+ \cdot OCS$ have been determined for the first time. By measuring the energy shifts of the Rydberg transitions in $(OCS)_2$, $CS_2 \cdot OCS$ and $(CS_2)_2$, a qualitative understanding of how the energy shifts of Rydberg transitions in the dimer relate to the nature of the

Rydberg orbital, the geometry of the dimer as well as the relative sizes of the dimer and the Rydberg orbital, has been developed. Possible problems of this simple picture have also been discussed.

REFERENCES

1. A. E. Douglas, in Chemical Spectroscopy and Photochemistry in the Vacuum-Ultraviolet, edited by C. Sandorfy, P. J. Ausloos and M. B. Robin (Reidel, Boston, 1973), NATO-Advanced Study Institutes series C, Vol. 8, p. 113.

2. See Section II.

3. W. M. Trott, N. C. Blais and E. A. Walters, J. Chem. Phys. 71, 1692 (1979).

4. M. B. Robin and N. A. Kuebler, J. Mol. Spectrosc. 33, 274 (1970).

5. O. Schnepp and K. Dressler, J. Chem. Phys. 33, 49 (1960).

6. K. M. Monahan and W. C. Walker, J. Chem. Phys. 63, 5126 (1975).

7. F. M. Matsunaga and K. Watanabe, J. Chem. Phys. 46, 4457 (1967).

8. J. Delwiche, M. J. Hubin-Franskin, G. Caprace, P. Natalis and D. Roy, J. Electron Spectrosc. Relat. Phenom. 21, 205 (1980).

9. V. H. Dibeler and J. A. Walker, J. Opt. Soc. Am. 57, 1007 (1967).

10. C. R. Brundle and D. W. Turner, Int. J. Mass Spectrom. Ion Phys. 2, 195 (1969).

11. D. C. Frost, S. T. Lee and C. A. McDowell, J. Chem. Phys. 59, 5484 (1973).

12. R. Frey, B. Gotchev, W. B. Peatman, H. Pollak and E. W. Schlag, Int. J. Mass Spectrom. Ion Phys. 26, 137 (1978).

13. S. Leach, J. Chim. Phys. 61, 1493 (1964).

14. J. H. D. Eland and J. Berkowitz, J. Chem. Phys. 70, 5151 (1979).

15. J. O. Hirschfelder, C. F. Curtiss and R. B. Bird, Molecular Theory of Gases and Liquids, (Wiley, New York, 1964).

16. G. R. Cook and M. Ogawa, J. Chem. Phys. 51, 647 (1969).

17. Y. Tanaka, A. S. Jursa and F. J. LeBlanc, J. Chem. Phys. 32, 1205 (1960).

18. A value of 1015.4 Å is given in J. Delwiche, M. J. Hubin-Franskin, P.-M. Guyon and I. Nenner, J. Chem. Phys. 74, 4219 (1981)

19. E. Lindholm. Ark. Fys. 40, 97 (1969).

20. R. S. Mulliken, J. Am. Chem. Soc. 86, 3183 (1964).

21. In these cases, the formation of $OCS^+ \cdot OCS$ from $OCS^*(n) \cdot OCS$ will be in competition with the direct dissociation process $OCS^*(n) \cdot OCS \rightarrow OCS^*(n) + OCS$.

22. H. Haberland, P. Oesterlin and K. Schmidt, Sixth Symposium on Molecular Beams, (Amsterdam, 1977).

23. P. E. Siska and T. Fukuyama, Tenth International Conference on the Physics of Electronic and Atomic Collisions, Abstracts of Papers, (Paris, France, 1977), p. 552.

24. C. H. Chen, P. E. Siska and Y. T. Lee, J. Chem. Phys. 59, 601 (1973).

25. The binding energy for $OCS \cdot CS_2$ is estimated to be $[D((CS_2)_2) \cdot D((OCS)_2)]^{1/2}$, where $D((CS_2)_2)$ and $D((OCS)_2)$ represent the binding energies of $(CS_2)_2$ and $(OCS)_2$, respectively.

26. C. Y. Ng, D. J. Trevor, B. H. Mahan and Y. T. Lee, J. Chem. Phys. 66, 446 (1977).

27. C. Y. Ng, P. W. Tiedemann, B. H. Mahan and Y. T. Lee, J. Chem. Phys. 66, 5737 (1977).

28. G. R. Cook and M. Ogawa, J. Chem. Phys. 51, 2419 (1969).

29. M. Larzilliere and N. Damany, Can. J. Phys. 56, 1150 (1978).

30. M. Ogawa and H. C. Chang, Can. J. Phys. 48, 2455 (1970).

31. A. Koide and T. Kihara, Chem. Phys. 5, 34 (1974).

32. N. Brigot, S. Odiot, S. H. Walmsley and J. L. Whitten, Chem. Phys. Lett. 49, 157 (1977).

SECTION V.

A HIGH RESOLUTION PHOTOIONIZATION STUDY OF ACETYLENE

INTRODUCTION

In a vacuum ultraviolet absorption study of acetylene, two Rydberg series below the ionization potential having quantum defects, δ, of 0.5 and 0.95 which converge to the limits of 92076 and 91950 cm^{-1}, respectively, were identified by Price (1). The 126 cm^{-1} difference of these limits was attributed to the spin orbit splitting of the $\tilde{X}^2\Pi_u$ state of the acetylene ion. Another absorption study (2) and a theoretical investigation (3) supported this interpretation. However, in a more recent VUV absorption study, Jungen (4) re-examined the Rydberg spectrum of acetylene and found three strong Rydberg series that can be satisfactorily assigned using 91950 cm^{-1} as the common series limit.

Early photoionization studies (5,6) of C_2H_2 and C_2D_2 suggested a simple step structure corresponding to excitation to the ground, first and second ν_2 vibrationally excited states of $C_2H_2^+$ near the threshold and evidence of weak autoionization structure superimposed on the steps was reported in subsequent studies (7,8). By cooling acetylene in a low pressure gas cell to 118K, which corresponds to an average rotational energy of $\sim$0.015 eV, Dibeler and Walker (9) have observed autoionizing Rydberg series converging to the vibrationally excited states of the $\tilde{X}^2\Pi_u$ state of $C_2H_2^+$.

Using the same δ values as those reported by Price (1), and the average vibrational interval of 0.227 eV for ν_2 obtained from the photoelectron spectrum of C_2H_2 (10), they have calculated members of the two Rydberg series which converge to each of the three vibrational states of $C_2H_2^+$ and compared them with autoionizing features resolved in the

photoionization efficiency curve for $C_2H_2^+$. Good correlation was found for members of the series having $\delta = 0.95$, whereas members of the series characterized by $\delta = 0.50$ were found to be either too weak to be observed, or unresolved. The analysis of the PIE curve for $C_2H_2^+$ also revealed a new Rydberg series with $\delta = 0.35$. Nevertheless, as a result of the limitation in resolution of their experiment, these Rydberg series have not been unequivocally identified. In order to examine these autoionizing Rydberg series in more detail, it is necessary to perform a higher resolution photoionization experiment of C_2H_2.

EXPERIMENTAL

The C_2H_2 molecular beam was produced by supersonic expansion through a 120 μm diameter nozzle orifice at a nozzle temperature of ∿290K and a stagnation pressure of ∿520 Torr. The acetylene was obtained from Matheson with a quoted purity of ≥99.6%. The argon continuum was used as the light source and the optical resolution was 0.14 Å (FWHM). Typical counting times are 6 seconds and ion counts accumulated at each point are approximately 8,000 counts. The PIE data for $C_2H_2^+$ in the region 1059-1090 Å are plotted in Fig. 1. Due to the extremely low light intensity in the region ∿1065.5-1068 Å, the data points have been omitted.

RESULTS AND DISCUSSION

As shown in Fig. 1, the PIE curve decreases rapidly in a wavelength interval of ∿0.55 Å, then tails away gradually toward lower energy. Based on the expectation that the vibrational relaxation is inefficient under the employed nozzle conditions, the tailing structure probably arises from vibrational hot bands. Taking the energy corresponding to the midpoint of the rapidly rising region as the ionization energy of C_2H_2, the resulting value of 11.396 ± 0.003 eV (1088.0 ± 0.3 Å) is in excellent agreement with previous photoionization measurements (9,11). The relative Franck-Condon factors for the 0,0 and 0,1 transitions are measured to be 1.00 and 0.33, respectively, which are also consistent with values obtained in previous photoionization (9) and photoelectron (10) studies.

The general profile of the PIE curve is similar to that obtained by Dibeler and Walker (9). Since the resolution is more than a factor of three higher than that used in the previous experiment, the autoionization structure superimposed on the vibrational steps is much better resolved. Attempts were made to assign the observed autoionization features by using quantum defects similar to those reported in Refs 1, 4 and 5, and the average vibrational quantum of ν_2 for $C_2H_2^+$. The possibility of having two converging limits separated by approximately 50 cm^{-1} was also considered in the analysis (12). The best fit can be represented by the two Rydberg series

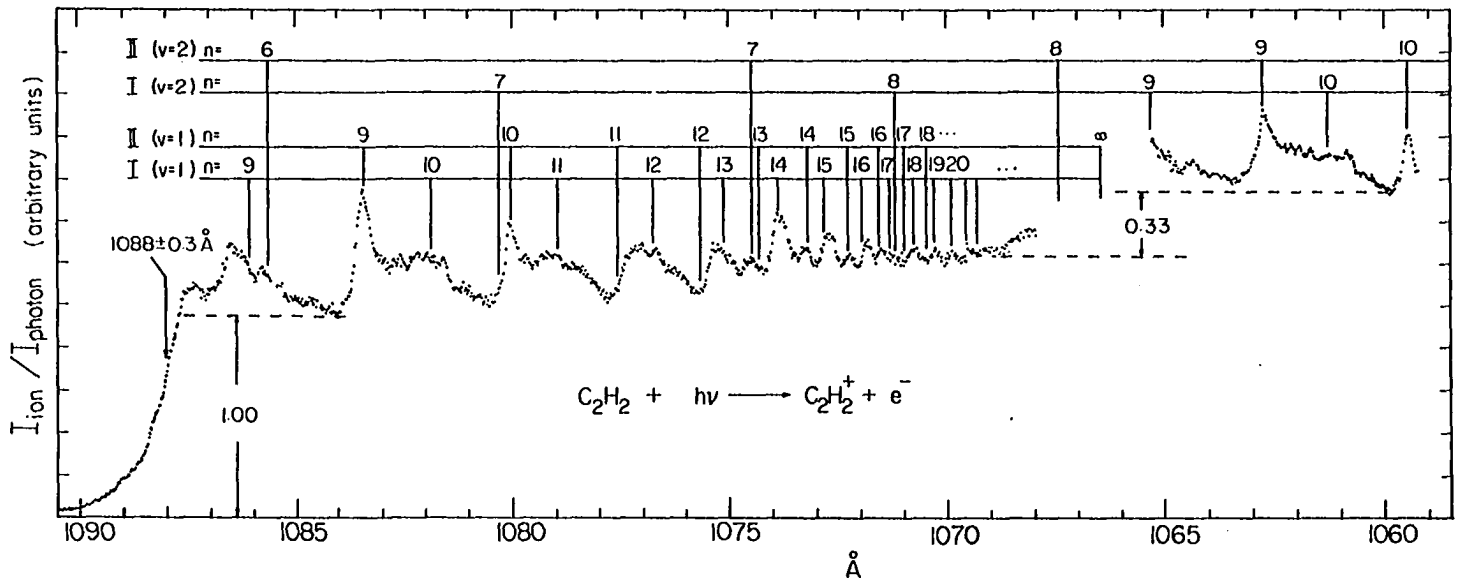

Figure 1. Photoionization efficiency curve for $C_2H_2^+$ obtained using a wavelength resolution of 0.14 Å (FWHM)

$$\nu_n = 93{,}770 - \frac{R}{(n-0.95)^2} \text{ cm}^{-1}, \quad \text{series I } (v_2 = 1)$$

$$\nu_n = 93{,}770 - \frac{R}{(n-0.36)^2} \text{ cm}^{-1}, \quad \text{series II } (v_2 = 1)$$

where R and n are the Rydberg constant and the principal quantum number, respectively. Similar to the previous observation (9), the members of the Rydberg series characterized by $\delta = 0.50$ which are identified below the IE of C_2H_2 are not observed here. Using the positions of the peaks at 94,093 cm^{-1} (1062.82 Å) and 94,384 cm^{-1} (1059.50 Å), and $\delta = 0.36$, the converging limit for the Rydberg series II ($v_2 = 2$) is calculated to be 95,563 cm^{-1}. The positions of the observed autoionization peaks (ν_{obs}) are listed in Table 1 and compared with the calculated values for members of series I ($v_2 = 1$), II ($v_2 = 1$), I ($v_2 = 2$), and II ($v_2 = 2$). It is interesting to note that the n = 11 and 12 members of series II ($v_2 = 1$) are missing from the PIE spectrum. According to these assignments, the uncertainty of the IE for the $\tilde{X}^2\Pi_u$ ($v_2 = 1$) state of $C_2H_2^+$ is estimated to be ±12 cm^{-1}. The resulting values for the vibrational spacings ΔE_v = 0-1 and 1-2 are 1860 ± 27 cm^{-1} and 1793 cm^{-1}, respectively, which are consistent with the average ν_2 of $C_2H_2^+$ derived from the photoelectron spectrum of C_2H_2. The result of this analysis suggests that the strong autoionizing features originate mainly from series I and that the $\Delta v = -1$ processes are favored in the autoionization of $C_2H_2^*(n,v)$ in this wavelength region.

Table 1. Possible assignments for autoionization peaks observed in the region 1059-1090 Å

ν_{obs} (cm^{-1})	ν_{calc} [nl(v) or nll(v)]
92051 (1086.35 Å)[a]	92077 [9l(1)]
92102 (1085.75 Å)	92113 [6ll(2)]
92298 (1083.45 Å)	92300 [9ll(1)]
92421 (1082.00 Å)[a]	92430 [10l(1)]
92588 (1080.05 Å)	92589 [10ll(1)]
92678 (1079.00 Å)[a]	02684 [11l(1)]
	92801 [1111(1)]
92868 (1076.80 Å)	91871 [12l(1)]
	92960 [12ll(1)]
93010 (1075.15 Å)[a]	93014 [13l(1)]
93071 (1074.45 Å)	93074 [7ll(2)]
	93083 [13ll(1)]
93127 (1073.80 Å)	93126 [14l(1)]
93175 (1073.25 Å)	93180 [14ll(1)]
93223 (1072.70 Å)	93214 [15l(1)]
93262 (1072.25 Å)	93258 [15ll(1)]
93297 (1071.85 Å)	93286 [16l(1)]
93336 (1071.40 Å)	93321 [16ll(1)]
	93344 [17l(1)]
	93355 [8l(2)]
	93374 [17ll(1)]
93392 (1070.75 Å)	93393 [18l(1)]
	93417 [18ll(1)]
93436 (1070.25 Å)	93433 [19l(1)]
	93454 [19ll(1)]

[a]Estimated centers of the autoionizing bands.

Table 1. Continued

ν_{obs} (cm^{-1})	ν_{calc} [nI(v) or nII(v)]
93471 (1069.85 Å)	93468 [20I(1)]
	03683 [8II(2)]
	93870 [9I(2)]
94089 (1062.82 Å)	94093 [9II(2)]
94224 (1061.30 Å)	94223 [10I(2)]
94384 (1059.50 Å)	94382 [10II(2)]

REFERENCES

1. W. C. Price, Phys. Rev. 47, 444 (1935).

2. P. G. Wilkinson, J. Mol. Spectrosc. 2, 387 (1958).

3. E. W. Greene, Jr., J. Barnard and A. B. F. Duncan, J. Chem. Phys. 54, 71 (1971).

4. M. Jungen, Chem. Phys. 2, 367 (1973).

5. V. H. Dibeler and R. M. Reese, J. Res. Nat. Bur. Stand. A 68, 409 (1964).

6. R. Botter, V. H. Dibeler, J. A. Walker and H. M. Rosenstock, J. Chem. Phys. 44, 1271 (1966).

7. B. Brehm, Z. Naturforsch. 21a, 196 (1966).

8. I. Omura, T. Kaneko, Y. Yamada and K. Tanaka, J. Phys. Soc. Jpn. 27, 178 (1969).

9. V. H. Dibeler and J. A. Walker, Int. J. Mass Spectrom. Ion Phys. 11, 49 (1973).

10. C. Baker and D. W. Turner, Proc. R. Soc. (London) Ser. A 308, 19 (1968).

11. V. H. Dibeler, J. A. Walker and K. E. McCulloh, J. Chem. Phys. 59, 2264 (1973).

12. It is predicted that the $\tilde{X}^2\Pi_u$ state of $C_2H_2^+$ might have a splitting of $\sim$50 cm^{-1}. See G. Herzberg, Molecular Spectra and Molecular Structure III. Electronic Spectra and Electronic Structure of Polyatomic Molecules, (Van Nostrand Reinhold Co., New York, 1966), p. 518.

SECTION VI.

A STUDY OF THE UNIMOLECULAR DECOMPOSITION OF THE $(C_2H_2)_2^+$ COMPLEX

INTRODUCTION

The ion-molecule reactions of acetylene

$$C_2H_2^+ + C_2H_2 \rightarrow C_4H_3^+ + H \quad (1)$$

$$\rightarrow C_4H_2^+ + H_2 \quad (2)$$

$$\rightarrow C_4H_2^+ + 2H \quad (3)$$

$$\rightarrow C_2H_3^+ + C_2H \quad (4)$$

have been the subject of numerous mass spectrometric investigations in the last three decades (1-22). These studies show that $C_4H_3^+$ and $C_4H_2^+$ are the major product ions when the $C_2H_2^+$ reactant ions are formed by electron ionization and photoionization in the energy range 11.4-20 eV. There is general agreement that the ratio of the reaction rates for reaction 2 to reaction 1 with $C_2H_2^+$ prepared in vibrational levels of the $\tilde{X}^2\Pi_u$ ground state is approximately 0.5 (5-11,19-21), and that there exists an excited molecular state of $C_2H_2^+$ at about 16 eV which strongly favors the formation of the $C_4H_2^+$ ion (6,7,11,20,21). The observation of considerable hydrogen-deuterium mixing of the C_4 product ions when the reactions are studied in C_2H_2-C_2D_2 mixtures (5,6) or when $C_2H_2^+$ is reacted with C_2D_2 in a tandem mass spectrometer (7) provides evidence that these reactions involve the formation of long-lived or intimately mixed reaction complexes.

Since the $C_4H_2^+$ ion can also be produced by the reaction

$$C_2H^+ + C_2H_2 \rightarrow C_4H_2^+ + H \quad (5)$$

and the appearance energy (AE) of C_2H^+ from C_2H_2 is 16.72 eV (23) which is close to the ionization energy (IE $\simeq$ 16.36 eV) (24-27) of the first excited state ($\tilde{A}^2\Sigma_g^+$) of $C_2H_2^+$, previous studies were unable to assess the relative contributions to the formation of $C_4H_2^+$ from reactions 2, 3 and 5. Furthermore, due to the fact that reactions 1 and 2 are exothermic by $\sim$12.4 and $\sim$23.5 kcal/mol, respectively, information pertaining to the energetics of these ion-molecule processes such as AEs cannot be obtained by conventional ion-molecule reaction studies.

This report presents the results and the analysis of a study of the unimolecular decomposition of acetylene dimer ions which were prepared by the direct photoionization and/or the autoionization processes

$$(C_2H_2)_2 + h\nu \rightarrow (C_2H_2)_2^+ + e^- \qquad (6)$$

$$\rightarrow C_2H_2^*(n,v) \cdot C_2H_2 \rightarrow C_2H_2^+ \cdot C_2H_2 + e^- \quad . \qquad (7)$$

Although the possibility of the direct fragmentation of excited Rydberg dimers $C_2H_2^*(n,v) \cdot C_2H_2$ to form $C_4H_3^+$, $C_4H_2^+$, etc. cannot be excluded, from the consideration that the autoionization lifetime is in general much shorter than the time needed for molecular rearrangements, it is most likely that reaction 7 will precede the fragmentation processes. The novel aspects of the photoionization of van der Waals dimers in the study of internally excited atomic and molecular species have been discussed in detail previously (28-30). Since the binding energy between $C_2H_2^+$ and C_2H_2 is 22.5 $\pm$ 1 kcal/mol (31), which is greater than the exothermicity of reaction 1 and approximately equal to that of reaction 2, it is possible to determine the AE's of $C_4H_3^+$ and $C_4H_2^+$ and, thus, the

highest potential energy barriers for the $C_4H_3^+ + H$ and the $C_4H_2^+ + H_2$ channels along the reaction coordinate. A similar photoionization study on $(C_2H_4)_2$ which demonstrates this idea has been reported (30,32). Because of the higher energy resolution achieved in this experiment compared to previous investigations by the electron ionization and charge transfer methods, photoionization efficiency (PIE) data for $C_4H_2^+$ and $C_4H_3^+$ from $(C_2H_2)_2$ obtained in the energy range ~10.5-20 eV have provided more detailed information concerning the roles of the vibrationally and electronically excited states in reactions 1, 2 and 3 without the influence of reaction 5.

The conventional mass spectrometric technique used in the kinetic study of ion-molecule reactions does not allow for a clear distinction between the collision complex mechanism and the simple consecutive reaction mechanism. There is strong evidence that the $(C_2H_2)_3^+$ ions rearrange to some stable $C_6H_6^+$ isomers prior to dissociation (31). Thus, this study should also shed light on the collision complex mechanism of the ion-molecule reactions of $C_2H_2^+ + C_2H_2$.

EXPERIMENTAL

The acetylene dimers were produced by supersonic expansion through a 120 μm diameter stainless steel nozzle at a nozzle temperature (T_0) of approximately 230K and a stagnation pressure (P_0) ≤ 350 Torr. Part of the data were obtained at $T_0 \approx 298$K and $P_0 \approx 1000$ Torr. Under these nozzle conditions, ions containing more than four carbon atoms could not be detected, indicating that the concentrations of higher clusters $(C_2H_2)_n$, $n > 2$, were negligible and C_2H_2 and $(C_2H_2)_2$ were the major constituents of the molecular beam. Since the acetylene beam was sampled in a collisionless environment, the observed fragment ions represent the primary fragments of $C_2H_2^+$ and $(C_2H_2)_2^+$. The acetylene was obtained from Matheson with a quoted purity of ≥99.6%.

All the data were obtained with an optical resolution of 1.4 Å (FWHM). Data points were taken typically at either 0.5 or 1 Å intervals. The standard deviations of PIE data for $C_2H_2^+$, $C_4H_2^+$, $C_4H_3^+$ and $(C_2H_2)_2^+$ are better than 10%. Each PIE curve was based on at least two scans, and the prominant structures in the spectra were found to be reproducible.

RESULTS AND DISCUSSION

Photoionization efficiency data obtained for $C_2H_2^+$, $C_4H_2^+$, $C_4H_3^+$ and $(C_2H_2)_2^+$ in the region 600-1200 Å are plotted in Figs. 1(a), (b), (c) and (d), respectively. Due to the low intensity of $C_2H_3^+$ and its coincidence in mass with $C^{12}C^{13}H_2^+$, the PIE curve for $C_2H_3^+$ could not be measured in this study. The PIE curve for $C_2H_2^+$ shown here in Fig. 1(a) is in excellent agreement with that reported by Botter et al. (33) and by Berkowitz (34). Although the structure other than that near the ionization threshold has not been thoroughly analyzed, it is quite obvious that the PIE spectrum of $C_2H_2^+$ in the region ~750-970 Å is dominated by autoionization features. The gradual decrease in PIE at energies greater than ~16.72 eV probably arises from the fragmentation of $C_2H_2^+$ to form $C_2H^+ + H$.

The general profiles of the PIE curves for $C_2H_2^+$, $C_4H_2^+$, $C_4H_3^+$ and $(C_2H_2)_2^+$ are quite similar except that the PIE spectrum for $C_4H_2^+$ exhibits an abrupt increase in the region around 760 Å instead of following the decreasing trend of other curves in the same region. This observation is consistent with features found in the ionization efficiency curves of $C_4H_2^+$ and $C_4H_3^+$ from reaction 1, 2 and 3 in gas cell studies of acetylene using the electron ionization method (7,11). Since the IE to the $\tilde{A}^2\Sigma_g^+$ state of $C_2H_2^+$ is ~16.36 eV (757 Å) (24-27), the attribution to the higher reactivity of the $\tilde{A}^2\Sigma_g^+$ state in the formation of $C_4H_2^+$ seems to be the obvious conclusion (6,7,11). However, a careful examination of the PIE curves for $C_4H_2^+$ and $C_4H_3^+$ in the region 650-850 Å reveals that the PIE for $C_4H_2^+$ actually starts to deviate

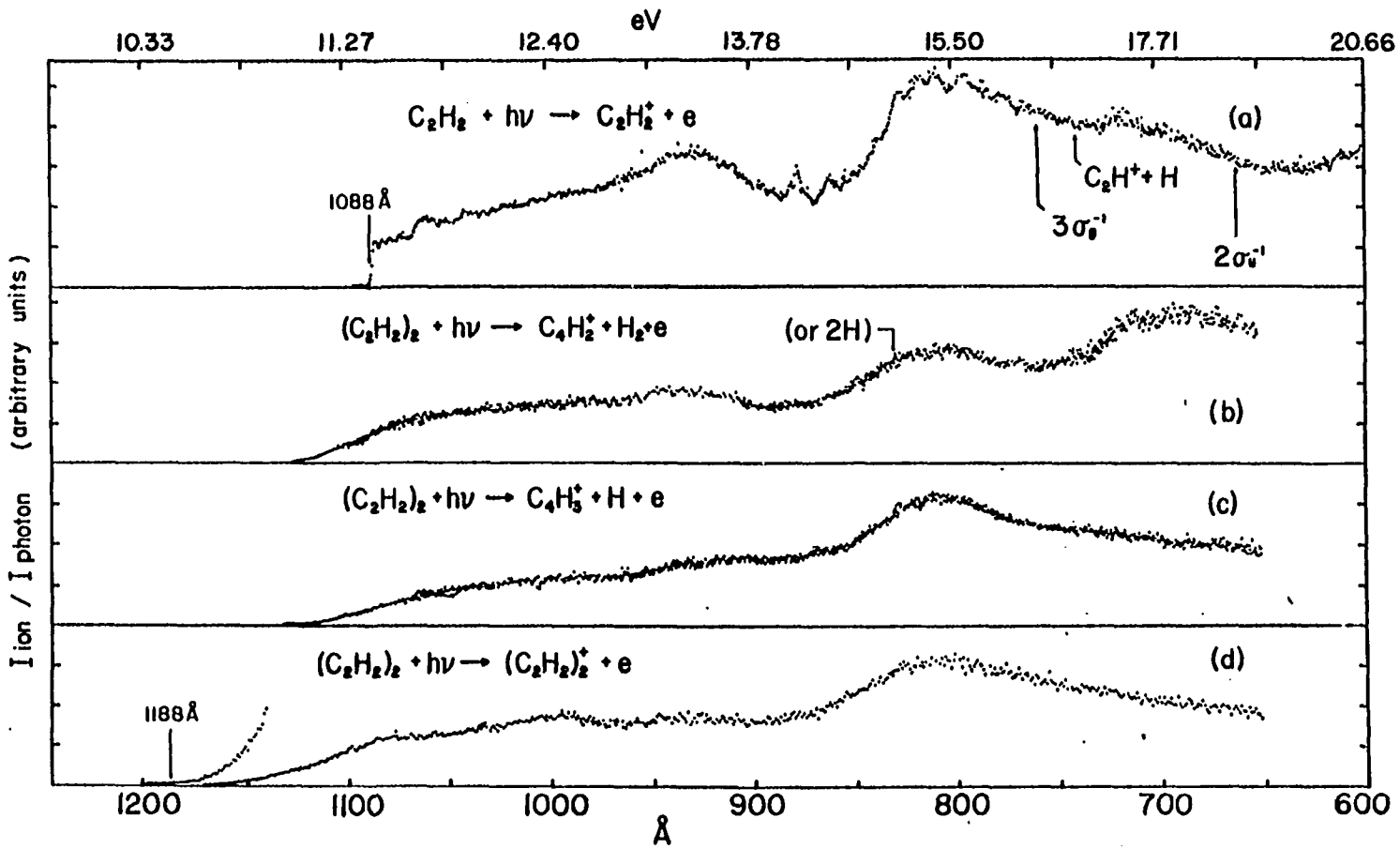

Figure 1. Photoionization efficiency curves for (a) $C_2H_2^+$, (b) $C_4H_2^+$, (c) $C_4H_3^+$ and (d) $(C_2H_2)_2^+$ in the region ~600 Å - 1200 Å. Experimental condition $P_0 \approx 350$ Torr, $T_0 \approx 230$K, wavelength resolution = 1.4 Å (FWHM)

gradually with respect to the PIE for $C_4H_3^+$ at energies well below the IE for the $\tilde{A}^2\Sigma_g^+$ state of $C_2H_2^+$.

According to known thermodynamical data (35-37) (see Table 1), the thermochemical threshold for reaction 3 is 14.90 eV and the expected onset for the formation of $C_4H_2^+ + 2H$ from $(C_2H_2)_2$ is 14.93 eV (830 Å), as indicated by an arrow in Fig. 1(b). Therefore, at photon energies above 14.93 eV, both the $C_4H_2^+ + H_2$ and the $C_4H_2^+ + 2H$ channels are energetically accessible.

In order to re-examine the role of the $\tilde{A}^2\Sigma_g^+$ state in the formation of $C_4H_2^+$ and to assess the relative contributions of reactions 2 and 3 to the increase in intensity for $C_4H_2^+$, the relationship between $I((C_2H_2)_2^+)$, $I(C_4H_2^+)$ and $I(C_4H_3^+)$, where $I((C_2H_2)_2^+)$, $I(C_4H_2^+)$ and $I(C_4H_3^+)$ represent the intensities for $(C_2H_2)_2^+$, $C_4H_2^+$ and $C_4H_3^+$, respectively, has been investigated. Figure 2 shows the relative abundances, $I(C_2H_2)_2^+/\Sigma$, $I(C_4H_2^+)/\Sigma$ and $I(C_4H_3^+)/\Sigma$ of $(C_2H_2)_2^+$, $C_4H_2^+$ and $C_4H_3^+$, respectively, in percentage as a function of the photon energy (38). Here, Σ is the sum of $I((C_2H_2)_2^+)$, $I(C_4H_3^+)$ and $I(C_4H_2^+)$. The relative abundance diagram is based on PIE data for various ions measured at wavelength intervals of 50 Å. As a result of a much shorter time span in obtaining these data in comparison with that needed for measurements of PIE data shown in Figs. 1(b), (c) and (d), the data plotted in Fig. 2 are believed to be less susceptible to minor experimental fluctuations and, thus, better represent the relative abundances of these ions. Despite the fact that the PIE data obtained here are not state-selected data, the relative abundance plots shown in Fig. 2 still display the significant features

Table 1. 298K heats of formation in kcal/mol of neutrals and ions[a]

Compound	Neutrals	Ions
$(C_2H_2)_2$	108 ± 0.2[b] (35,36)	348.9 ± 1 (31)
C_4H_4		276 ± 2 (50) 280 ± 2 (51) 285 ± 3 (53) 293.7 ± 0.5[c] (52) 294 ± 2[d] (52)
C_4H_3		307 (54)
C_4H_2		348 (37)
C_2H_2	54.34[b] (35) 54.19[b] (35)	317.2 (35)
H	52.10 (35)	

[a]The number in the parentheses are the references.

[b]Heat of formation at 0K.

[c]Heat of formation for the 1-buten-3-yne ion.

[d]Heat of formation for the butatriene ion.

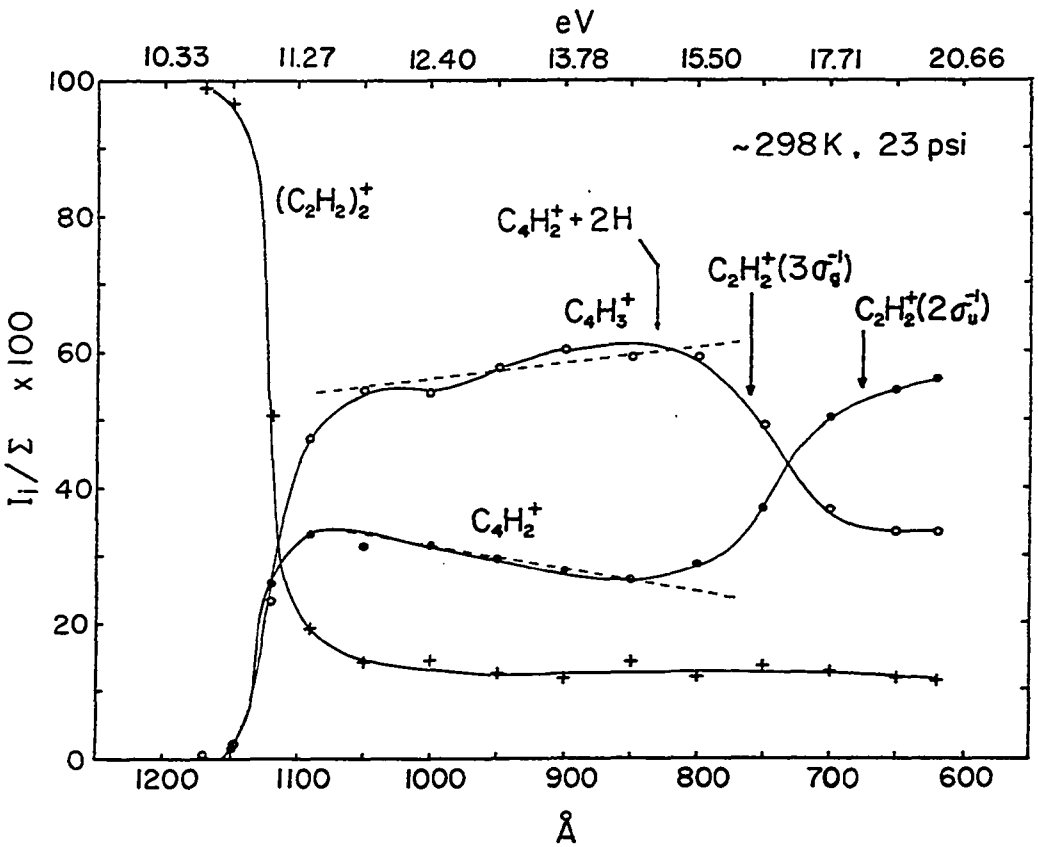

Figure 2. The variations of the relative abundances for $(C_2H_2)_2^+$, $C_4H_3^+$ and $C_4H_2^+$ as a function of the photon energy. Σ is the sum of $I((C_2H_2)_2^+)$, $I(C_4H_3^+)$ and $I(C_4H_2^+)$, where $I((C_2H_2)_2^+$, $I(C_4H_3^+)$ and $I(C_4H_2^+)$ represent the intensities of $(C_2H_2)_2^+$, $C_4H_3^+$ and $C_4H_2^+$, respectively

as anticipated in the unimolecular decomposition of $(C_2H_2)_2^+$ following the scheme:

$$(C_2H_2)_2^+ \rightarrow (C_4H_4^+)^* \rightarrow C_4H_3^+ + H \quad (7)$$

$$\rightarrow C_4H_2^+ + H_2 \quad (8)$$

$$\rightarrow C_4H_2^+ + 2H \quad . \quad (9)$$

The most apparent feature is the rapid decay of the relative abundance of $(C_2H_2)_2^+$ and the corresponding increase in the abundances for $C_4H_3^+$ and $C_4H_2^+$ after the onsets for $C_4H_3^+$ and $C_4H_2^+$. The $C_4H_3^+$ ion is the major product ion in the region ∿11.37-16.53 eV (750-1090 Å), whereas at energies above ∿16.98 eV, the $C_4H_2^+$ ion becomes the dominate species. The variations in the relative abundances of $C_4H_2^+$ and $C_4H_3^+$ clearly reflects the competitive nature of reactions 7, 8 and 9.

The ratio of $I(C_4H_2^+)$ to $I(C_4H_3^+)$ measured at different photon wavelengths is listed and compared with several previous measurements at specific ionization energies by photoionization (19) and electron ionization methods (5,7) in Table 2. Munson (5), and Futrell and Tiernan (7), using electrons as the ionization source, found that $I(C_4H_2^+)/I(C_4H_3^+) = 0.45$ at electron energies ≤15 eV. In a photoionization study of reactions of acetylene ions, Buttrill (19) found that the value of $I(C_4H_2^+/I(C_4H_3^+)$ decreases gradually from ∿0.50 to 0.42 with increasing photon energy in the wavelength region ∿1025-1090 Å. These values are in good agreement with the ratios observed here in the region 800-950 Å. In the region 1000-1090 Å, however, the values of

Table 2. The ratio of the intensity for $C_4H_2^+$ to that for $C_4H_3^+$ measured at different ionization photon wavelengths

	$I(C_4H_2^+)/I(C_4H_3^+)$[a]	
λ (Å)	This Work	Other Techniques
1120	1.07 ± 0.05	
1090	0.70 ± 0.02	0.49[b]
1050	0.58 ± 0.01	0.44[b]
1000	0.58 ± 0.03	
950	0.52 ± 0.02	
900	0.46 ± 0.01	
850	0.45 ± 0.01	0.44 ± 0.04[c], 0.45 ± 0.01[d]
800	0.48 ± 0.01	
750	0.76 ± 0.01	
700	1.37 ± 0.04	
650	1.61 ± 0.05	
620	1.67 ± 0.10	

[a] $I(C_4H_2^+)$ and $I(C_4H_3^+)$ represent the intensities of $C_4H_2^+$ and $C_4H_3^+$, respectively.

[b] Values obtained by scaling Fig. 1 of Ref. 19.

[c] Reference 5. Electron energy ≤15 eV (∿827 Å).

[d] Reference 7. Electron energy ≤15 eV (∿827 Å).

$I(C_4H_2^+)/I(C_4H_3^+)$ are greater than those reported previously. Due to the efficient rotational relaxation in the supersonic expansion and the rotational selection rules of the photoionization processes, total angular momenta associated with the $(C_2H_2)_2^+$ ions prepared by reactions 6 and 7 should be much smaller than collision-complexes formed by the reaction of $C_2H_2^+$ with C_2H_2 where the dominate force is the long-range ion-induced dipole interaction. Assuming the validity of the above arguments, the higher values of $I(C_4H_2^+)/I(C_4H_3^+)$ obtained here in comparison with the values of Buttrill (19) are contrary to the expectation based on the study of Meisels et al. concerning the angular momentum effects on ion-molecule reactions (39,40). Nevertheless, if reactions 1-4 involve both the direct and the collision-complex mechanisms, the higher values of $I(C_4H_2^+)/(C_4H_3^+)$ observed in this experiment can be interpreted as evidence that the formation of $C_4H_3^+ + H$ is more favorable by the direct than by the complex mechanisms.

Based on Franck-Condon factors for the excitation from the ground state of C_2H_2 to the $\tilde{X}^2\Pi_u$ state of $C_2H_2^+$ derived from the HeI photoelectron spectrum of C_2H_2 (24-27), one only expects a few vibrational levels (v_2 = 0, 1, 2 and 3) of the ground $\tilde{X}^2\Pi_u$ state to be excited with photon energies below the IE of the $\tilde{A}^2\Sigma_g^+$ state (~16.36 eV). However, higher vibrational levels of the $\tilde{X}^2\Pi_u$ state can be populated by autoionization processes. The $C_2H_2^+$ ion in the $\tilde{X}^2\Pi_u$ and the $\tilde{A}^2\Sigma_g^+$ states possess a linear and a bent structure, respectively (41). If autoionization takes place from Rydberg levels which converge to the $\tilde{A}^2\Sigma_g^+$ state into the $\tilde{X}^2\Pi_u$ state, the difference in geometry of these two states may cause highly

vibrationally excited $C_2H_2^+(\tilde{X}^2\Pi_u)$ ions to be formed. It was suggested that there is a quartet ionic state that lies below the $\tilde{A}^2\Sigma_g^+$ state which might provide a nonradiative pathway from the $\tilde{A}^2\Sigma_g^+$ state to the $\tilde{X}^2\Pi_u$ state (42). From the consideration of the change in the electron spin of an autoionization process, the $C_2H_2^+$ ions formed by autoionization are most likely to be in the $\tilde{X}^2\Pi_u$ state at energies below ~16.36 eV. Another mechanism which will lead to the formation of highly vibrationally excited $C_2H_2^+(\tilde{X}^2\Pi_u)$ ions is the "resonant" autoionization process (43). In a photoionization study of N_2O, Baer et al. (43) showed that approximately 10% of the autoionization results in N_2O^+ ions in the $X^2\Pi$ state with up to 3 eV of vibrational energy. Assuming autoionization of $C_2H_2^*(n,v)$ to be unperturbed by C_2H_2 in the dimer, it is reasonable to believe that the vibrational energy of $(C_2H_2)_2^+$ prepared by reactions 6 and 7 increases correspondingly with excitation photon energy.

One of the interesting features shown in Fig. 2 is the nearly linear increasing trend and the corresponding decreasing trend of the relative abundances for $C_4H_3^+$ and $C_4H_2^+$, respectively, in the region ~850-1090 Å. Buttrill (19) pointed out that according to a quasi-equilibrium theory treatment, fragmentation of the $(C_4H_4^+)^*$ reaction complex to $C_4H_2^+ + H_2$ necessarily involves formation of a "tight" activated complex having a low frequency factor. On the other hand, the formation of $C_4H_3^+ + H$ involves a relatively "loose" activated complex with a higher frequency factor. Since the fragmentation probability for a "loose" complex is expected to increase more rapidly with internal

energy than a "tight" complex, we conclude that this observation is in qualitative agreement with the prediction based on the quasi-equilibrium theory.

The relative yields of $C_4H_3^+$ and $C_4H_2^+$ are found to deviate from the expected behavior at photon energies slightly above 14.6 eV (850 Å). Stemming from the fair agreement of this value with the calculated AE of reaction 9 (14.9 eV), it is logical to consider this feature to be evidence that the $C_4H_3^+$ ions formed by reaction 7 further fragment into $C_4H_2^+ + H$ with little kinetic shift. This experiment cannot exclude the contribution of reaction 8 to the increase in intensity of $C_4H_2^+$ when the $C_2H_2^+$ moiety in $(C_2H_2)_2^+$ is prepared in the $\tilde{A}^2\Sigma_g^+$ state. Nevertheless, it is fair to conclude that reaction 9 contributes significantly to the observed increase in the formation of $C_4H_2^+$ at energies above the IE of the $\tilde{A}^2\Sigma_g^+$ state.

As a result of the perturbation of C_2H_2, the ionization threshold for $C_2H_2^+(\tilde{A}^2\Sigma_g^+) \cdot C_2H_2$ is expected to be lower than the IE for the $\tilde{A}^2\Sigma_g^+$ state of $C_2H_2^+$. Previous experiments (29,30,44) show that this shift, which arises mainly from stronger ion-dipole and/or ion-induced dipole interactions of the dimer ion in the nuclear configuration of the neutral dimer, compared to the van der Waals attractive interaction of the neutral dimer, is usually about 0.1-0.2 eV. Theoretically, this shift cannot be greater than the difference of the dissocation energies for $C_2H_2^+(\tilde{A}^2\Sigma_g^+) \cdot C_2H_2$ and $C_2H_2 \cdot C_2H_2$. Assuming the dissociation energy for $C_2H_2^+(\tilde{X}^2\Pi_u) \cdot C_2H_2$ to be the same as that for $C_2H_2^+(\tilde{A}^2\Sigma_g^+) \cdot C_2H_2$, this difference is less than 1.0 eV (30,31). The fact that the observed

onset (~14.9 eV) for the increase and the decrease in relative abundances of $C_4H_2^+$ and $C_4H_3^+$, respectively, is approximately 1.5 eV lower than the IE for the $\tilde{A}^2\Sigma_g^+$ state makes the previous claim concerning the specific reactivity of the $\tilde{A}^2\Sigma_g^+$ state of $C_2H_2^+$ in reactions 1, 2 and 3 very doubtful. The possibility that the quartet state, which is below the $\tilde{A}^2\Sigma_g^+$, might be populated in electron impact experiments (6,7,11,20) cannot be excluded. Based on the above arguments, this experiment suggests that the substantial increase in the yield of $C_4H_2^+$, observed in previous collisional experiments, is mainly due to reaction 3 and that both vibrational and electronic energies are effective in promoting this reaction provided it is energetically allowed. The fluorescence from the $\tilde{A}^2\Sigma_g^+$ state to the ground $\tilde{X}^2\Pi_u$ state has not been observed (42); some of the $C_2H_2^+(\tilde{A}^2\Sigma_g^+)$ ions might actually be interconverted to vibrationally excited $C_2H_2^+(\tilde{X}^2\Pi_u)$ by nonradiative pathways before reacting with C_2H_2.

Figure 3 shows the pressure dependence of the relative intensities of $(C_2H_2)_2^+$ (and/or $C_4H_4^+$), $C_4H_3^+$, $C_4H_2^+$ and $(C_2H_2)_3^+$ obtained at $T_0 \approx 230K$ and at the photon wavelength of 700 Å (~17.7 eV). At a low stagnation pressure, where the concentration of the acetylene trimer is negligible, the intensity of $C_4H_2^+$ is greater than that of $C_4H_3^+$. As the concentration of $(C_2H_2)_3$ is increased as a result of raising the nozzle stagnation pressure, the intensity of $C_4H_3^+$ is found to increase faster than that of $C_4H_2^+$ and the $C_4H_3^+$ ion becomes the major species at $P_0 \gtrsim 560$ Torr (45). In accordance with the above discussion, the formation of $C_4H_2^+ + 2H$ by reaction 9 is likely to be stepwise process

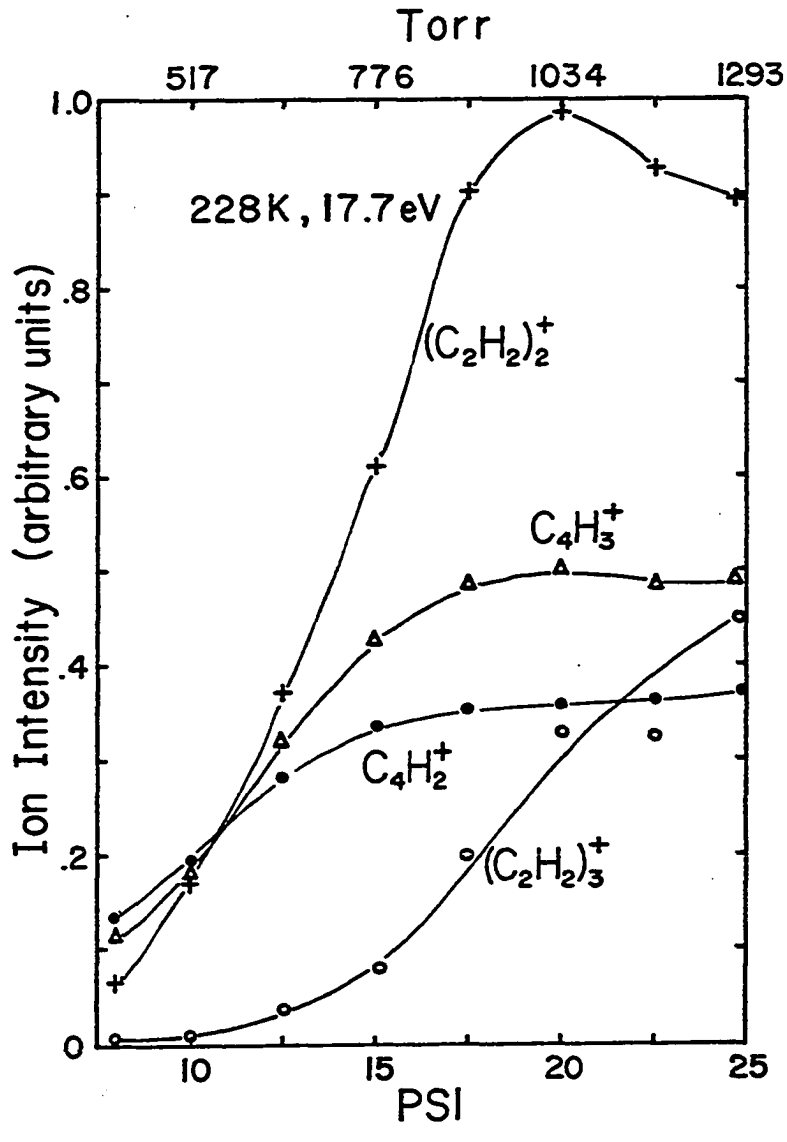

Figure 3. The pressure dependence of the relative intensities for $(C_2H_2)_3^+$, $(C_2H_2)_2^+$, $C_4H_3^+$ and $C_4H_2^+$ measured at 700 Å (17.7 eV)

$$(C_2H_2)_2^+ \rightarrow (C_4H_4^+)^{**} \xrightarrow{(a)} (C_4H_3^+)^{**} + H \xrightarrow{(b)} C_4H_2^+ + 2H \quad . \qquad (10)$$

The processes involved in the formation of $C_4H_2^+$ from $(C_2H_2)_3^+$ will be (46)

$$(C_2H_2)_3^+ \rightarrow (C_4H_4^+)^{**}C_2H_2 \rightarrow (C_4H_3^+)^{**} \cdot C_2H_2 + H \rightarrow C_4H_2^+ + 2H + C_2H_2 \quad . \qquad (11)$$

However, the activated intermediates $(C_4H_4^+)^{**} \cdot C_2H_2$ and $(C_4H_3^+)^{**} \cdot C_2H_2$ of reaction 11 can also decay by the dissociation processes

$$(C_4H_4^+)^{**} \cdot C_2H_2 \rightarrow (C_4H_4^+)^{*} + C_2H_2 \qquad (12)$$

$$(C_4H_3^+)^{**} \cdot C_2H_2 \rightarrow (C_4H_3^+)^{*} + C_2H_2 \qquad (13)$$

in which the $(C_4H_4^+)^*$ and $(C_4H_3^+)^*$ ions will be stabilized by channeling some of the excess energy into the internal motion of C_2H_2 as well as the kinetic energies of the fragments. In cases when the internal energy contents of $(C_4H_4^+)^*$ and $(C_4H_3^+)^*$ are too low for further fragmentations, such as step (a) of reaction 10, the intensities of the $C_4H_4^+$ and $C_4H_3^+$ ions will increase at the expense of the formation of $C_4H_2^+$. The rapid increase in yields for $C_4H_4^+$ and $C_4H_3^+$ as a function of the nozzle stagnation pressure as shown in Fig. 3 is consistent with this interpretation. Figure 4 shows the variations of the intensities of $(C_2H_2)_2^+$ (and/or $C_4H_4^+$), $C_4H_3^+$, $C_4H_2^+$ and $(C_2H_2)_3^+$ <u>versus</u> P_0 obtained at $T_0 \approx 230K$ and at the photon wavelength of 810 Å (≈15.3 eV). The pressure dependence plots for $(C_2H_2)_2^+$ (and/or $C_4H_4^+$)and $(C_2H_2)_3^+$ obtained at

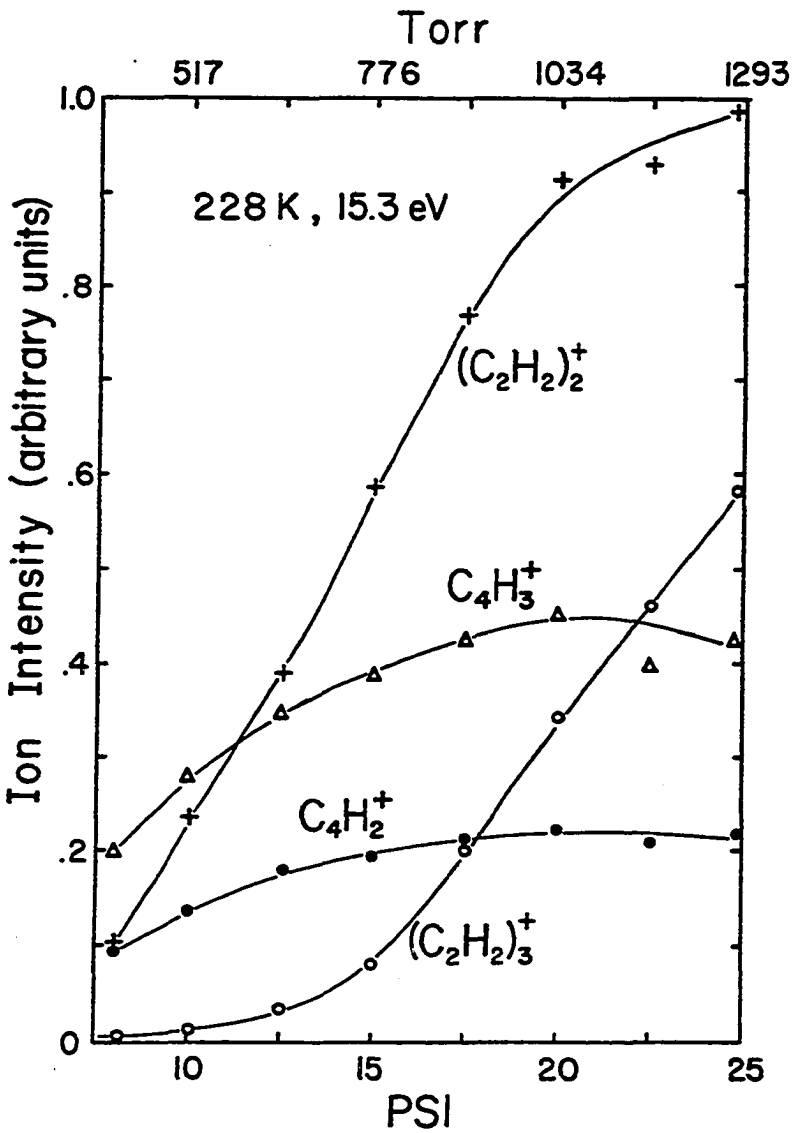

Figure 4. The pressure dependence of the relative intensities for $(C_2H_2)_3^+$, $(C_2H_2)_2^+$, $C_4H_3^+$ and $C_4H_2^+$ measured at 810 Å (15.3 eV)

700 and 810 Å are similar. The values for $I(C_4H_2^+)/I(C_4H_3^+)$ measured at different stagnation pressures at 700 Å are compared with those obtained at 810 Å in Table 3. At 810 Å, it was found that the ratio $I(C_4H_2^+)/I(C_4H_3^+)$ remains nearly constant ($\sim$0.5) as P_0 varies from $\sim$414 to 1293 Torr. Since the photon energy used in Fig. 4 is close to the thermochemical threshold of reaction 9 and the probability for further fragmentation of $(C_4H_3^+)^{**}$ formed by reaction 10a is low in the time scale of this experiment ($\sim 10^{-5}$ sec) (47), the stabilization of $(C_4H_3^+)^{**}$ by reaction 13 will only have a minor effect in the pressure dependence of the intensity for $C_4H_3^+$. However, the slight increase in the value of $I(C_4H_2^+)/I(C_4H_3^+)$ from 0.49 to 0.51 as P_0 increases from 414 to 1293 Torr shows that reaction 10b occurs to some extent at 810 Å (15.3 eV). The nearly constant value observed at 810 Å for $I(C_4H_2^+)/I(C_4H_3^+)$ at different nozzle stagnation pressures is also consistent with the conclusion that the branching ratios for the formation of $C_4H_2^+$ and $C_4H_3^+$ from $C_2H_2^+(\tilde{X}^2\Pi_u) \cdot C_2H_2$ is similar to that from $C_2H_2^+(\tilde{X}^2\Pi_u) \cdot (C_2H_2)_2$.

The PIE curves for $C_4H_2^+$ and $C_4H_3^+$ near the thresholds obtained at $T_0 \approx 298$K and $P_0 \approx 1000$ Torr are magnified and shown in Fig. 5. Within the experimental uncertainties, the AEs of $C_4H_2^+$ and $C_4H_3^+$ from $(C_2H_2)_2$ were found to be identical and have the value of 10.9 ± 0.05 eV (1137 ± 5 Å). These values are slightly lower than, but within the error estimates of those (1142 ± 5 Å) observed at $T_0 \approx 230$K and $P_0 \approx 1000$ Torr, a nozzle condition at which an appreciable concentration of $(C_2H_2)_3$ in the beam was produced (31). The thermodynamical thresholds for reactions 7 and 8 are 10.88 and 10.40 eV, respectively. Therefore,

Table 3. Pressure dependence of the ratio for the intensity of $C_4H_2^+$ to that of $C_4H_3^+$ at ionization photon energies of 15.3 (810 Å) and 17.7 eV (700 Å)

Ionization Energy	Nozzle Stagnation Pressure (Torr)							
(eV)	414	517	646	776	905	1034	1163	1293
15.3 (810 Å)	0.49	0.49	0.48	0.50	0.50	0.49	0.52	0.51
17.7 (700 Å)	1.17	1.08	0.88	0.79	0.72	0.72	0.75	0.75

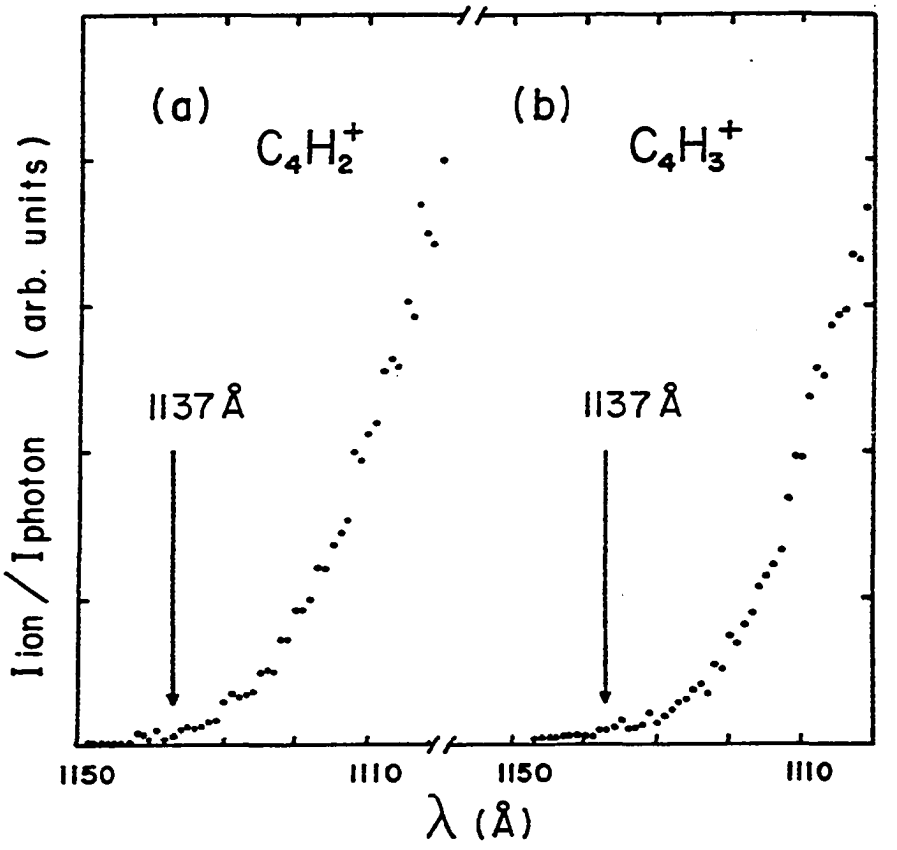

Figure 5. Photoionization efficiency curves for (a) $C_4H_2^+$ and (b) $C_4H_3^+$ near the thresholds. Experimental conditions; $P_0 \approx 1000$ Torr, $T_0 \approx 298$K, wavelength resolution = 1.4 Å (FWHM)

these measurements suggest that reaction 1 proceeds with no activation energy, whereas ∿12 kcal/mol is needed to overcome the potential barrier for the elimination of H_2 by reaction 2.

Koyano et al. (48) reported the observation of $C_4H_3^+$ and $C_4H_2^+$ by irradiating acetylene in a gas cell at 1216 Å. They interpreted these products to be the results of chemiionization processes of excited acetylene molecules. A very careful search for $C_4H_3^+$ and $C_4H_2^+$ signals were made in this wavelength region but we found no evidence for such processes. A similar conclusion was noted by Futrell and Tiernan (7) in an electron impact study. In the experiment of Koyano and Tanaka, the source of 1216 Å radiation was produced by a low pressure hydrogen discharge lamp with a LiF window used to separate the gas chamber and the radiation source. Since the LiF window will transmit radiation having wavelengths longer than ∿1040 Å (49), the $C_4H_3^+$ and $C_4H_2^+$ ions observed by Koyano and Tanaka were probably formed by ion-molecule reactions such as reaction 1, 2 and 3 induced by weak molecular hydrogen emission from the discharge lamp.

In order to better visualize the observations made in this study, a pseudo reaction coordinate diagram shown in Fig. 6 is constructed based on the thermochemical data reported in the literature (31,35-37, 50-54) (Table 1) and the AEs for $C_4H_3^+$ and $C_4H_2^+$ obtained in this study. The most stable geometry for $C_4H_2^+$ corresponds to a diacetylene ion structure. The structure of the $C_4H_3^+$ ion is not known. A recent calculation using the semi-empirical INDO technique prefers the linear

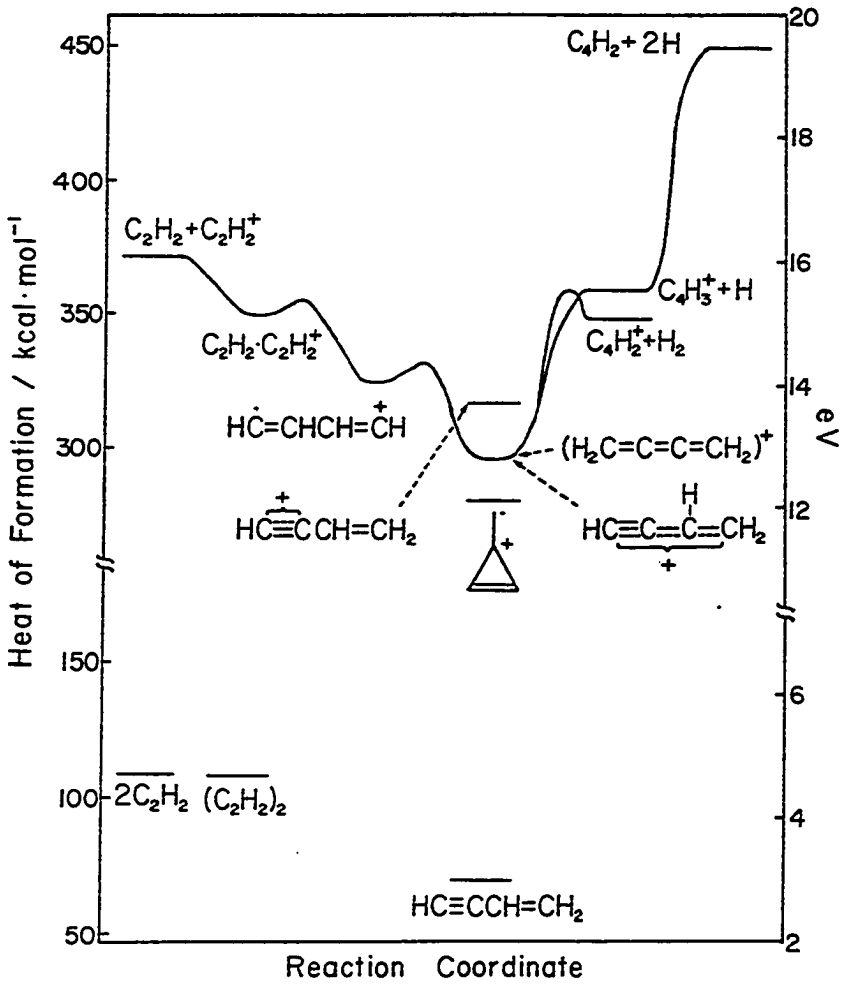

Figure 6. Pseudo reaction coordinate diagram for the decomposition of $(C_2H_2)_2^+$

carbon chain structures $CH_2=C\overset{\cdot}{\cdot\cdot}C\cdot\cdot C\cdot\cdot CH$ for the neutral C_4H_3 radical (55). The simple molecular orbital theory predicts that the highest occupied molecular orbital of this radical is of nonbonding character associated with the allyl radical-like π-type molecular orbital (56). Therefore, the $C_4H_3^+$ ion, which is formed by ejecting the nonbonding electron to the continuum, should have a structure similar to the C_4H_3 radical, i.e., $CH_2=C\overset{+}{\cdot\cdot}C\cdot\cdot C\cdot\cdot CH$. One of the possible configurations adjacent to the $(C_2H_2)_2^+$ complex might involve the formation of a C-C bond between $C_2H_2^+$ and C_2H_2 and give rise to $HC\dot{=}CH-CH=\overset{+}{C}H$. The energetics of this radical ion is also unknown. The stability of $HC\dot{=}CH-CH=\overset{+}{C}H$ shown in Fig. 5 is just a rough estimate. There are several possible stable structures corresponding to the stoichiometry of $C_4H_4^+$. They are the 1-buten-3-yne, butatriene, cyclobutadiene and methylenecyclopropene ions. According to previous investigations (50,52,53), the methylenecyclopropene ion is believed to be the most stable structure and has a value for the heat of formation of 276-285 kcal/mol. Electron impact experiments showed that the 1-buten-3-yne ion can fragment into $C_4H_2^+ + H_2$ and $C_4H_3^+ + H$ (54,57). It is interesting to note that the AE for $C_4H_3^+$ from 1-buten-3-yne reported by Field et al. (54) is in excellent agreement with that from $(C_2H_2)_2$ determined here on the total energy scale (heat of formation for the neutral precursor plus ionization energy). The measured AE for $C_4H_2^+$ from 1-buten-3-yne is slightly higher (∿0.25 eV) than that from $(C_2H_2)_2$ (54). Recently, in a study of the metastable decomposition of the 1-buten-3-yne ion, Lifshitz et al. (57) found the kinetic energy releases

for the $C_4H_3^+ + H$ and the $C_4H_2^+ + H_2$ channels to be ~0.045 and 0.411 eV, respectively. These measurements are consistent with the activation barriers obtained for reactions 1 and 2 in this experiment. These comparisons show that the highest potential energy barrier for reaction 8 is most likely located between the stable $C_4H_4^+$ isomer and $C_4H_2^+ + H_2$. In Fig. 6, we have assumed that the stable $C_4H_4^+$ complex involved has the 1-buten-3-yne ion structure. In fact, at the total energies of concern in this experiment, other isomers such as the butatriene and methylenecyclopropene ions are also accessible.

The analysis of the photoelectron spectrum (PES) of the 1-buten-3-yne (58-59) shows that the first IE corresponds to the ionization of an electron from the butadiene-like π-type molecular orbital. Hence, the structure of the ground state 1-buten-3-yne ion should have the $H_2C\overset{+}{\overbrace{\cdot\doteq\cdot CH\cdot\doteq\cdot C\cdot\doteq\cdot}}CH$ structure. The strongest band in the PES of 1-buten-3-yne is the second band which arises from the ionization of an electron in the acetylene-like π-type molecular orbital. The structure for the first excited state should be $H_2C{=}CH{-}\overset{+}{\overbrace{C\cdot\doteq\cdot}}CH$. Since the total energy range of the experiment is more than 44 kcal/mol higher than the heat of formation of the latter ion, a plausible mechanism for the decomposition of $(C_2H_2)_2^+$ to form $C_4H_3^+ + H$ is

$$(C_2H_2)_2^+ \rightarrow \overset{\cdot}{H}C{=}CH{-}\overset{+}{C}H{=}CH \xrightarrow{(a)} HC\overset{+}{\overbrace{\cdot\doteq\cdot C}}{-}CH{=}CH_2 \xrightarrow{(b)} HC\overset{+}{\overbrace{\cdot\doteq\cdot C\cdot\doteq\cdot}}C{=}CH_2{+}H \quad . \tag{14}$$

There is evidence that in numerous carbocations, hydrogen shifts precede

decomposition (5,6,60-62). The activation barrier for 1,2-hydrogen shift is estimated to be ∿6-12 kcal/mol (63). Thus, step 14a, which involves hydrogen shifts, is expected to be fast. The formation of $C_4H_3^+$ in step 14b simply proceeds by ejection of the β-hydrogen from the excited 1-buten-3-yne ion.

Assuming the $C_4H_2^+$ ion to have the diacetylene ion structure, the formation of $C_4H_2^+ + H$ from $HC\overset{+}{\overbrace{\dot{=}\dot{C}}}-CH=CH_2$ might involve the elimination of the α and β hydrogen atoms. It has been pointed out previously that the concerted 1,2-elimination of H_2 occurring through a planar transition state is a symmetry-forbidden process (64). Kinetic energy release studies on the 1,2-elimination of molecular hydrogen from many precursor ions indicated that activation energies for H_2 losses are high (64,65). In many cases, due to the lower barrier to 1,2-hydrogen shifts, a 1,1-elimination of H_2 is believed to be the favored route. It is noteworthy that the 1,1-elimination of H_2 is a symmetry-allowed process (65). The fact that the AEs for the formation of $C_4H_2^+ + H_2$ and $C_4H_3^+ + H$ are the same seems to imply that the transition state, which determines the activation energy of reaction 8, has a structure very similar to that of the $C_4H_3^+$ ion. Based on this interpretation, one possible mechanism for the formation of $C_4H_2^+ + H_2$ from $HC\dot{=}\dot{C}-CH=CH$ is

$$HC\overset{+}{\overbrace{\dot{=}\dot{C}}}-CH=CH_2 \xrightarrow{(a)} HC\overset{+}{\overbrace{\dot{=}\dot{C}\dot{=}\dot{C}}}=CH_2 \xrightarrow{(b)} HC\overset{+}{\overbrace{\dot{=}\dot{C}\dot{=}\dot{C}\dot{=}\dot{C}}}H + H_2 \quad . \quad (15)$$

Step 15a involves the stretching of the C-H bond in the β-position and

the forming of an activated complex having the $C_4H_3^+$ ion structure with the H atom loosely attached to it. In step 15b, the weakly bonded H atom picks up an α-hydrogen to form $C_4H_2^+ + H_2$. This might actually proceed by a 1,1-elimination of H_2 preceded by a 1,2-hydrogen shift. Combining the results of this experiment, a rigorous theoretical study will shed light on the collision-complex mechanism for the ion-molecule reactions of $C_2H_2^+ + C_2H_2$.

REFERENCES

1. F. H. Field, J. L. Franklin and F. W. Lampe, J. Am. Chem. Soc. 79, 2665 (1957).

2. R. Barker, W. H. Hamill and R. R. Williams, Jr., J. Phys. Chem. 63, 825 (1959).

3. R. Fuchs, Z. Naturforsch 16a, 1026 (1961).

4. E. Lindholm, I. Szabo and P. Wilmenius, Ark. Fys. 25, 417 (1963).

5. M. S. B. Munson, J. Phys. Chem. 69, 572 (1965).

6. J. J. Myher and A. G. Harrison, Can. J. Chem. 46, 1755 (1968).

7. J. H. Futrell and T. O. Tiernan, J. Phys. Chem. 72, 158 (1968).

8. R. M. O'Malley and K. R. Jennings, Int. J. Mass Spectrom. Ion Phys. 2, 257 (1969).

9. A. A. Herod and A. G. Harrison, Int. J. Mass Spectrom. Ion Phys. 4, 415 (1970).

10. S. E. Buttrill, Jr., J. Chem. Phys. 50, 4125 (1969).

11. G. A. W. Derwish, A. Galli, A. Giardini-Guidoni and G. G. Volpi, J. Am. Chem. Soc. 87, 1159 (1965).

12. A. Bloch, Adv. Mass Spectrom. 2, 48 (1963).

13. C. E. Melton and W. H. Hamill, J. Chem. Phys. 41, 1469 (1964).

14. J. H. Futrell and L. W. Sieck, J. Phys. Chem. 69, 892 (1965).

15. P. S. Rudolph and C. E. Melton, J. Phys. Chem. 63, 916 (1959).

16. S. W. Wexler, A. Lifshitz and A. Quattrochi, Adv. Chem. Ser. 58, 193 (1966).

17. J. H. Futrell and T. O. Tiernan in Ion-Molecule Reactions, edited by J. L. Franklin (Plenum, New York, 1972), p. 485.

18. P. G. Miasek and J. L. Beauchamp, Int. J. Mass Spectrom. Ion Phys. 15, 49 (1974).

19. S. E. Buttrill, Jr., J. Chem. Phys. 62, 1834 (1975).

20. I. H. Suzuki, Int. J. Mass Spectrom. Ion Phys. 40, 167 (1981).

21. I. Szabo and P. J. Derrick, Int. J. Mass Spectrom. Ion Phys. 7, 55 (1971).

22. V. P. Warneck, Ber. Bunsen Phys. Chem. 76, 421 (1972).

23. Y. Ono and C. Y. Ng, J. Chem. Phys. 74, 6985 (1981).

24. C. Baker and D. W. Turner, Chem. Commun. 797 (1967).

25. J. M. Hollas and T. A. Sutherley, Molec. Phys. 21, 183 (1971).

26. M. I. Al-Joboury, D. P. May and D. W. Turner, J. Chem. Soc. 616 (1965).

27. R. G. Cavell and D. A. Allisen, J. Chem. Phys. 69, 159 (1978).

28. M. E. Gress, S. H. Linn, Y. Ono, H. F. Prest and C. Y. Ng, J. Chem. Phys. 72, 4242 (1980).

29. Y. Ono, S. H. Linn, H. F. Prest, M. E. Gress and C. Y. Ng, J. Chem. Phys. 74, 1125 (1981).

30. C. Y. Ng, Adv. Chem. Phys. 52, 1982 (in press).

31. See Section VII.

32. S. T. Ceyer, P. W. Tiedemann, C. Y. Ng, B. H. Mahan and Y. T. Lee, J. Chem. Phys. 70, 2138 (1979).

33. R. Botter, V. H. Dibeler, J. A. Walker and H. M. Rosenstock, J. Chem. Phys. 44, 1271 (1966).

34. J. Berkowitz, Photoabsorption, Photoionization, and Photoelectron Spectroscopy (Academic Press, New York, 1979), p. 284.

35. H. M. Rosenstock, K. Draxl, B. W. Steiner and J. T. Herron, J. Phys. Chem. Ref. Data 6, Suppl. 1 (1977).

36. J. O. Hirschfelder, C. F. Curtiss and R. B. Bird, Molecular Theory of Gases and Liquids (Wiley, New York, 1964), p. 1112.

37. W. L. Smith, Proc. Roy. Soc. (London) A300, 519 (1967).
C. Baker and D. W. Turner, Proc. Roy. Soc. (London) A308, 19 (1968).

38. In the construction of the relative abundance diagram (Fig. 2), minor product channels such as $C_3H_3^+ + CH$, $C_2H_3^+ + C_2H$, etc. have been omitted. The low intensities observed for $C_2H_3^+$ and $C_3H_3^+$ justify omitting these channels.

39. G. M. L. Verboom and G. G. Meisels, J. Chem. Phys. 68, 2714 (1978).

40. G. G. Meisels, G. M. L. Verboom, M. J. Weiss and T. C. Hsieh, J. Am. Chem. Soc. 101, 7189 (1979). According to Meisels et al., if the fragmentation of the reaction complex is treated in the quasi-diatomic approximation and the attractive potential is governed entirely by the ion-dipole interaction, the maximum in the effective potential energy barrier ($V_{eff,max}$) along the dissociation reaction coordinate is related to the reduced mass (μ) of the quasi-diatomic complex, the total angular momentum (J), and the polarizability (α) of the neutral fragment by the relation: $V_{eff,max} = J^4/8\alpha e^2\mu^2$. In this case, $\alpha(H) = 0.667$ Å^3, $(H_2) = 0.79$ Å^3 (Ref. 36), and μ associated with the $C_4H_2^+ + H$ channel is approximately twice that for the $C_4H_3^+ + H$ channel. Thus, $V_{eff,max}$ for H ejection is greater than that for H_2 elimination, and the formation of $C_4H_2^+ + H_2$ is predicted to be the favorable channel for higher J values.

41. R. J. Buenker and S. D. Peyerimohoff, Chem. Rev. 74, 127 (1974).

42. J. P. Maier, in Kinetics of Ion-Molecule Reactions, edited by P. Ausloos (Plenum, New York, 1979), NATO-Advanced Study Institutes Series B, Vol. 40, p. 449.

43. T. Baer, P.-M. Guyan, I. Nenner, A. Tabsché-Fouhaillé, R. Botter, L. F. A. Ferreira and T. R. Govers, J. Chem. Phys. 70, 1585 (1979).

44. S. H. Linn and C. Y. Ng, J. Chem. Phys. 75, 4921 (1981).

45. This observation shows that $C_4H_3^+$ and $C_4H_2^+$ are also primary fragments of $(C_2H_2)_3^+$.

46. If the $(C_2H_2)_3^+$ ions rearrange to some stable $C_6H_6^+$ ions before fragmenting, the processes involved will be

$$(C_2H_2)_3^+ \rightarrow (C_6H_6^+)^* \rightarrow C_6H_5^{+*} + H \rightarrow C_4H_2^+ + C_2H_2 + 2H \quad .$$

47. The flight time of an ion from the ionization region to the ion detector is estimated to be 10^{-5} sec.

48. I. Koyano, I. Tanaka and I. Omura, J. Chem. Phys. 40, 2734 (1964).

49. A. H. Laufer, J. A. Pirog and J. R. McNesby, J. Opt. Soc. Am. 55, 64 (1965).

50. T. Baer, G. D. Willet, D. Smith and J. S. Phillips, J. Chem. Phys. 70, 4076 (1979).

51. J. H. D. Eland, J. Berkowitz, H. Schulte and R. Frey, Int. J. Mass Spectrom. Ion Phys. 28, 297 (1978).

52. H. M. Rosenstock, K. E. McCulloh and F. P. Lossing, Int. J. Mass Spectrom. Ion Phys. 25, 327 (1977).

53. H. M. Rosenstock, R. Stockbauer and A. C. Parr, Int. J. Mass Spectrom. Ion Phys. 38, 323 (1981).

54. F. H. Field, J. L. Franklin and F. W. Lampe, J. Am. Chem. Soc. 79, 2665 (1957).

55. A. Hinchliffe, J. Mol. Struct. 39, 123 (1977).

56. A. Streitwieser, Jr., Molecular Orbital Theory for Organic Chemists (Wiley, New York, 1961).

57. C. Lifshitz, D. Gibson, K. Levsen and I. Dotan, Int. J. Mass Spectrom. Ion Phys. 40, 157 (1981).

58. P. Bruckmann and M. Klessinger, J. Electron Spectrosc. Rel. Phenom. 2, 341 (1973).

59. M. D. Van Hoorn, J. Electron Spectrosc. Rel. Phenom. 6, 65 (1975).

60. I. Baumel, R. Hagemann and R. Botter, 19th Annual Conference on Mass Spectrometry and Allied Topics, Committee E.14 A.S.T.M., Atlanta, Georgia, May 1971.

61. B. Davis, D. H. Williams and A. N. H. Yeo, J. Chem. Soc. B 81 (1970).

62. N. A. Uccella and D. H. Williams, J. Am. Chem. Soc. 94, 8778 (1972).

63. W. A. Lathan, W. J. Hehre and J. A. Pople, J. Am. Chem. Soc. 93, 808 (1971).

64. D. H. Williams and G. Hvistendahl, J. Am. Chem. Soc. 96, 6753 (1974).

65. D. H. Williams and G. Hvistendahl, J. Am. Chem. Soc. 96, 6755 (1974).

SECTION VII.

A STUDY OF THE UNIMOLECULAR DECOMPOSITION OF THE $(C_2H_2)_3^+$ COMPLEX

INTRODUCTION

The mechanism for the unimolecular decomposition of the benzene ion has been the subject of many experimental (1-9) and theoretical (7,10,11) investigations during the last decade. The major fragment ions resulting from the unimolecular decomposition of the excited benzene molecular ions with excitation energies below 20 eV are $C_6H_5^+$, $C_6H_4^+$, $C_4H_4^+$ and $C_3H_3^+$. The same product ions are observed from C_6H_6 such as 1,5-hexadiyne (8,12), 2,4-hexadiyne (8,12-14) and 1,3-hexadiyne (12,14). The fact that, within experimental errors, the benzene, 1,5-hexadiyne and 2,4-hexadiyne molecular ions dissociate to the four product ions with identical branching ratios in the total energy range ∿15.0-15.5 eV (neutral C_6H_6 heat of formation plus excitation energy) indicates that these isomers of $C_6H_6^+$ rearrange to a common precursor ion prior to fragmentation. The experimental and calculated unimolecular fragmentation rates for $C_6H_6^+$ are consistent with the interpretation that this common precursor has the benzene molecular ion structure (8). Above this energy range, there is evidence that newly accessible processes involve some intermediate complexes other than the common precursor ions (8,13,14). The kinetic energy release data of Keough et al. (15) suggest that the reactive form of the benzene molecular ion at higher excitation energies has an acyclic structure.

Here, the results of a study of the unimolecular decomposition of acetylene trimer ions which are synthesized by the direct photoionization of van der Waals trimers of acetylene are reported.

$$(C_2H_2)_3 + h\nu \rightarrow (C_2H_2)_3^+ + e^- \qquad (1)$$

Due to the weak interactions between the acetylene molecules in $(C_2H_2)_3$, the ionization process 1, to a first approximation, involves the ionization of only one of the acetylene molecules. The resulting $(C_2H_2)_3^+$ ion, consisting of an acetylene molecular ion and two neutral acetylene molecules held together by polarization forces, can be considered to be a collisional complex formed in a trimolecular collision of $C_2H_2^+ + 2C_2H_2$. A question concerning these loose trimer ions is whether they isomerize to some stable $C_6H_6^+$ ions before fragmenting. By identifying the fragment ions of $(C_2H_2)_3^+$ and comparing the branching ratios of the fragments from $(C_2H_2)_3^+$ with those observed from other stable $C_6H_6^+$ isomers at the same total energy, we have obtained significant insight into the unimolecular decomposition of $(C_2H_2)_3^+$.

EXPERIMENTAL

The $(C_2H_2)_3$ was produced by supersonic expansion through a 120 μm diameter nozzle orifice at a nozzle temperature (T_0) of approximately 230K and a stagnation pressure (P_0) of 1000 Torr. Under these expansion conditions, ions containing more than six carbon atoms could not be detected, indicating that the concentration of higher acetylene clusters $(C_2H_2)_n$, $n > 3$ were negligible and C_2H_2, $(C_2H_2)_2$, $(C_2H_2)_3$ were the major constituents of the molecular beam. Since the acetylene beam was sampled in a collisionless environment, the observed fragment ions represent the primary fragments of $C_2H_2^+$, $(C_2H_2)_2^+$ and $(C_2H_2)_3^+$. The acetylene was obtained from Matheson with a quoted purity of ≥99.6%.

All data were obtained with an optical resolution of 1.4 Å (FWHM). Data points were taken typically at either 0.5 or 1 Å intervals. Due to the low signal intensity of the $C_6H_4^+$ ion, data were taken at 25 Å intervals beyond the threshold region. The standard deviations obtained are ≤10% for $C_6H_6^+$ (or $(C_2H_2)_3^+$), $C_6H_5^+$ and $C_4H_4^+$, and ≤20% for $C_6H_4^+$ and $C_3H_3^+$. Each pohotionization efficiency (PIE) curve was based on at least two scans, and the prominent structures in the curves were found to be reproducible.

RESULTS AND DISCUSSION

The ions observed in the region 600-1260 Å are C_2H^+, $C_2H_2^+$, $C_3H_3^+$, $C_4H_2^+$, $C_4H_3^+$, $C_4H_4^+$ (and/or $(C_2H_2)_2^+$), $C_6H_4^+$, $C_6H_5^+$ and $(C_2H_2)_3^+$ (and/or $C_6H_6^+$). The analysis of the PIE curves for C_2H^+ (16) and $C_2H_2^+$ (17) near the thresholds have been reported elsewhere. The profiles of the PIE curves for $C_3H_3^+$, $C_4H_2^+$, $C_4H_3^+$, $C_4H_4^+$ (and/or $(C_2H_2)_2^+$), $C_6H_4^+$, $C_6H_5^+$ and $(C_2H_2)_3^+$ (and/or $C_6H_6^+$) are similar.

Figures 1(a), (b), (c), (d) and (e) show the PIE curves for $(C_2H_2)_3^+$ (and/or $C_6H_6^+$), $C_6H_5^+$, $C_6H_4^+$, $C_4H_4^+$ (and/or $(C_2H_2)_2^+$) and $C_3H_3^+$, respectively, in the region ~650-1275 Å obtained at $P_0 \approx 1000$ Torr and using a wavelength resolution of 1.4 Å (FWHM). The peak observed in the PIE curves at ~800-850 Å arises from autoionizing states of C_2H_2. A similar structure was evident in the PIE curve for $C_2H_2^+$ (18). At energies higher than approximately 12.56 eV (987 Å), which is the thermochemical threshold for the process

$$(C_2H_2)_2 + h\nu \rightarrow C_3H_3^+ + CH + e^- \quad . \qquad (2)$$

$C_3H_3^+$ might also arise from the fragmentation of $(C_2H_2)_2$. The ionization energy (IE) of $(C_2H_2)_3$ was determined to be 9.83 ± 0.04 eV (1261 ± 5 Å) and within experimental uncertainties, the appearance energies (AE) for $C_3H_3^+$, $C_4H_4^+$, $C_6H_4^+$ and $C_6H_5^+$ from $(C_2H_2)_3$ were all found to be 10.10 ± 0.04 eV (1228 ± 5 Å).

It is unknown whether the mass 52 ions observed near the onset as shown in Fig. 1(d) have the tight $C_4H_4^+$ or the loose $(C_2H_2)_2^+$ structure.

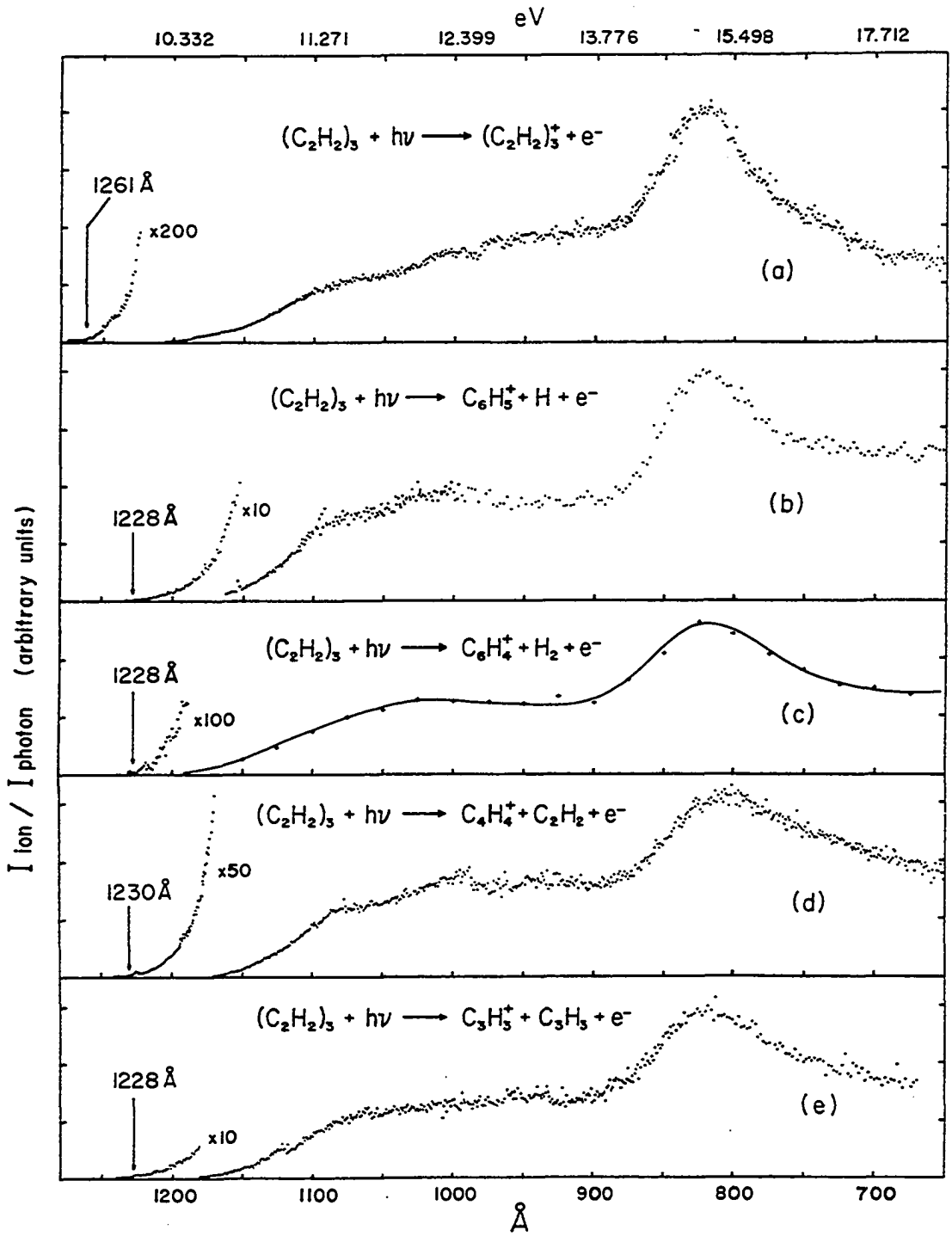

Figure 1. PIE curves in the region 650-1275 Å for (a) $(C_2H_2)_3^+$, (b) $C_6H_5^+$, (c) $C_6H_4^+$, (d) $C_4H_4^+$, and (e) $C_3H_3^+$

Interestingly, the AE of the mass 52 ions determined at $P_0 \approx 1000$ Torr was found to be approximately 0.36 eV lower than that obtained at a stagnation pressure of $P_0 \approx 350$ Torr, where the $(C_2H_2)_3$ and heavier cluster concentrations were negligible. The PIE curves near the thresholds for the mass 52 ions obtained at $P_0 \approx 1000$ and 350 Torr are plotted on the same sensitivity scale and are shown in Figs. 2(a) and (b), respectively. At $P_0 \lesssim 350$ Torr, the mass 52 ions should have the structure of $(C_2H_2)_2^+$ and are mainly produced by the photoionization process

$$(C_2H_2)_2 + h\nu \rightarrow (C_2H_2)_2^+ + e^- \quad . \tag{3}$$

Therefore, the IE of $(C_2H_2)_2$ was determined to be 10.44 ± 0.04 eV (1188 ± 5 Å). At $P_0 \approx 1000$ Torr, the mass 52 ions can be formed by process 3 and the photodissociative ionization processes

$$(C_2H_2)_3 + h\nu \rightarrow (C_2H_2)_2^+ + C_2H_2 + e^- \tag{4}$$

$$\rightarrow C_4H_4^+ + C_2H_2 + e^- \quad . \tag{5}$$

Since the AE of process 4 is expected to be higher than the IE of $(C_2H_2)_2$, the mass 52 ions observed in Fig. 1(d) below the IE of $(C_2H_2)_2$ must have a structure corresponding to some stable isomers of $C_4H_4^+$ instead of a loose $(C_2H_2)_2^+$ structure.

The observation that the AE for the mass 52 ions from $(C_2H_2)_3$ is lower than the IE of $(C_2H_2)_2$ is contrary to the expectation of previous findings concerning the threshold measurements of the clusters of some

simple inorganic molecules such as $(O_2)_{n=2-5}$ (19,20), $(N_2)_{n=2,3}$, $(CO)_{n=2,3}$ (21), $(CO_2)_{n=2-4}$ (22) and $(CS_2)_{n=2-5}$ (23). In all the latter cases, AEs of the dimer ion fragments from the trimers and heavier clusters were all found to be higher than the IE of the corresponding dimers. A reasonable explanation for the difference observed between systems involving hydrocarbons (24) and simple inorganic molecules is that, for hydrocarbon cluster ions, there exists tight structure such as $C_4H_4^+$ which is much more stable than the loose $(C_2H_2)_2^+$ complex, whereas the cluster ions of these simple inorganic molecules can only exist as loose complexes. The lower AE of process 5 in comparison with process 4 is simply the result that $\Delta H_f^\circ(C_2H_2)_2^+)$ is greater than $\Delta H_f^\circ(C_4H_4^+)$.

Using the IEs of C_2H_2 (11.396 ± 0.003 eV) (17,25,26) and $(C_2H_2)_2$, and the estimated dissociation energy of $C_2H_2 \cdot C_2H_2$ (27), the dissociative energy $(D_0((C_2H_2)_2^+))$ can be calculated from the relation

$$D_0((C_2H_2)_2^+) = IE(C_2H_2) + D_0((C_2H_2)_2) - IE((C_2H_2)_2) \quad . \qquad (6)$$

The calculated dissociation energy for $C_2H_2^+ \cdot C_2H_2$ is 22.5 ± 1 kcal/mol. It is interesting to note that, within error estimates of the experiments, this value is equal to the dissociation energies determined for $N_2^+ \cdot N_2$ (20.8 ± 1.2 kcal/mol) and $CO^+ \cdot CO$ (22.4 ± 1 kcal/mol) (21). This observation leads one to speculate that the interaction of the electrons in the carbon carbon triple bonds of C_2H_2 and $C_2H_2^+$ is mainly responsible for the stability of $(C_2H_2)_2^+$. The good agreement found between the dissociation energies for $(C_2H_2)_2^+$, $(N_2)_2^+$ and $(CO)_2^+$ can also be taken as a support for the validity of the IE of $(C_2H_2)_2$ determined here. Assuming

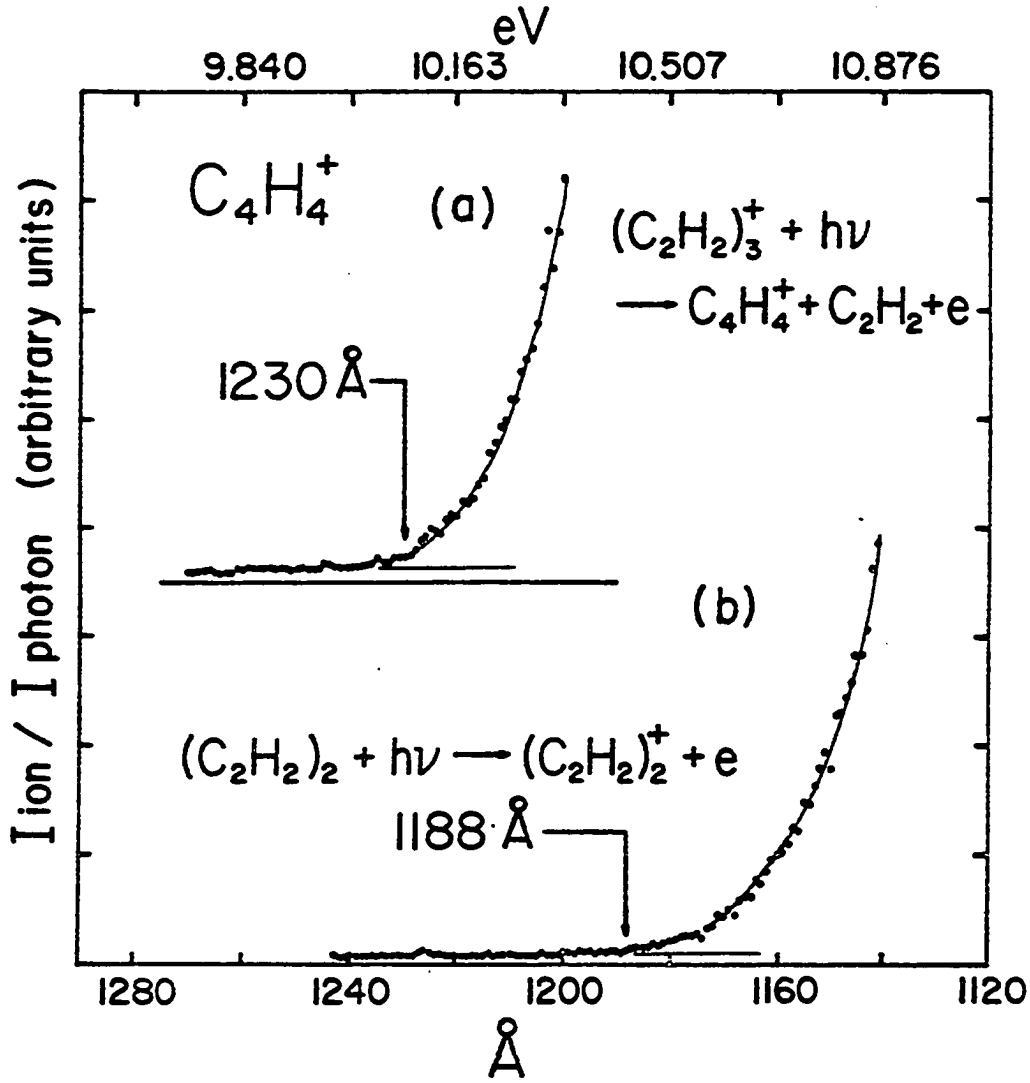

Figure 2. PIE curves for the mass 52 ions near the thresholds. (a) PIE curve for $C_4H_4^+$ near the threshold. Experimental conditions: $P_0 \approx 1000$ Torr, $T_0 \approx 230$K, wavelength resolution = 1.4 Å (FWHM). (b) PIE curve for $(C_2H_2)_2^+$ near the threshold $P_0 \approx 350$ Torr, $T_0 \approx 230$K, wavelength resolution = 1.4 Å (FWHM)

the binding energy for $(C_2H_2)_2 + C_2H_2$ to be the same as that for $C_2H_2 + C_2H_2$, and using the IEs of $(C_2H_2)_2$ and $(C_2H_2)_3$, a value of 14.4 ± 1 kcal/mol was deduced from a relation similar to Eq. 6. This value, however, was found to be substantially greater than the lower bounds for the dissociation energies for $(CO)_2^+ \cdot CO$ (3.7 kcal/mol) and $(N_2)_2^+ \cdot N_2$ (1.4 kcal/mol) reported by Linn et al. (21).

The $C_4H_2^+$ and $C_4H_3^+$ ions are the major fragment ions from $(C_2H_2)_2$. The pressure dependence measurements of the intensities for $C_4H_3^+$ and $C_4H_2^+$ strongly suggest that the $C_4H_3^+$ and $C_4H_2^+$ ions are also the primary fragments from $(C_2H_2)_3$ in the region ∿650-1142 Å. Figures 3(a) and (b) show the PIE curves for $C_4H_2^+$ and $C_4H_3^+$ near the thresholds obtained at $P_0 \approx 1000$ Torr. The AEs of these two ions were also found to be identical and have the value of 10.86 ± 0.05 eV (1142 ± 5 Å). The neutral products for the $C_4H_3^+$ and $C_4H_2^+$ channels are not known. Based on the known thermodynamic data (27-31) (see Table 1), the thermochemical thresholds for the processes

$$(C_2H_2)_3 + h\nu \rightarrow C_4H_3^+ + C_2H_3 + e^- \quad (7)$$

$$\rightarrow C_4H_3^+ + C_2H_2 + H + e^- \quad (8)$$

$$\rightarrow C_4H_2^+ + C_2H_4 + e^- \quad (9)$$

$$\rightarrow C_4H_2^+ + C_2H_2 + H_2 + e^- \quad (10)$$

are calculated to be 9.10, 10.89, 8.60 and 10.40 eV, respectively. Since these values are lower than or equal to the observed AEs of $C_4H_3^+$

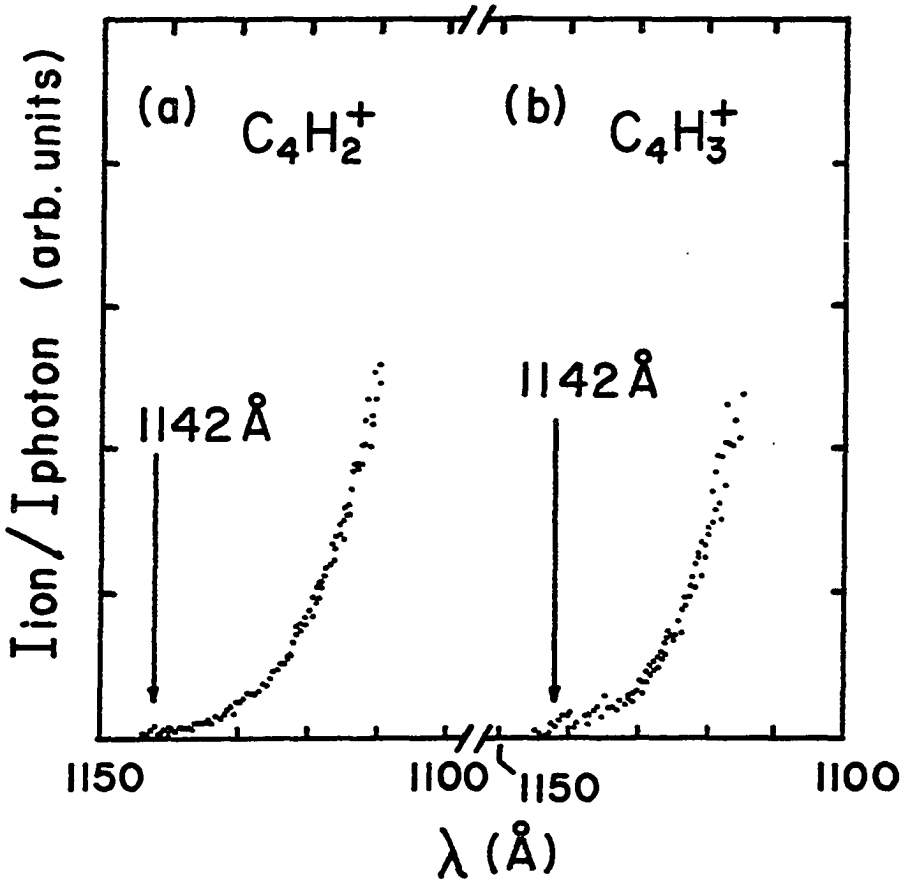

Figure 3. PIE curves near the threshold for (a) $C_4H_2^+$ and (b) $C_4H_3^+$. Experimental conditions: $P_0 \approx 1000$ Torr, $T_0 \approx 230$K, wavelength resolution = 1.4 Å (FWHM)

Table 1. 298K heats of formation in kcal/mol of neutrals and ions[a]

Compound	Neutrals	Ions
$(C_2H_2)_3$	162.2 ± 0.4[b] (27,28)	388.9 ± 1.0[c]
Benzene	19.82 ± 0.12 (28)	233 (28)
2,4-hexadiyne	86 ± 1 (8) 90 ± 2 (12)	291 ± 1 (8) 295 ± 5 (12)
2,3-hexadiyne	95 ± 2 (12)	301 ± 5 (12)
1,4-hexadiyne	98 ± 2 (12)	316 ± 5 (12)
1,5-hexadiyne	99.5 (12)	328 ± 1 (8) 329 ± 2 (12)
$C_6H_5^+$		264 ± 1 (8) 266 ± 2 (34,35) 270 ± 4 (36) 270 (43)
$C_6H_4^+$		~318 (7) 315 ± 3 (44)
$(C_2H_2)_2$	108 ± 0.2[b] (27,28)	348.9 ± 1[c]
C_4H_4		276 ± 2 (8) 280 ± 2 (37) 385 ± 3 (45)
C_4H_3		307 (29)
C_4H_2		348 (30)

[a]The number in the parentheses are the references.

[b]Heats of formation at 0K.

[c]This work. Because of the high degree of rotational and low frequency vibrational relaxation in the supersonic expansion, these values, which are deduced from the measured IE's for $(C_2H_2)_2$ and $(C_2H_2)_2$, can be considered to be the heats of formation at 0K.

Table 1. Continued

Compound	Neutrals	Ions
C_3H_3	80 (8) 80.7 (38)	255 (8) 256 ± 2 (39) 255.5 (40) 257 (12)
C_2H_4	12.49 (28)	
C_2H_3	65 (31)	
C_2H_2	54.34 (28) 54.19[b] (28)	317.2 (28)
H	52.10 (28)	

and $C_4H_2^+$, processes 7, 8, 9 and 10 must be considered to be possible reactions near the experimental onsets. From the metastable transitions (32), it is known that the $C_6H_5^+$ and $C_6H_4^+$ ions from benzene fragment further to form $C_4H_3^+$ and $C_4H_2^+$, respectively. Hence, this finding also suggests that C_2H_2 + H and C_2H_2 + H_2 should be included as likely neutral products for the $C_4H_3^+$ and $C_4H_2^+$ channels, respectively.

According to previous photoionization studies on benzene (7,8,12), the $C_6H_5^+$, $C_6H_4^+$, $C_4H_4^+$ and $C_3H_3^+$ ions formed at the fragmentation thresholds are believed to have the structure of the phenyl, benzyne, methylenecyclopropene and cyclopropenyl ions, respectively. In order to visualize the observation of this study, a pseudo reaction coordinate diagram (Fig. 4) is constructed by using the thermochemical data reported in the literature (8,12,27-31,33-45) and those obtained in this study (Table 1). The AEs for the formation of $C_6H_5^+$ + H, $C_6H_4^+$ + H_2, $C_4H_4^+$ + C_2H_2, $C_4H_3^+$ + C_2H_3 (or C_2H_2 + H), $C_4H_2^+$ + C_2H_4 (or C_2H_2 + H_2) and $C_3H_3^+$ + C_3H_3 from benzene, 1,5-hexadiyne, 2,4-hexadiyne and 1,4-hexadiyne have been measured previously by photoionization (7,12,13,42) and electron impact (12,41) mass spectrometry. Some selected measurements on the AEs of these fragments are listed in Table 2 and compared on the total energy scale with the results obtained here. We note that the $C_6H_5^+$ as well as the $C_4H_4^+$ fragment onsets from benzene are very close on the total energy scale to values obtained from the linear C_6H_6 isomers. The differences between the AEs and the corresponding thermochemical thresholds of these processes were attributed to the kinetic shift effects (46-48). These effects have been demonstrated by studying the

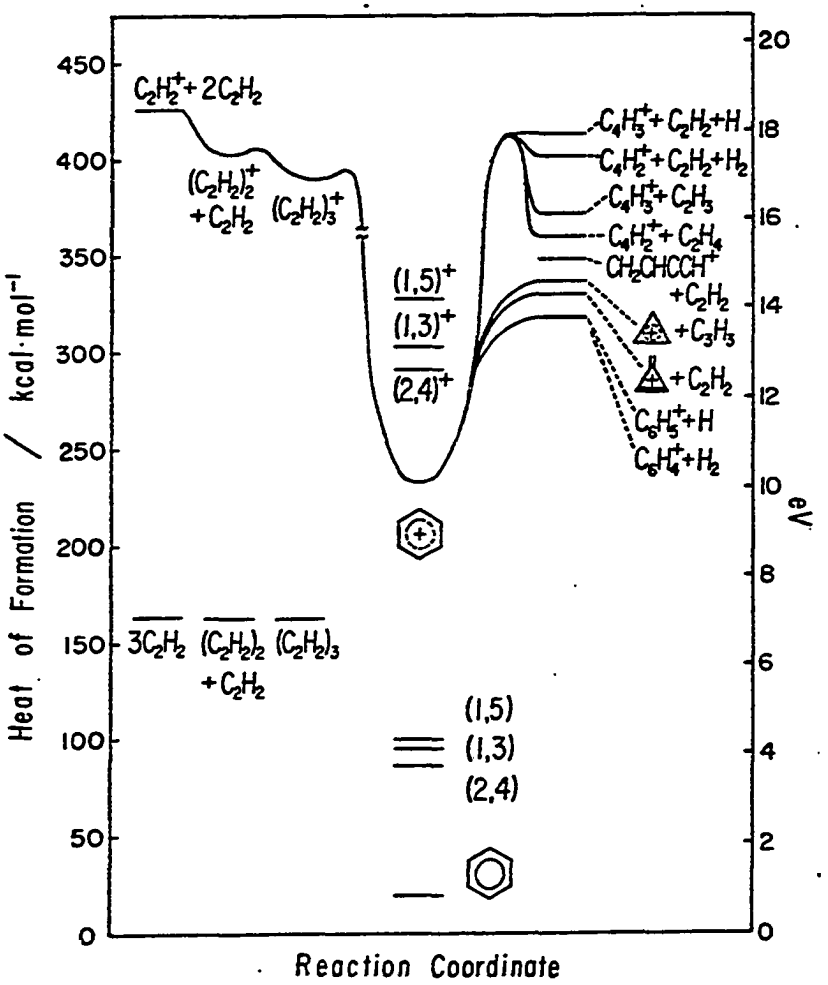

Figure 4. Pseudo reaction coordinate diagram for the decomposition of $(C_2H_2)_3^+$. Here, (1,3), (1,5), (2,4), $(1,3)^+$, $(1,5)^+$ and $(2,4)^+$ represent 1,3-hexadiyne, 1,5-hexadiyne, 2,4-hexadiyne and their ions, respectively

Table 2. Selected experimental appearance energies (AE) of $C_6H_5^+$, $C_6H_4^+$, $C_4H_4^+$, $C_4H_3^+$, $C_4H_2^+$, $C_3H_3^+$ from $(C_2H_2)_3^+$ and some stable $C_6H_6^+$ isomers

Process	AE (eV)	T.E.[a] (eV)	Ref.
$(C_2H_2)_3 + h\nu \rightarrow C_6H_5^+ + H + e^-$	10.10 ± 0.04	17.13 ± 0.04	This work
$HC{\equiv}C\text{-}CH_2\text{-}CH_2\text{-}C{\equiv}CH + h\nu \rightarrow C_6H_5^+ + H + e^-$	10.16 ± 0.08	14.47 ± 0.11	12
$HC{\equiv}C\text{-}CH_2\text{-}C{\equiv}C\text{-}CH_3 + e^- \rightarrow C_6H_5^+ + H + 2e^-$	10.21 ± 0.1	14.46 ± 0.13	12
$H_3C\text{-}C{\equiv}C\text{-}C{\equiv}C\text{-}CH_3 + h\nu \rightarrow C_6H_5^+ + H + e^-$	10.55 ± 0.09	14.28 ± 0.10[b] 14.45 ± 0.12[c]	12
C_6H_6 (benzene) $+ h\nu \rightarrow C_6H_5^+ + H + e^-$	13.78 ± 0.08 ≈13.95	14.64 ± 0.08	12 7
C_6H_6 (benzene) $+ h\nu \rightarrow C_6H_5^+ + H + e^-$	13.74 ± 0.1	14.60 ± 0.1	12
$(C_2H_2)_3 + h\nu \rightarrow C_6H_4^+ + H_2 + e^-$	10.10 ± 0.04	17.13 ± 0.04	This work
C_6H_6 (benzene) $+ h\nu \rightarrow C_6H_4^+ + H_2 + e^-$	≈13.90	≈14.76	7

[a]Total energy = AE plus the heat of formation of the neutral isomer.

[b]Calculated values by using ΔH°_{f298}(2,4-hexadiyne) = 86 ± 1 kcal/mol. See Ref. 8.

[c]Calculated values by using ΔH°_{f298}(2,4-hexadiyne) = 90 ± 2 kcal/mol. See Ref. 12.

Table 2. Continued

Process	AE (eV)	T.E.[a] (eV)	Ref.
$(C_2H_2)_3 + h\nu \rightarrow C_4H_4^+ + C_2H_2 + e^-$	10.10 ± 0.04	17.13 ± 0.04	This work
$HC\equiv C-CH_2CH_2-C\equiv CH + h\nu \rightarrow C_4H_4^+ + C_2H_2 + e^-$	10.42 ± 0.08	14.73 ± 0.11	12
$H_3C\equiv C-C-C\equiv C-CH_3 + h\nu \rightarrow C_4H_4^+ + C_2H_2 + e^-$	11.27 ± 0.2	15.00 ± 0.2	12
C_6H_6 (benzene) $+ h\nu \rightarrow C_4H_4^+ + C_2H_2 + e^-$	14.17 ± 0.08 ≈14.30	15.03 ± 0.08	12 7
$(C_2H_2)_3 + h\nu \rightarrow C_4H_3^+ + C_2H_3$ (or $C_2H_2 + H$) $+ e^-$	10.86 ± 0.05	17.89 ± 0.08	This work
$H_3C-C\equiv C-C\equiv C-CH_3 + h\nu \rightarrow C_4H_3^+ + C_2H_3$ (or $C_2H_2 + H$) $+ e^-$	14.6 ± 0.1	18.33 ± 0.11[b] 18.50 ± 0.13[c]	13
$HC\equiv C-CH_2-CH_2-C\equiv CH + h\nu \rightarrow C_4H_3^+ + C_2H_3$ (or $C_2H_2 + H$) $+ e^-$	13.05 - 13.78	17.36 - 18.10	12
C_6H_6 (benzene) $+ e^- \rightarrow C_4H_3^+ + C_2H_3$ (or $C_2H_2 + H$) $+ 2e^-$	17.6 ± 0.1	18.46 ± 0.1	41
$(C_2H_2)_3 + h\nu \rightarrow C_4H_2^+ + C_2H_4$ (or $C_2H_2 + H_2$) $+ e^-$	10.86 ± 0.05	17.89 ± 0.08	This work
$H_3C-C\equiv C-C\equiv C-CH_3 + h\nu \rightarrow C_4H_2^+ + C_2H_4$ (or $C_2H_2 + H_2$) $+ e^-$	14.1 ± 0.05	17.83 ± 0.07[b] 18.00 ± 0.10[c]	42
	14.05 ± 0.1	17.78 ± 0.11[b] 17.95 ± 0.13[c]	13
$HC\equiv C-CH_2-CH_2-C\equiv CH + h\nu \rightarrow C_4H_2^+ + C_2H_4$ (or $C_2H_2 + H_2$) $+ e^-$	13.05 - 13.78	17.38 - 18.10	12

Table 2. Continued

Process	AE (eV)	T.E.[a] (eV)	Ref.
C_6H_6 (benzene) + e^- → $C_4H_2^+$ + C_2H_4 (or C_2H_2 + H_2) + $2e^-$	17.5 ± 0.3	18.36 ± 0.3	41
$(C_2H_2)_3$ + hν → $C_3H_3^+$ + C_3H_3 + e^-	10.10 ± 0.04	17.13 ± 0.04	This work
C_6H_6 (benzene) + hν → $C_3H_3^+$ + C_3H_3 + e^-	∿14.25	∿15.11	7

effect of the ion residence time on the AE of $C_6H_5^+$ in benzene (49-51). Gordon and Reid (51) found that the AE decreased from 14.1 ± 0.1 eV to 12.7 ± 0.1 eV as the ion residence time increased from ca. 5 μs to 1200 μs. The kinetic energy release studies of Cooks et al. (52) and Jones et al. (53) reveal only small kinetic energy releases for the $C_4H_4^+ + C_2H_2$ and $C_6H_5^+ + H$ channels, indicating that there are no significant barriers to the reverse reactions. The total energies corresponding to the AEs for $C_6H_5^+$, $C_6H_4^+$, $C_4H_4^+$ and $C_3H_3^+$ from $(C_2H_2)_3^+$ are much higher than those deduced from the AEs of these fragment ions from other stable $C_6H_6^+$ precursors. This is partly due to the higher heat of formation of $(C_2H_2)_3^+$ in comparison to the stabilities of the product fragments $C_6H_5^+ + H$, $C_6H_4^+ + H_2$, $C_4H_4^+ + C_2H_2$ and $C_3H_3^+ + C_3H_3$. The difference of 0.26 ± 0.06 eV between the AEs for $C_6H_5^+$, $C_6H_4^+$, $C_4H_4^+$ and $C_3H_3^+$ from $(C_2H_2)_3$, and the IE of $(C_2H_2)_3$ can be attributed to the potential energy barrier for the rearrangement of $(C_2H_2)_3^+$ to other stable $C_6H_6^+$ ions. One of the most interesting results of this study is that the total energies (412 kcal/mol) corresponding to the AEs for $C_4H_3^+$ and $C_4H_2^+$ determined here are in fair agreement with those derived from the AEs of these two ions from stable $C_6H_6^+$ isomers (see Table 3). Assuming the formation of $C_4H_3^+$ and $C_4H_2^+$ to be mainly due to processes 7-10, this observation is consistent with the conclusion that the $(C_2H_2)_3^+$ ions rearrange to some stable $C_6H_6^+$ precursor ions before fragmenting.

The relative intensities for $(C_2H_2)_3^+$ (and/or $C_6H_6^+$), $C_6H_5^+$, $C_6H_4^+$, $C_4H_4^+$ and $C_3H_3^+$ measured at 1200 Å (10.33 eV) were 24, 1.0, 0.29, 6.5 and 0.37, respectively. At this excitation energy, there should be no

contribution to the $C_3H_3^+$ and $C_4H_4^+$ ions from the acetylene dimers. The uncertainty in internal energy of the $(C_2H_2)_3^+$ ions formed is expected to be equal to $h\nu$ - $IE((C_2H_2)_3)$ = 10.33 - 9.83 = 0.5 eV. Assuming a uniform distribution of internal energies for $(C_2H_2)_3^+$ in the total energy range 16.87-17.37 eV, the observed branching ratios for $(C_2H_2)_3^+$ (and/or $C_6H_6^+$), $C_6H_5^+$, $C_6H_4^+$, $C_4H_4^+$ and $C_3H_3^+$ from $(C_2H_2)_3$ can be viewed as state selected data with an energy spread of ∿0.5 eV. The relative fragment ion intensities from state selected benzene (3,9), 2,4-hexadiyne (13) and 1,3-hexadiyne (14) molecular ions have been determined previously by photoion-photoelectron coincidence and charge transfer methods. The energy resolutions used in Refs. 3, 13 and 14 are estimated to be 0.2, 0.3 and 0.3 eV, respectively. In order to make a meaningful comparison of the results of these studies with those observed here, the relative intensities (54) of $C_6H_5^+$, $C_6H_4^+$, $C_4H_4^+$ and $C_3H_3^+$ were obtained by averaging the values scaled from the breakdown diagrams reported in Refs. 3, 9, 13 and 14 at intervals of ∿0.1 eV in the total energy range ∿16.87-17.37 eV. These average values, together with the results of the present study, are listed in Table 3. The intensity of $C_6H_5^+$ has been normalized to 1.0. The branching ratios for $C_6H_5^+$, $C_6H_4^+$ and $C_3H_3^+$ from $(C_2H_2)_3$ are in reasonable agreement with those from benzene, 2,4-hexadiyne and 1,3-hexadiyne. However, the relative intensity of $C_4H_4^+$ from $(C_2H_2)_3$ is approximately a factor of three greater than those observed from other stable C_6H_6 isomers. The higher intensity for $C_4H_4^+$ observed here may be partly due to the finite collisional dissociation process

Table 3. The average values for relative fragment ion intensities from the dissociation of various isomers of $C_6H_6^+$ and $(C_2H_2)_3^+$ in the total energy (ionization energy + neutral C_6H_6 (or $(C_2H_2)_3$) heat of formation) range of 16.87-17.37 eV (normalized for the intensity of $C_6H_5^+$)

Isomer	Fragments[a]				
	$C_6H_6^+$ (or $(C_2H_2)_3^+$)	$C_6H_5^+$	$C_6H_4^+$	$C_4H_4^+$	$C_3H_3^+$
$(C_2H_2)_3$[b]	24 ± 1.8	1.00 ± 0.10	0.29 ± 0.06	6.5 ± 0.7	0.37 ± 0.07
benzene[c]	∿0	1.00 ± 0.37	0.23 ± 0.14	1.66 ± 0.46	0.44 ± 0.26
benzene[d]	∿0.08	1.00	0.20	2.73	0.72
2,4-hexadiyne[e]	∿0	1.00 ± 0.08	0.28 ± 0.03	2.00 ± 0.14	0.56 ± 0.05 (0.40 ± 0.05)[f]
1,3-hexadiyne[g]	∿0	1.00 ± 0.14	0.12 ± 0.04	1.92 ± 0.14	0.52 ± 0.07

[a]The average values for the fragment ion intensities in the total energy range 16.87-17.37 eV from various isomers of $C_6H_6^+$ are obtained by scaling breakdown diagrams shown in Refs. 3, 9, 13, and 14.

[b]This work.

[c]Reference 3. The total energy range 16.87-17.17 eV corresponds to the excitation energy in the range 16.0-16.5 eV.

[d]Reference 9.

[e]Reference 13. The total energy range 16.87-17.37 eV corresponds to the excitation energy in the range 13.14-13.64 eV. Since the data in the excitation energy range ∿13.14-13.4 are not available, the values listed in the table represent the average values in the excitation energy range ∿13.4-13.64 eV.

[f]The value of 0.4 for the relative intensity of $C_3H_3^+$ is deduced from the ratio of the $C_3H_3^+$ and $C_4H_4^+$ intensities in Ref. 8 and the average relative intensity for $C_4H_4^+$ reported in Ref. 13.

[g]Reference 14. The total energy range 16.87-17.37 eV corresponds to the excitation energy in the range ∿12.75-13.25 eV.

$$(C_2H_2)_3^+ + M \rightarrow (C_2H_2)_2^+ + C_2H_2 + M \quad . \qquad (11)$$

Because of the relatively low dissociation energy for $(C_2H_2)_2^+ \cdot C_2H_2$, the cross section for process 11 is expected to be large. The assumption that the distribution of internal energies for $(C_2H_2)_3^+$ is uniform in the total energy range 16.87-17.37 eV might also give rise to some discrepancies in this comparison. According to the study of Baer et al. (8), at total energies above ~16.5 eV, there is evidence that the precursors involved in the fragmentation of the 1,5-hexadiyne ion are different from those involved in the dissociation of the benzene and 2,4-hexadiyne ions. Thus, $(C_2H_3)_3^+$ may also react by a different direct mechanism at these energies without sampling a region of a common $C_6H_6^+$ phase space. In any case, the good agreement observed between the relative intensities of $C_6H_5^+$, $C_6H_4^+$ and $C_3H_3^+$ from $(C_2H_2)_3$ and those of Refs. 3, 9, 13 and 14 support the interpretation that the dominant route for the decomposition of the $(C_2H_2)_3^+$ ions is the complex mechanism which involves the rearrangement of $(C_2H_2)_3^+$ to some precursors prior to dissociation common to other stable $C_6H_6^+$ isomers. Thus,

$$(C_2H_2)_3^+ \rightarrow (C_6H_6^+)^* \rightarrow C_6H_5^+ + H \qquad (12)$$

$$\rightarrow C_6H_4^+ + H_2 \qquad (13)$$

$$\rightarrow C_4H_4^+ + C_2H_2 \qquad (14)$$

$$\rightarrow C_3H_3^+ + C_3H_3 \qquad (15)$$

The longest reaction time sampled in this experiment is $\sim 10^{-5}$ sec which is defined by the flight time of an ion from the ionization region to the entrance of the quadrupole mass spectrometer. Since the potential energy barrier for the rearrangement of $(C_2H_2)_3^+$ to other stable $C_6H_6^+$ isomers is only $\sim$0.26 eV, the lifetimes of the $(C_2H_2)_3^+$ complexes having internal excitations slightly above the barrier are expected to be shorter than 10^{-5} sec. As shown in Table 3, the intensity of $(C_2H_2)_3^+$ (and/or $C_6H_6^+$) is found to be much higher than those of the stable $C_6H_6^+$ ions observed in Refs. 3, 9, 13 and 14, implying that only a fraction of the $(C_2H_2)_3^+$ ions formed by process 1 at 1200 Å (10.33 eV) have sufficient internal energy to overcome this barrier and dissociate according to reactions 12-15. As the excitation energy increases, the internal energy distribution will favor the dissociation processes and the intensity of the parent ion should decrease. Table 4 lists the relative intensities of $(C_2H_2)_3^+$ (and/or $C_6H_6^+$), $C_6H_4^+$, $C_4H_4^+$ (and/or $(C_2H_2)_2^+$), and $C_3H_3^+$ obtained at several photon energies. The rapid decrease of the intensity of $(C_2H_2)_3^+$ (and/or $C_6H_6^+$) relative to other species is in accordance with this expectation. The relative intensities of $C_6H_5^+$ and $C_6H_4^+$ remain constant in the energy range 10.33-19.10 eV. The increases in intensities for $C_4H_4^+$ and $C_3H_3^+$ with respect to those of $C_6H_5^+$ and $C_6H_4^+$ at higher energies probably have contributions from processes 2 and 3.

In summary, the experimental observations which support the conclusion that the $(C_2H_2)_3^+$ ions rearrange to some common precursors as do other stable $C_6H_6^+$ isomers are:

Table 4. Photoionization mass spectra of $(C_2H_2)_3^{+a,b}$

(A)	$C_6H_6^+$ or $(C_2H_2)_3^+$	$C_6H_5^+$	$C_6H_4^+$	$C_4H_4^+$	$C_3H_3^+$
1200	24.0	1.00	0.29	6.5	0.37
1175	8.7	1.00	0.20	6.8	0.34
1100	3.2	1.00	0.19	14.3	0.43
1000	3.2	1.00	0.19	15.0	0.53
900	3.0	1.00	0.19	15.2	0.65
800	3.1	1.00	0.20	15.4	0.71
700	2.9	1.00	0.19	15.2	1.02
650	2.8	1.00	0.20	14.3	1.10

[a]These measurements have not been corrected for the transmission factors of various ions.

[b]The error estimates for the relative intensities of $C_6H_6^+$ (or $(C_2H_2)_3^+$), $C_6H_5^+$ and $C_4H_4^+$ (or $(C_2H_2)_2^+$) are approximately 10%. For the relative intensities of $C_6H_4^+$ and $C_3H_3^+$, the uncertainties are estimated to be better than 20%.

(1) The fragment ions observed from $(C_2H_2)_3^+$ are identical to those from other stable $C_6H_6^+$ isomers.

(2) The AE of $C_4H_4^+$ from $(C_2H_2)_3$ was found to be lower in energy than the IE of $(C_2H_2)_2$.

(3) The measured AEs for the formation of $C_4H_3^+$ and $C_4H_2^+$ from the $(C_2H_2)_3$ in the total energy scale are in agreement with the AEs of these two ions from 2,4-hexadiyne, 1,5-hexadiyne and benzene.

(4) The relative intensities of the $C_6H_5^+$, $C_6H_4^+$ and $C_3H_3^+$ ions from $(C_2H_2)_3$ and those reported previously from benzene, 2,4-hexadiyne and 1,3-hexadiyne in the total energy range 16.87-17.17 eV were found to be in fair agreement.

REFERENCES

1. B. Andlauer and Ch. Ottinger, J. Chem. Phys. 55, 1471 (1971); B. Andlauer and Ch. Ottinger, Z. Naturforsch. Teil A 27, 293 (1972).

2. J. H. D. Eland and H. Schulte, J. Chem. Phys. 62, 3835 (1975).

3. J. H. D. Eland, R. Frey, H. Schulte and B. Brehm, Int. J. Mass Spectrom. Ion Phys. 21, 209 (1976).

4. J. H. Beynon, R. M. Caprioli, W. O. Perry and W. E. Baitinger, J. Am. Chem. Soc. 94, 6828 (1972).

5. W. A. Chupka, in Chemical Spectroscopy and Photochemistry in the Vacuum-Ultraviolet, edited by C. Sandorfy, P. J. Ausloos and M. B. Robin (Reidel, Dordrecht, 1974), p. 433.

6. W. A. Chupka, J. Berkowitz and S. I. Miller, paper presented at American Society for Mass Spectrometry, 20th Annual Conference on Mass Spectrometry and Applied Topics, Dallas, Texas, June 1972.

7. H. M. Rosenstock, J. T. Larkins and J. A. Walker, Int. J. Mass Spectrom. Ion Phys. 11, 309 (1973).

8. T. Baer, G. D. Willett, D. Smith and J. S. Phillips, J. Chem. Phys. 70, 4076 (1979).

9. B. O. Jonsson and E. Lindholm, Ark. Fys, 39, 65 (1969).

10. C. E. Klots, Z. Naturforsch. Teil A 27, 553 (1972).

11. M. L. Vestal, in Fundamental Processes in Radiation Chemistry, edited by P. Ausloos (Wiley, New York, 1968), p. 59.

12. H. M. Rosenstock, K. E. McCulloh and F. P. Lossing, Int. J. Mass Spectrom. Ion Phys. 25, 327 (1977).

13. J. Dannacher, Chem. Phys. 29, 339 (1978).

14. J. Dannacher, Adv. Mass Spectrom. 8A, 37 (1979).

15. T. Keough, T. Ast, J. H. Beynon and R. G. Cooks, Org. Mass Spectrom. 7, 245 (1973).

16. Y. Ono and C. Y. Ng, J. Chem. Phys. 74, 6985 (1981).

17. See section V.

18. R. Botter, V. H. Dibeler, J. A. Walker and H. M. Rosenstock, J. Chem. Phys. 44, 1271 (1966).

19. S. L. Anderson, T. Hirooka, P. W. Tiedemann, B. H. Mahan and Y. T. Lee, J. Chem. Phys. 73, 4779 (1980).

20. S. H. Linn, Y. Ono and C. Y. Ng, J. Chem. Phys. 74, 3348 (1981).

21. S. H. Linn, Y. Ono and C. Y. Ng, J. Chem. Phys. 74, 3342 (1981).

22. S. H. Linn and C. Y. Ng, J. Chem. Phys. 75, 4921 (1981).

23. See section II.

24. A similar observation was found in the photoionization study of $(C_2H_4)_2$ and $(C_2H_4)_3$. Y. Ono and C. Y. Ng, to be published.

25. V. H. Dibeler and J. A. Walker, Int. J. Mass Spectrom. Ion Phys. 11, 49 (1973).

26. V. H. Dibeler, J. A. Walker and K. E. McCulloh, J. Chem. Phys. 59, 2264 (1973).

27. J. O. Hirschfelder, C. F. Curtiss and R. B. Bird, Molecular Theory of Gases and Liquids, (Wiley, New York, 1964), p. 1112.

28. H. M. Rosenstock, K. Draxl, B. W. Steiner and J. T. Herron, J. Phys. Chem. Ref. Data 6, Suppl. 1 (1977).

29. F. H. Field, J. L. Franklin and F. W. Lampe, J. Am. Chem. Soc. 79, 2665 (1957).

30. W. L. Smith, Proc. Roy. Soc. (London) A300, 519 (1967);
C. Baker and D. W. Turner, Chem. Commun. 797 (1967);
C. Baker and D. W. Turner, Proc. Roy. Soc. (London) A308, 19 (1968).

31. A. G. Harrison and F. P. Lossing, J. Am. Chem. Soc. 82, 519 (1960).

32. Ch. Ottinger, Z. Naturforsch. 20A, 1229 (1965).

33. S. W. Benson, Thermochemical Kinetics, (John Wiley and Sons, New York, 1968).

34. Y. Sergeev, M. E. Akopyan and G. I. Vilesov, Opt. Spektrosk. 32, 230 (1972).

35. D. M. Golden and S. W. Benson, Chem. Rev. 69, 125 (1969).

36. J. L. Beauchamp, Adv. Mass Spectrom. 6, 717 (1974).

37. J. H. D. Eland, J. Berkowitz, H. Schulte and R. Frey, Int. J. Mass Spectrom. Ion Phys. 28, 297 (1978).

38. W. Tsang, Int. J. Chem. Kinet. 2, 23 (1970).

39. F. P. Lossing, Can. J. Chem. 50, 3973 (1972).

40. A. C. Parr and F. A. Elder, J. Chem. Phys. 49, 2659 (1968).

41. C. Lifshitz and B. G. Reuben, J. Chem. Phys. 50, 951 (1969).

42. Reference 13 of Ref. 12.

43. H. M. Rosenstock, R. Stockbauer and A. C. Parr, J. Chem. Phys. 73, 773 (1980).

44. H. M. Rosenstock, R. Stockbauer and A. C. Parr, J. Chim. Physique 77, 745 (1980).

45. H. M. Rosenstock, R. Stockbauer and A. C. Parr, Int. J. Mass Spectrom. Ion Phys. 38, 323 (1981).

46. L. Friedman, F. A. Long and M. Wolfsberg, J. Chem. Phys. 26, 714 (1957).

47. L. Friedman, F. A. Long and M. Wolfsberg, J. Chem. Phys. 27, 613 (1957).

48. W. A. Chupka, J. Chem. Phys. 30, 191 (1959).

49. M. L. Gross, Org. Mass Spectrom. 6, 827 (1972).

50. C. Lifshitz, A. M. Peers, M. Weiss and M. J. Weiss, Adv. Mass Spectrom. 6, 871 (1974).

51. S. M. Gordon and N. W. Reid, Int. J. Mass Spectrom. Ion Phys. 18, 379 (1975).

52. R. G. Cooks, K. C. Kim, T. Keough and J. H. Beynon, Int. J. Mass Spectrom. Ion Phys. 15, 271 (1974).

53. E. G. Jones, L. Bauman, J. H. Beynon and R. G. Cooks, Org. Mass Spectrom. 7, 185 (1973).

54. The relative intensities for $C_6H_5^+$, $C_6H_4^+$, $C_4H_4^+$ and $C_3H_3^+$ as shown by the breakdown diagrams in Refs. 3, 9, 13 and 14 only vary slightly in the total energy range 16.87-17.37 eV.

GENERAL CONCLUSION

The studies performed on nitric oxide, carbon disulfide, carbonyl sulfide, and acetylene demonstrate the capability of this apparatus to obtain high resolution data. Aided by the cooling of the rotational envelope from the supersonic beam source, IEs have been measured directly and accurately to within 3 meV. The optical resolution of 0.14 Å (FWHM) is the highest achieved to date using a supersonic molecular beam target of these gases and, if necessary, higher resolution can be obtained by using either narrower monochromator slits or a higher order dispersion from the grating. The accompanying loss in light intensity can be compensated for by using even longer discharge lamps than the one currently used. Satisfactory Rydberg series assignments were made for most of the autoionization structures with the aid of previously reported absorption studies. However, due to complicated interactions, many peaks remain unidentified in the CS_2^+ spectrum and multiple assignments were frequent in NO^+.

The study of the clusters $(CS_2)_{n=2-5}$, $(OCS)_{n=2,3}$, $(C_2H_2)_{n=2,3}$, $Ar \cdot CS_2$, and $OCS \cdot CS_2$ have provided thermodynamic data of the cluster ions, many of which were measured for the first time. The most interesting feature of cluster ionization, however, was the observation of red shifts for most dimer Rydberg peaks compared to those of the monomer with a few peaks exhibiting blue shifts. The actual quantity of the shifts have been tabulated and a model consistent with the observations has been proposed. To elucidate this explanation further, Fig. 6 illustrates the radial probability densities of two Rydberg orbitals

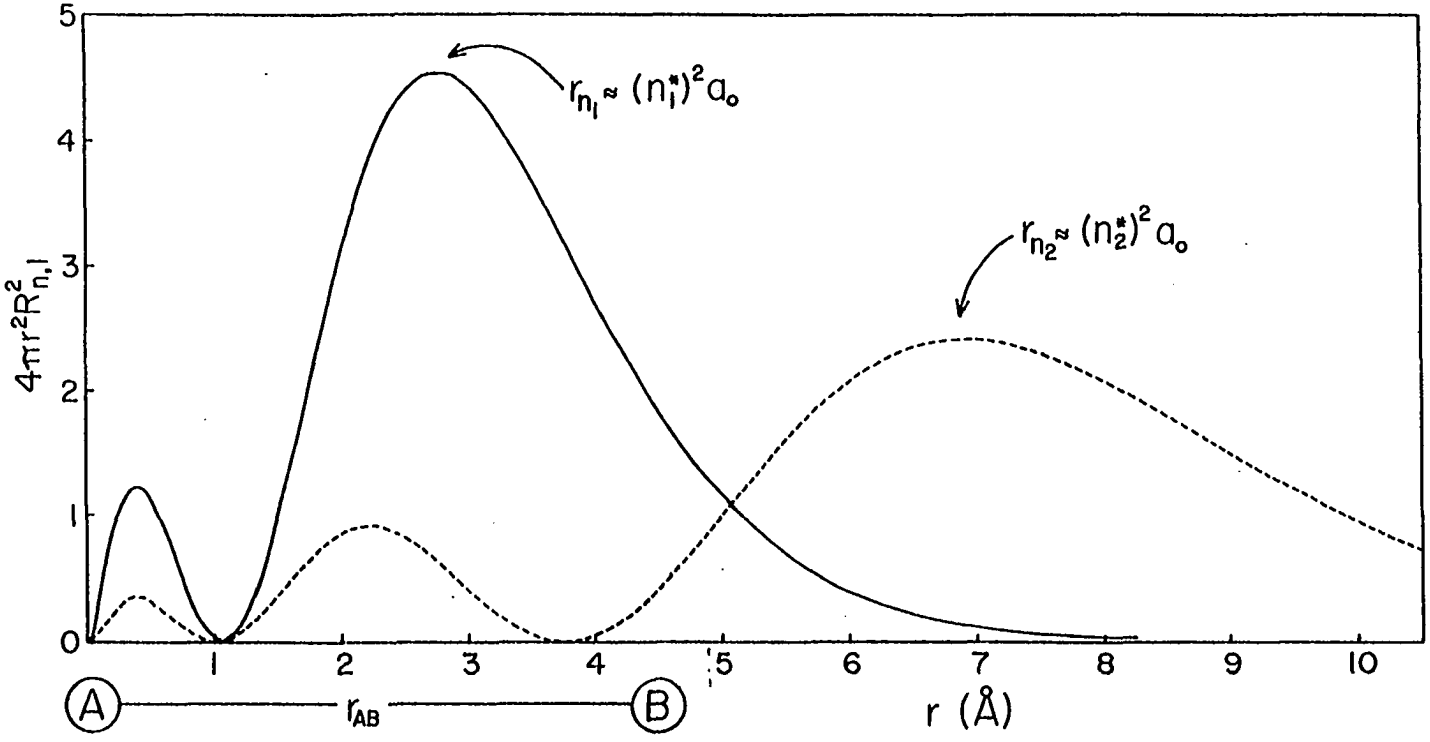

Figure 6. Schematic representation of the radial probability density, $4\pi r^2 R_{n\ell} R^*_{n\ell,*}$ for Rydberg orbitals characterized by the effective principal quantum numbers, n_1^* and n_2^*. Here r_{n1} and r_{n2} represent the radii of Rydberg orbitals characterized by n_1^* and n_2^*, respectively. r_{AB} is the intermolecular distance of a van der Waals molecule A • B

originating from molecule A of the AB van der Waals dimer. When an electron is excited to a Rydberg orbital with an average radius larger than the intermolecular distance r_{AB}, the shielding of the ion core A^+ by the Rydberg electron becomes less effective and charge multipole attractive interactions and chemical forces play a more important role in the bonding of the $A^*(n_2) \cdot B$ dimer. The potential energy of $A^*(n_2) \cdot B$ at the equilibrium configuration of AB is thus greater than the dissociation energy of AB and gives rise to a red shift in energy of the Rydberg transition in the AB dimer compared to that in A. If the electron, however, is excited to a level with r_A smaller than r_{AB}, the exchange repulsion will dominate and a blue shift will be observed in the dimer ion spectrum. Though other types of interactions may cause shifts in Rydberg transitions, this interpretation is consistent with the data and seems to be the most reasonable explanation.

The magnitudes of the shifts have also provided clues of the geometry of the CS_2 and OCS dimers. Comparing the magnitude of the shift of one series with that of another series, along with an assignment of a series to a particular type of orbital, possible geometries of the CS_2 and OCS dimers were discussed and further studies on $Ar \cdot CS_2$ and $OCS \cdot CS_2$ provided even greater insight to the nature of the cluster configuration.

Photoionization of the $(C_2H_2)_2$ and $(C_2H_2)_3$ clusters have provided insight into the energetics and internal energy effects of hydrocarbon clusters. The highest energy barriers to fragmentation along the reaction coordinate have been determined from the fragment AE

measurements and the observed fragmentation patterns have indicated that rearrangements to form more stable isomers occur prior to fragmentation. The specific evidence obtained here is that the $(C_2H_2)_3^+$ ion fragments have the same products as do the other isomers of $C_6H_6^+$, the AE of $C_4H_4^+$ from $(C_2H_2)_3$ was found to be lower in energy than the IE of $(C_2H_2)_2$, the AEs of $C_4H_3^+$ and $C_4H_2^+$ from $(C_2H_2)_3$ was in good agreement with the AEs of the two ions from 2,4-hexadiyne, 1,5-hexadiyne, and benzene on the total energy scale, and the relative intensities of the $C_6H_5^+$, $C_6H_4^+$ and $C_3H_3^+$ ions from $(C_2H_2)_3$ are in fair agreement with those from benzene, 2,4-hexadiyne, and 1,3-hexadiyne in the total energy range 16.87-17.17 eV. A review article of previous C_6H_6 fragmentation studies discusses the evidence obtained indicating that some other isomers of $C_6H_6^+$ rearrange prior to fragmentation (59).

The $(C_2H_2)_2$ studies provided insight into the possible mechanisms of $C_4H_4^+$ fragmentation and the competition between H atom elimination and H elimination as a function of the internal energy. Evidence was obtained indicating that elimination of 2H to form $C_4H_2^+$ occurred at the thermochemical threshold for the process and that this did not depend upon the formation of the electronically excited state of the dimer ion $C_2H_2^+(\tilde{A}^2\Sigma_g^+) \cdot C_2H_2$.

Additional photoionization studies on the ethylene, propylene, and cyclopropane clusters have been performed and are currently undergoing analysis. Preliminary results for ethylene indicate the $(C_2H_4)_2^+$ and $(C_2H_4)_3^+$ ions also undergo rearrangement with sufficient internal energy to more stable isomers. The fragment AE measurements were found to be

inconsistent with the findings of Ceyer et al. resulting in different interpretations of the intermediate complexes along the reaction coordinate. A comparison of the fragmentation patterns of $(C_2H_4)_3^+$ and $(C_3H_6)_2^+$ seem to indicate a common $C_6H_{12}^+$ intermediate, but closer examination is required prior to making any conclusions. So far, the evidence obtained from this laboratory is consistent with the assumption that energy randomization is rapid and isomerization rates are higher than the rates of decomposition at the energies used here.

REFERENCES

1. F. L. Mohler, Phys. Rev. 28, 46 (1926).

2. F. L. Mohler, P. D. Foote and R. L. Chenault, Phys. Rev. 27, 37 (1926).

3. K. Watanabe and E. C. Y. Inn, J. Opt. Soc. Am. 43, 32 (1953).

4. K. Watanabe, Phys. Rev. 91, 1155 (1953).

5. K. Watanabe, J. Chem. Phys. 22, 1564 (1954).

6. N. Wainfan, W. C. Walker and G. L. Weissler, J. Appl. Phys. 24, 1318 (1953).

7. N. Wainfan, W. C. Walker and G. L. Weissler, Phys. Rev. 99, 542 (1955).

8. H. Hurzeler, M. G. Inghram and J. D. Morrison, J. Chem. Phys. 27, 313 (1957).

9. H. Hurzeler, M. G. Inghram and J. D. Morrison, J. Chem, Phys. 28, 76 (1958).

10. G. L. Weissler, J. A. R. Samson, M. Ogawa and G. R. Cook, J. Opt. Soc. Am. 29, 339 (1959).

11. F. J. Comes and W. Lessmann, Z. Naturforsch 19a, 65 (1964).

12. V. H. Dibeler and R. M. Reese, J. Res. Natl. Bur. Std. 68A, 409 (1964).

13. P. M. Dehmer and W. A. Chupka, J. Chem. Phys. 65, 2243 (1976).

14. G. R. Parr and J. W. Taylor, Rev. Sci. Instrum. 44, 1578 (1973).

15. G. R. Parr and J. W. Taylor, Int. J. Mass Spectrom. Ion Phys. 14, 467 (1974).

16. M. G. Liverman, S. M. Beck and R. E. Smalley, J. Chem. Phys. 70, 192 (1979).

17. For a review of molecular beams, see J. B. Anderson, in Molecular Beams and Low Density Gas Dynamics, edited by P. P. Wegener, (Marcel Dekker, New York, 1974), Chapter 1.

18. C. Y. Ng, Ph.D. Thesis, the University of California, Berkeley, CA (1976).

19. C. Y. Ng, D. J. Trevor, B. H. Mahan and Y. T. Lee, J. Chem. Phys. 65, 4327 (1976).

20. C. Y. Ng, D. J. Trevor, B. H. Mahan and Y. T. Lee, J. Chem. Phys. 66, 3985 (1977).

21. C. Y. Ng, P. W. Tiedemann, B. H. Mahan, and Y. T. Lee, J. Chem. Phys. 66, 3985 (1977).

22. C. Y. Ng, P. W. Tiedemann, B. H. Mahan and Y. T. Lee, J. Chem. Phys. 66, 5737 (1977).

23 C. Y. Trevor, P. W. Tiedemann, S. T. Ceyer, P. L. Kronebush, B. H. Mahan, and Y. T. Lee, J. Chem. Phys. 67, 4235 (1977).

24. W. M. Trott, N. C. Blais and E. A. Walters, J. Chem. Phys. 69, 3150 (1978).

25. W. M. Trott, N. C. Blais and E. A. Walters, J. Chem. Phys. 71, 1692 (1979).

26. P. M. Dehmer and E. D. Poliakoff, Chem. Phys. Lett. 77, 326 (1981).

27. P. M. Dehmer and S. T. Pratt, J. Chem. Phys. 76, 843 (1982).

28. P. M. Dehmer, J. Chem. Phys. 76, 1263 (1982).

29. S. T. Pratt and P. M. Dehmer, J. Chem. Phys. 76, 3433 (1982).

30. O. F. Hagena, in Molecular Beams and Low Density Gas Dynamics, edited by P. P. Wegener, (Marcel Dekker, New York, 1974), Chapter 2.

31. J. O. Hirschfelder, C. F. Curtiss and R. B. Bird, Molecular Theory of Gases and Liquids, (Wiley, New York, 1964).

32. S. L. Anderson, T. Hirooka, P. W. Tiedemann, B. H. Mahan and Y. T. Lee, J. Chem. Phys. 73, 4779 (1980).

33. S. H. Linn, Y. Ono and C. Y Ng, J. Chem. Phys. 74, 3348 (1981).

34. S. H. Linn, Y. Ono and C. Y. Ng, J. Chem. Phys. 74, 3342 (1981).

35. G. G. Jones and J. W. Taylor, J. Chem. Phys. 68, 1768 (1978).

36. E. A. Walters and N. C. Blais, J. Chem. Phys. 75, 4208 (1981).

37. S. T. Ceyer, P. W. Tiedemann, C. Y. Ng, B. H. Mahan and Y. T. Lee, J. Chem. Phys. 70, 2138 (1979).

38. S. T. Ceyer, P. W. Tiedemann, B. H. Mahan and Y. T. Lee, J. Chem. Phys. 70, 14 (1979).

39. P. W. Tiedemann, S. L. Anderson, S. T. Ceyer, T. Hirooka, C. Y. Ng, B. H. Mahan and Y. T. Lee, J. Chem. Phys. 71, 605 (1979).

40. W. A. Chupka, P. W. Dehmer and W. J. Jivery, J. Chem. Phys. 63, 3929 (1975).

41. G. V. Marr, Photoionization Processes in Gases, (Academic Press, New York, 1967).

42. M. Seya and F. Masuda, Sci. Light 12 9 (1963).

43. N. R. Daly, Rev. Sci. Instrum. 31, 264 (1960).

44. R. W. Ditchburn, U. Opik, Atomic and Molecular Processes, edited by D. R. Bates, (Academic, London, 1962).

45. S. Geltman, Phys. Rev. 112, 176 (1958).

46. V. H. Dibeler and J. A. Walker, Int. J. Mass Spectrom. Ion Phys. 11, 49 (1973).

47. P. B. Killgoar, Jr., G. E. Leroi, J. Berkowitz and W. A. Chupka, J. Chem. Phys. 58, 803 (1973).

48. J. Berkowitz, Photoabsorption, Photoionization and Photoelectron Spectroscopy, (Academic, New York, 1979).

49. U. Fano, Phys. Rev. 124, 1866 (1961).

50. F. H. Mies, Phys. Rev. 175, 164 (1968).

51. J. W. Rabalais, Principles of Ultraviolet Photoelectron Spectroscopy, (Wiley-Interscience, New York, 1977).

52. W. A. Chupka, Ion-Molecule Reactions, Vol. 1, edited by J. L. Franklin (Plenum, New York, 1972), p. 33.

53. R. S. Mulliken, J Am. Chem. Soc. 86, 3183 (1964).

54. G. Herzberg, in Topics in Modern Physics - A Tribute to E. U. Condon, edited by W. E. Brittin and H. Odabasi, (Colorado Association University Press, Boulder, CO, 1971), p. 191.

55. For example, Y. Ono and C. Y. Ng, J. Chem. Phys. 74, 6985 (1981).

56. M. L. Vestal, in Fundamental Processes in Radiation Chemistry, edited by P. Ausloos, (Wiley-Interscience, New York, 1968).

57. P. J. Robinson and K. A. Holbrook, Unimolecular Reactions, (Wiley-Interscience, New York, 1972).

58. W. Forst, Theory of Unimolecular Reactions, (Academic, New York, 1973).

59. H. M. Rosenstock, J. Kannacher and J. F. Liebman, Radiat. Phys. Chem. (in press).

ACKNOWLEDGEMENTS

I would like to thank Dr. Cheuk-Yiu Ng for his guidance and support throughout my years as his graduate student. The intensity and drive with which he performs his work has truly been an amazement and an inspiration. I am indebted to my colleagues, Harry Prest and Steve Linn for their invaluable assistance and friendship. The many discussions and activities with them have been enlightening and unforgettable experiences. I would also like to express my appreciation to Dr. Mary Gress, John Erickson, Beth Osuch, and Wen Bih Tzeng for their assistance in acquiring some of the data.

Special appreciation go to my friends in Los Angeles, especially Daniel Alba, Junichi Shioda, John and Lynne Ozawa, and my sister Linda for their everlasting friendship, love and encouragement. Finally, I am eternally grateful to my parents for their support and understanding. Their dedication and faith in me is a prime source of motivation and has made all my achievements possible.